Technische Universität München

Lehrstuhl für Aerodynamik und Strömungsmechanik

Dynamic Stall on a Pitching Double-Swept Rotor Blade Tip

Benjamin Lütke

Vollständiger Abdruck der von der Fakultät für Maschinenwesen der Technischen Universität München zur Erlangung des akademischen Grades eines

Doktor-Ingenieurs

genehmigten Dissertation.

Vorsitzender: Prof. Dr.-Ing. Manfred Hajek

Prüfer der Dissertation: 1.   apl. Prof. Dr.-Ing. Christian Breitsamter

2.   Prof. Dr.-Ing. Lorenz Tichy

Danksagung

Abstract

Dynamic stall is experimentally and numerically investigated on a pitching double-swept helicopter rotor blade tip. The wind tunnel model with its advanced planform has a spanwidth of 750 mm and an aspect ratio of $AR = 4.5$. The aerodynamic and structural design of the instrumented wind tunnel model is presented in detail. The carbon composite reinforced plastic design leads to a high stiffness of the model. Thus, the aeroelastic influence is very limited and the first eigenfrequency is at $f = 67$ Hz. A negative elastic twist of $\alpha = -0.7°$ and a bending deformation of $D_z = 17$ mm at $r/R = 0.9$ occurs for the maximum load case at $Ma = 0.5$ and $Re = 1.2 \cdot 10^6$. The pitching motion for this load case has an amplitude of $\alpha = 8° \pm 5°$ and a reduced frequency of $k = 0.039$. The URANS computations with a rigid contour show a good agreement to the experimental results. Two areas of separated flow can be detected inboard and outboard of the forward-backward swept kink at high angles of attack. Strong crossflow velocities at the swept parts of the blade tip lead to delayed stall and decreased lift at the kink. Oscillations in the c_p-distribution are more evident than in the deep stall case. The laminar-turbulent transition is shifted downstream and stall sets in significantly earlier when the Reynolds number is reduced from $Re = 1.2 \cdot 10^6$ to $Re = 0.72 \cdot 10^6$. The unsteady pressure sensitive paint measurements show the same areas of separated flow. However, the increased surface roughness leads to an increased flow separation at the inboard section and delayed stall at the backward swept part. The variation of pitching frequency and Mach number show similar results as the experiments with two-dimensional pitching airfoils. One significant advantage of the forward-backward swept planform is that the sectional lift and moment do not collapse simultaneously over the span width. Thus, a sharp gradient in the global pitching moment is avoided.

Keywords

Dynamic stall, helicopter, double-swept blade tip, wind tunnel, carbon fiber reinforced plastic model, CFRP, structural design, separated flow

Kurzfassung

In dieser Doktorarbeit wird der dynamische Strömungsabriss an einer schwingenden, doppelt-gepfeilten Rotorblattspitze sowohl experimentell als auch numerisch untersucht. Das Windkanalmodell hat eine Spannweite von 750 mm und ein Seitenverhältnis von $AR = 4.5$. Die aerodynamische und strukturelle Auslegung des instrumentierten Windkanalmodells wird im Detail vorgestellt. Die Faserverbundbauweise führt zu einer hohen Steifigkeit des Modells, wodurch der aeroelastische Einfluss minimiert wird. Die erste Eigenfrequenz liegt bei $f = 67$ Hz. Für den maximalen Lastfall bei $Ma = 0.5$ and $Re = 1.2 \cdot 10^6$ ergibt sich eine negative Verwindung von $\alpha = -0.7°$ und eine Durchbiegung von $D_z = 17$ mm bei $r/R = 0.9$. Die Nickschwingung dieses Lastfalles ist bei einer Amplitude von $\alpha = 8° \pm 5°$ und erreicht eine reduzierte Frequenz von $k = 0.039$. Die URANS Simulationen zeigen eine gute Übereinstimmung mit den experimentellen Ergebnissen. Bei hohen Anstellwinkeln sind zwei Regionen abgelöster Strömung rechts- und linksseitig des vorwärts-/rückwärtsgepfeilten Knickes zu erkennen. Starke Querströmungen in den gepfeilten Bereichen der Blattspitze verzögern den dynamischen Strömungsabriss und verringern den Auftrieb bei diesem Knick. Für diesen Lastfall sind signifikantere Schwingungen in der c_p-Verteilung erkennbar als bei Lastfällen mit stärker abgelöster Strömung. Der laminar-turbulente Umschlagspunkt liegt weiter stromabwärts und der Strömungsabriss setzt deutlich früher ein, wenn die Reynoldszahl von $Re = 1.2 \cdot 10^6$ auf $Re = 0.72 \cdot 10^6$ abgesenkt wird. Bei den Messungen mit drucksensitiver Farbe tritt die Ablösung an den gleichen Stellen auf, jedoch führt die erhöhte Oberflächenrauhigkeit zu einer verstärkten Strömungsablösung im ungepfeilten und vorwärtsgepfeilten Bereich. Im rückwärtsgepfeilten Bereich wird der Strömungsabriss verzögert. Die Variationen der Nickfrequenz und der Machzahl zeigen ähnliche Ergebnisse wie von zweidimensional schwingenden Profilen. Ein wesentlicher Vorteil der vorwärts-rückwärts gepfeilten Kontur ist der zeitliche Versatz des Strömungsabrisses entlang der Spannweite. Dadurch wird ein starker Gradient im globalen Nickmoment vermieden.

Stichwörter

Dynamischer Strömungsabriss, Hubschrauber, doppelt-gepfeilte Rotorblattspitze, Windkanal, Faserverbundbauweise, strukturelle Auslegung, abgelöste Strömung

Contents

Nomenclature

b	m	Wind tunnel model breadth
$c_{(ref)}$	m	Airfoil (reference) chord
$c_p = \Delta p / \left(\frac{\rho_\infty}{2} u_\infty^2 \right)$	-	Pressure coefficient
u_∞	m/s	Free stream velocity
r	m	Radial position (from the root)
r_{inv}	m	Radial position (from the tip)
f	Hz	Frequency
k	-	Reduced frequency: $k = 2\pi f c_{ref} / u_\infty$
AR	-	Aspect Ratio
$C_{D/d}$	-	Global / local drag coefficient
$C_{L/l}$	-	Global / local lift coefficient
$C_{N/n}$	-	Global / local normal force coefficient
$C_{M/m}$	-	Global / local aerodynamic moment coefficient
D	N	Drag
L	N	Lift
M	Nm	Moment
Ma	-	Mach number
R	m	Total radius
Re	-	Reynolds number
T_0	K	Total temperature
p_0	Pa	Total pressure
$\mathbf{u}$	m	Deformation vector
$\mathbf{f}_a$	N	Aerodynamic force vector
$\mathbf{f}_I$	N	Inertial force vector
$\mathbf{f}_s$	N	Structural force vector
$\mathbf{M}$	kg	Mass matrix
$\mathbf{K}$	kg/s^2	Stiffness matrix
$\mathbf{D}$	kg/s	Damping matrix
$\mathbf{H}$	-	Interpolation matrix

Greek Symbols

$\alpha, \overline{\alpha}$	°	Angle of attack, mean angle of attack
$\alpha_{\pm}$	°	Sinusoidal motion amplitude
ρ	kg/m^3	Density
Λ	°	Sweep angle
ϕ_l	m	lth Mode shape
ψ	°	Azimuth position
θ_{coll}	°	Helicopter collective pitch angle
θ_{cyc}	°	Helicopter cyclic pitch angle
ω	2π/s	Natural frequency

1 Introduction

1.1 Motivation

The Blue Edge^{TM} helicopter rotor blade tip incorporated on the recently rolled out H160 (Fig. 1.1) is the first double-swept blade tip in operational flight since the BERP [1] blade tip. The latter was used on the G-Lynx helicopter which claimed the speed record of 249.1 mph (400.87 km/h) on August 11th 1986 [1]. Despite this promising result, it took another 30 years before the newly developed Blue Edge^{TM} blade came into use.

Figure 1.1: **AIRBUS-HELICOPTER-H160 with the Blue Edge^{TM} blade (© T.Rostang)**

The huge potential of the innovative planforms to reduce noise and vibrations, while enhancing the overall performance, and the progresses in composite manufacturing have led to the replacement of conventional blade tips. However, the aerodynamic and structural behaviors of a rotor blade are complex and their complexity increases with a more sophisticated planform. One can state that the aerodynamic phenomena are fully understood only for a few advanced rotor blade geometries if any. The high number of essential design parameters like rotor radius, twist, taper, chord and sweep already show the difficulty in designing 'the best rotor blade', not to mention the large number of possible flight states. Therefore, the optimized rotor blade tips cannot be investigated in every aerodynamic detail during the design phase. Unpredicted events might occur only later at the whirltower or at the flight test. Vortices that interact with the structure might only be resolved with high fidelity, expensive computational fluid dynamic (CFD) simulations

---
[1]British Experimental Rotor Programme

in advance. However, CFD is not yet capable of resolving all flow features within a reasonable amount of time. Even more striking is the uncertainty in the correct resolution of the flow. Especially, the lack of accuracy in regions of flow separation shows the need of experiments.
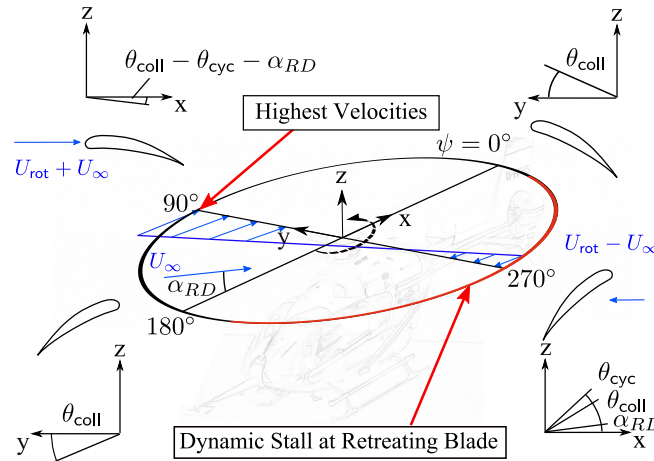
Figure 1.2: **Helicopter in fast forward flight**

In fast forward or maneuvering flight, the advancing blade experiences higher velocities than the retreating blade (Figure 1.2). The blade pitch angle is sinusoidally varied (θ_{cyc}) by means of a swashplate, so that the moment about the lateral axis is balanced [2]. The rotor disk plane angle of attack α_{RD} defines the angle between the velocity U_∞ and the rotor disk plane. The velocity U_∞ is the helicopter velocity with respect to the air [3]. Flow separation and dynamic stall occur at the retreating blade where the angle of attack is at its maximum. Since the separation behavior and flow phenomena are different for every planform and every airfoil, questions arise for every new rotor blade.

How does the dynamic stall behavior look like? Are there any significant local vortices that induce vibrations or high pitch link loads? How does the separation behavior change for different rotation frequencies, angles of attack and Reynolds numbers? Are there any unexpected flow phenomena due to the notch and the kink of the double swept planform? How well are the structural and aerodynamic behaviors captured by state-of-the-art numerical methods?

1.2 State of the Art

In the following, a short review of the experimental work done on dynamic stall is given. Some numerical studies are presented as well, in order to show the possibilities and drawbacks of the computational fluid dynamic simulations concerning dynamic stall.

1.2.1 Dynamic Stall at a Helicopter (Model) Rotor

One of the first fundamental investigations on dynamic stall in free flight was published in 1946 by Gustafson and Myers [4]. Tufts were attached to the rotor blades of a helicopter. A motion-picture camera mounted rigidly on the rotor hub recorded the motion of the tufts. It was observed that flow separation occurs at high advance ratios in the outer part of the retreating blade. A forward speed of 113 km/h at a rotor speed of 205 rpm is estimated to be close to the operational limit according to the pilot reaction. The static stalling angle of the airfoil is exceeded by 4° at the retreating blade tip. The authors propose, among others, the introduction of twist for a more homogeneous lift distribution on the blade.

In 1968 Harris and Pruyn published "Blade Stall - Half Fact, Half Fiction" [5] where they present results from rotor tests of different models and full-scale flight test data of the CH-47A aft rotor [6]. Besides the pure aerodynamics, the authors also focus on the blade elasticity and point out the differences between the more elastic full-scale rotor blades and the significantly stiffer model rotor blades. Drag, moment and lift stall are separated in the investigations. Drag stall is described as an inplane phenomena which usually only causes inplane bending and inplane vibrations. It is the less critical stall phenomena. Moment stall is more critical since it can produce fatigue limited control loads. Negative moment damping coupled with torsionally soft blades can lead to large amplitude torsional responses. Moment stall can also occur without lift stall for rather stiff blades. A strong lift stall is observed only for large and soft rotor blades with a strong blade elastic twisting response to moment stall. Therefore, one recommendation of the authors is the enhancement of the torsional stiffness of the rotor blades and the control system. Also, moment stall should be prevented or shifted from the blade torsion natural frequencies.
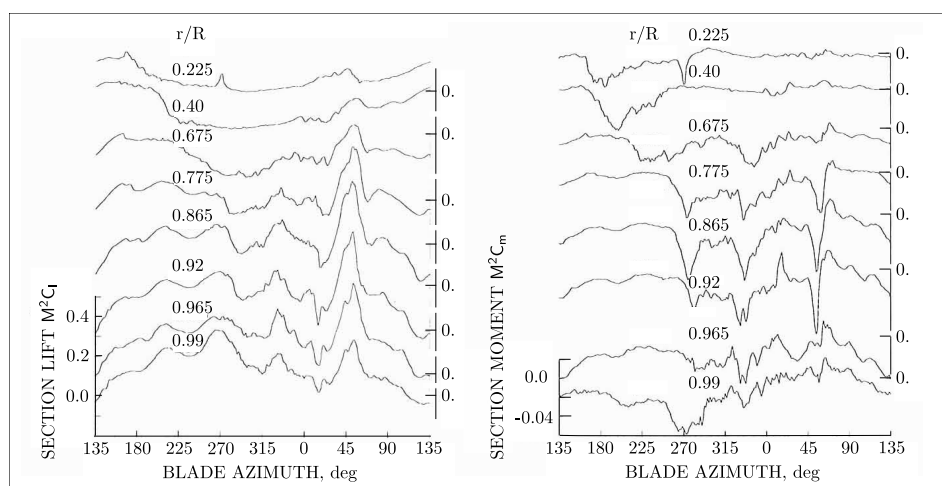
Figure 1.3: **Section stall and section moment for UTTAS pull-up at Rev14 [7]**

In the 1990's, UH-60A flight tests with highly instrumented rotor blades were performed [8]. Kufeld and Bousman [9] mention that due to dynamic stall [7] the pitch link loads are increased by a factor of 2.5 for severe maneuvers in comparison to maximum speed level flight. Three dynamic stall cases of the flight tests are presented in more detail in [7]: the 2.1 g UTTAS pull-up, a diving right turn at high speed and steady, level flight at high altitude or high loading. The author points out the general difficulty in measuring the accurate blade angle of attack in flight.

The induced flow angle is particularly difficult to determine. The development and occurrence of dynamic stall are described with regard to the azimuth and radial position. The 242 installed pressure transducers are used to integrate the section lift and section moment. The oscillatory pitch link loads during the UTTAS pull up are shown.

For a revolution, which shows a very high pitch link load, the section lift and the section moment of eight radial positions are plotted along the azimuth in Fig.1.3. Lift stall is clearly seen at the outboard section of the blade from 0.775R to 0.92R. It is observed at $\psi=273°$-$278°$ at the retreating blade. Lighter lift stall is found at about $\psi=330°$ and at the beginning of the first quadrant. At these positions, the lift stall is located closer to the blade tip. Strong lift stall is seen at $\psi=51°$-$54°$ for the advancing blade where higher onset Mach numbers occur. Moment stall is detected inboard of the blade at about $\psi=164°$-$166°$. This might be due to the flow over the nose of the aircraft which increases the local angle of attack at the inboard section of the blade. Three other moment stall cycles are detected at $\psi=252°$-$263°$, at $\psi=320°$-$330°$ and at $\psi=45°$. These stall events are located outboard of the blade and occur a few degrees before the corresponding lift stall events. The two other flight cases, which are not reproduced here, show similar stall cycles. However, for steady level flight the stall cycle in the first quadrant vanishes due to the lower inflow velocities at the advancing blade. The stall cycles at the retreating blade appear similar to the data obtained in wind tunnel tests with 2D pitching airfoils.

1.2.2 Dynamic Stall at 2D Pitching Airfoils

The fundamental experiments of Ham ([10], [11]) and McCroskey [12] showed that two-dimensional pitching airfoils show nearly the same stall characteristics as the retreating blade of a rotor at high advance ratios, see Fig.1.4. The forced pitching motion simulates the cyclic variation of the angle of attack (θ_{cyc}) which is necessary to balance the lift about the lateral axis.
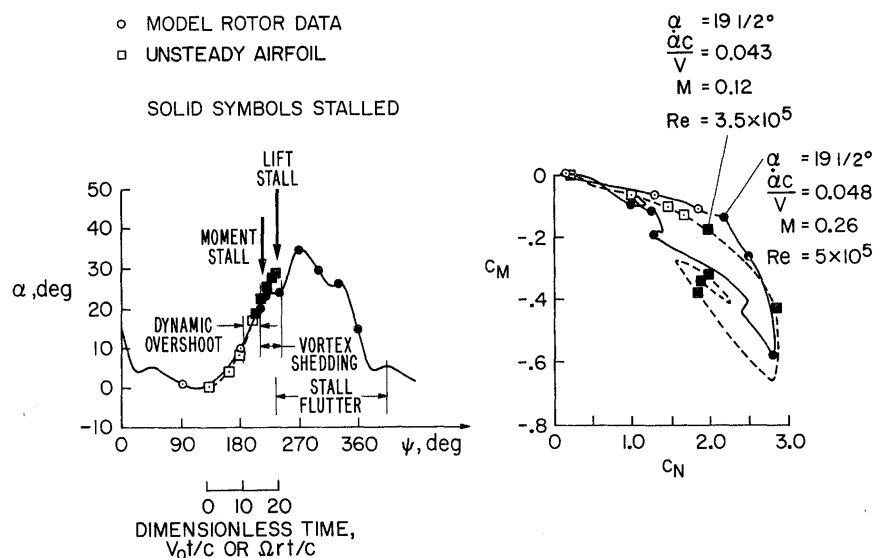
Figure 1.4: **Classical dynamic stall behavior for rotating and pitching blade [12]**

According to McCroskey [12], the essential flow features for $\psi=200°$-$360°$ are successively:

⌐ a dynamic overshoot and the beginning of the boundary layer separation with increasing angle of attack

⌐ a collapse of the suction peak

⌐ the formation of a leading edge vortex which is swept rearward and causes a negative pitching moment, e.g. moment stall

⌐ the dynamic lift stall at decreasing $\dot{\alpha}$
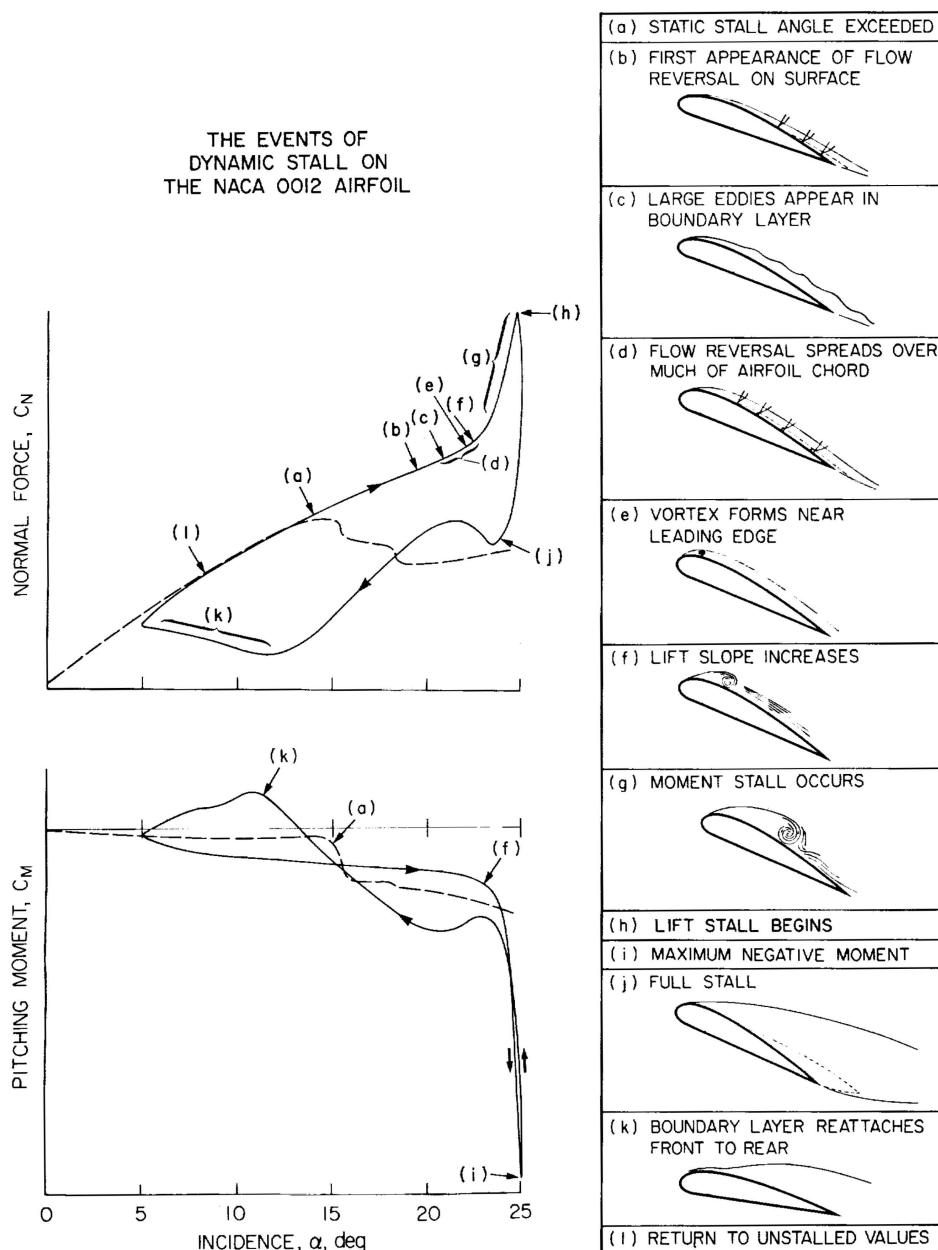
Figure 1.5: **Dynamic stall scheme [13]**

A detailed description of the flow phenomena, dynamic stall, is given in Carr et al. ([13],[14]). The scheme from [13] is depicted in Fig. 1.5. The pitching airfoil passes the static-stall angle at point (a) without any evident change in the flow around the airfoil. First flow reversal occurs at point (b) at the trailing edge (TE). The reversed flow spreads forward to the leading edge (LE) with increasing angle of attack (c)+(d). A vortex forms near the leading edge at point (e). The vortex grows and travels across the airfoil till point (h). It increases the lift significantly and leads to a strong negative pitching moment (i). As the vortex passes the trailing edge the lift peak suddenly drops, the flow is fully stalled (j). As the angle of attack decreases the flow gradually reattaches again (k)-(l).

In 1969, Liiva [15] already did one of the first pitching airfoil experiments. The influence of mean angle, pitching frequency and different Mach numbers are investigated in this work. Liiva defines a negative cycle damping D

$$D = [-\oint C_{My} d\alpha (\alpha_{\pm}^2 \pi^3 cf)]/[2v_{\infty}] \tag{1.1}$$

by the areas enclosed by clockwise circuits of C_{My} over α see Fig.1.6. The measurement points
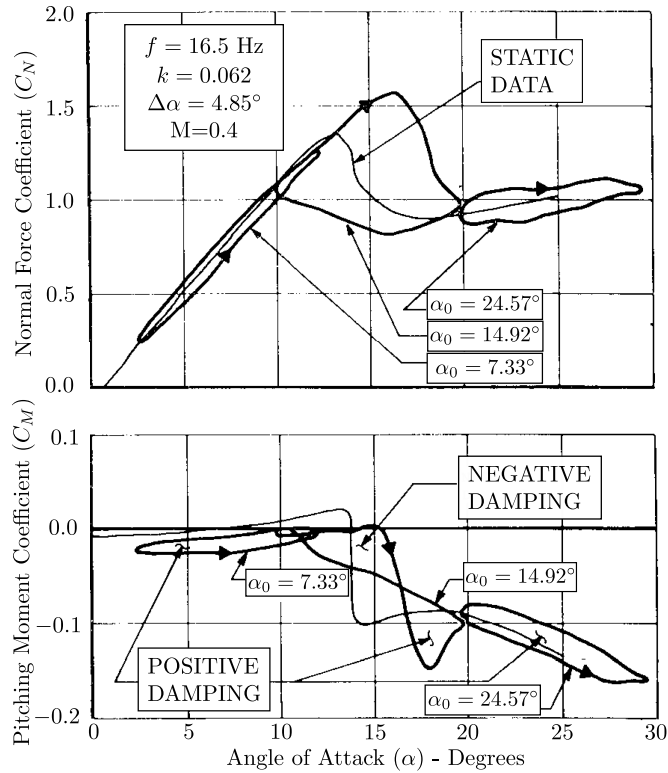
Figure 1.6: **Typical pitch oscillation data - Vertol 23010-1.58 airfoil [15]**

with the mean angles α_{mean}=7.33° and α_{mean}=14.92° are positively damped, whereas the measurement point at α_{mean}=14.92° has C_m-α circuits of both directions and is neutrally damped. If negative damping dominates, energy is extracted from the flow and stall flutter begins. For α_{mean}=14.92° a prominent dynamic overshoot in the lift and a large hysteresis in lift and moment are found. The strong and sudden negative pitching moment is remarkable. Similar to

the results, shown above, the moment decreases before the lift peak is reached. This can be explained by a leading edge vortex shifting the resulting lift to the trailing edge as it is swept rearward. Comparing the two pitching frequencies f_1=16.38 Hz and f_2=94.34 Hz Liiva shows that the onset of stall is postponed for the higher frequency. Comparing the oscillation amplitude $\alpha_{osc,1}$=2.5° and $\alpha_{osc,2}$=5°, Liiva [15] states that the negative damping is significantly larger at the low amplitude. The stall behavior at low Mach numbers Ma=0.2 and Ma=0.4 is described to be 'similar', whereas at Ma=0.6, no significant lift or moment break downs can be seen. This might be either due to the lower mean angle of attack, the low reduced frequency and the positive damping, but also due to a shock induced separation. As in the steady case, the stall peaks are shifted to higher angles of attack at higher Mach numbers. The C_L peak is higher for lower Mach numbers.

A symmetric and a cambered airfoil were compared by Liiva [15]. A more detailed investigation considering the influence of airfoil geometry can be found in [16] and [17]. In [16], dynamic stall is split into light and deep stall regimes in these investigations, shown in Figure (1.7). The
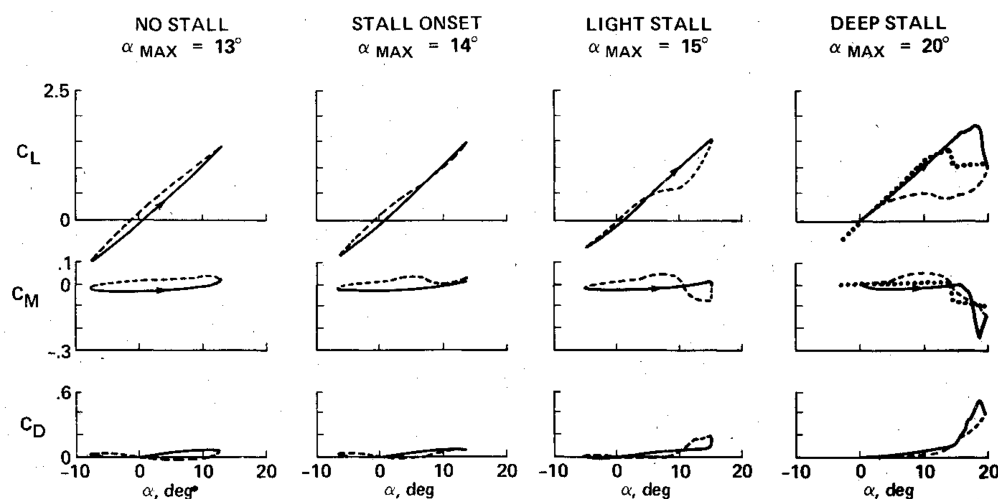
Figure 1.7: **Different dynamic stall regimes [17]**

peak negative moment, the lift and the drag become highest in the region of deep stall where the flow is separated for a large part of the cycle. The maximum incidence is higher than in the light dynamic stall regime. In the light stall regime, there is a stronger tendency toward negative aerodynamic damping. The maximum angle of attack is only slightly higher than the dynamic stall angle and the first large flow separation accompanied by large hystereses in the airloads can be observed. Light stall is more sensitive to all aerodynamic parameters and to the geometry of the airfoil. Thin airfoils with strong adverse pressure gradients at the beginning of the chord tend to exhibit 'leading-edge stall' with a concentrated vortex traveling from the leading to the trailing edge. The changes in C_L, C_M and C_D are more abrupt than for airfoils with a high leading edge camber. Profiles with a large leading edge chamber or rather huge profile thickness tend to stall at the trailing-edge first. In this case, the boundary-layer separation starts from the trailing edge and progresses forward to the leading edge with increasing incidence.

After 1980 experimental research focused on pitching swept wings, pitching blade tips and rotating experiments. Intensive experimental studies on sophisticated 2D pitching airfoils started at

the DLR Göttingen in the 1990s ([18],[19], [20],[21], [22]). The cited experiments took place in the Transonic Wind Tunnel Göttingen (DNW-TWG) at realistic Mach and Reynolds numbers.

In [18], results of an airfoil with a nose-drooping device at dynamic stall conditions are described. The successful reduction of moment and drag peaks is shown. However, the integration of the piezoelectric actuators is challenging and expensive. Their forces and the droop amplitudes are limited.

In [19], the authors show the potential of air jets positioned at 10% chord on the upper side of an OA209 airfoil. The pitching moment peaks are reduced up to 84% while increasing the lift by 37% at Ma=0.3. The investigations at Ma=0.4-0.5 are also promising. Again, the complicated integration in an operating rotor blade and the additional weight are strong drawbacks of the active dynamic stall control techniques.

Leading vortex generators (LEVoGs) [20] seem more promising from an operational point of view. Shaped as flat cylinders with a diameter of 6 mm and a height up to 1 mm they are simply glued on the model surface. They are positioned at the stagnation point and different spacings were investigated. The pitching moment peaks and drag peaks at dynamic stall conditions are decreased while the lift performance is kept. Furthermore, the flow is not significantly influenced by the LEVoGs at high Mach numbers and low angles of attack. Thus, the performance on the advancing blade is not decreased.

Unsteady design criteria [23] were used in the numerical design process for the airfoils EDI-M112 with 12%-thickness and the EDI-M109 with 9%-thickness. Wind tunnel tests have been carried out in the DNW-TWG, the experimental results have been presented in Gardner et al. [24]. The airfoils EDI-M112 with 12%-thickness and the EDI-M109 with 9%-thickness show excellent dynamic characteristics at dynamic stall. For Ma=0.3 both airfoils, the EDI-M112 and the EDI-M109, show a turbulent boundary layer separation at the trailing edge moving forward to the leading edge with increasing angle of attack. With increasing angle of attack the trailing edge separation changes into a leading edge separation at the EDI-M109, since a strong leading edge-vortex starts traveling backward and pushing the trailing edge separation off the end of the airfoil. Only at low pitching frequencies there is enough time for the trailing edge separation to reach the leading edge and cause full separation of the airfoil. In case of the EDI-M112 there is always a trailing edge separation. For Ma=0.4 there are no significant changes for the EDI-M109. A shock induced trailing edge separation can be seen for the EDI-M112. For Ma=0.5 both airfoils show a shock induced trailing edge separation, but with a stronger shock at the EDI-M112. The higher cycle-to-cycle variations and higher peak moments of the EDI-M109 for Ma=0.3-0.4 lead to the conclusion that the EDI-M112 is better suited for this Mach number regime. On the other hand the EDI-M109 shows less strong shocks and therefore smaller dynamic stall peaks for Ma=0.5 which states its relevance at higher Mach number regimes.

1.2.3 Dynamic Stall at 2.5D - 3D Pitching Configurations

An intermediate step from the 2D pitching configuration to the rotating system are pitching swept wings and pitching blade tips. In 1979 Hilaire [25] published the experimental results of an 30° backward swept and unswept oscillating NACA 0012 airfoil. The experiments were carried out in the 2.44 m octagonal test section of the UTRC Main Wind Tunnel (MTW). The tests focused on the lower Mach number regime Ma=0.3-0.4, at Reynolds numbers up to Re=6.82·10^6 for Ma=0.3. For both configurations (swept and unswept), the peak responses in lift, pressure

drag and moment are shifted to higher incidence as the frequency is increased. The peak amplitudes are increased as well. Although the pitching moment peaks are lower for the swept configuration, the stability margin of the airfoil is reduced, especially at low frequencies.

One of the first experiments with a hydraulic oscillation rig and pitching blade tips was done by H. Triebstein [26] in the 3 x 3 m wind tunnel of the DFVLR-AVA in Göttingen. He investigated rectangular tips with a NACA 0012 airfoil and different tip caps. However, the publication focuses on the complex calibration procedure of the pressure measurements. All pressure taps are connected to a single central pressure transducer using an electromechanical pressure switch. Transfer functions have to be built in the calibration procedure. Triebstein shows that the lift area of the oscillating tip is reduced towards the tip in the same way as it is known from the fixed wing. The tip vortex itself is described as strongly dependent on angle of attack, on oscillation frequency and on the geometry of the tip. Triebstein shows that the phase angle between motion and pressure increases for higher frequencies. The differences between the two end edges on the aerodynamic behavior do not become clear. Although the mean flow velocity and the oscillation amplitudes are lower than in reality, this publication is useful for validating vortex theories.
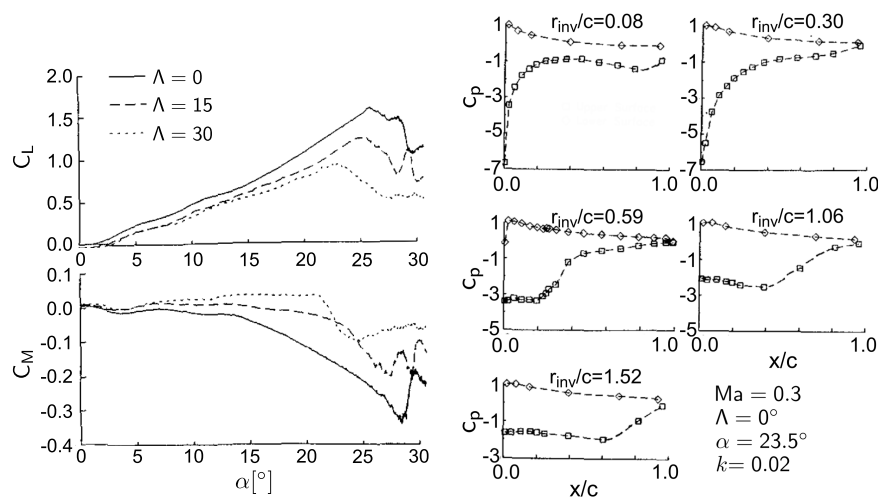
Figure 1.8: **Ramp** $0° - 30°$ at Ma**=0.3 and** k**=0.02; instantaneous** c_p **at** α**=23°** **[27]**

From 1988-1993, Lorber et al. ([28], [27], [29], [30], [31]) presented experimental data of a pitching unswept and backward swept three-dimensional wing in the UTRC Main Wind Tunnel, mentioned above. A straight, rectangular, untwisted blade tip of 1220 mm span and 440 mm chord was used. The model had a Sikorsky SSC-A09 9% thickness cambered airfoil section. A rounded tip cap was used for most of the measurement points which include Mach number from Ma=0.2 till Ma=0.6. The stall angle and the maximum lift coefficient decrease from lower to higher Mach numbers for steady and unsteady results. At all Mach numbers the unsteady lift, drag and moment peaks are higher than the corresponding steady peaks. Stall is delayed by the unsteady motion. The unsteady increments to the loads are increased with increasing pitch rate. These results are in good agreement with the two-dimensional pitching airfoil. Lorber states that the influence of the tip vortex is stronger for the unswept wing since the vortex rolls up over the upper tip surface and induces high suction loads near the trailing edge. Thus, the pitching moment is more negative for the unswept wing (Λ=0) than for the backward swept wing, as can be seen in Fig. 1.8. The instantaneous c_p distributions at Ma=0.3, α=23.5° of an 0-30° unswept

ramp case are shown in the right diagram of Fig 1.8. The flow is separated over large parts of the inboard sections $0.59 \leq r_{inv}/c \leq 1.52$ whereas strong suction peaks can be seen at the two outboard sections. The induced velocities resulting from the tip vortex reduce the effective angle of attack at the outboard sections. Thus, stall is delayed. Furthermore, the roll-up of the tip vortex increases the suction pressure at the most outboard section r_{inv}/c=0.08. The vortex propagation speed on the inboard is similar to two-dimensional results, whereas it is significantly lower at the tip. This might be due to the interaction between stall and tip vortices which also enhance the tip lift, as mentioned above. These effects are reduced at higher Mach numbers. The square tip shows a stronger tip vortex and therefore a higher lift near the tip than the round tip cap. However, this effect is significant only for the unswept wing.

Tang and Dowells' attempt [32] was to improve the semi-empirical, unsteady aerodynamic models used in comprehensive rotor codes like CAMRAD [33]. The aerodynamic models are often based on experimental two-dimensional airfoil data, as presented in Section 1.2.2. An aerodynamic transfer function is determined from the ratio of the output C_l to the input α_{osc} and the phase shift between output and input signals. The transfer function is fitted through the measured frequencies by means of several coefficients. Tang and Dowell showed the coefficients' dependency on the spanwise position at a pitching low aspect wing. They propose to investigate more complex planforms than the rectangular wing which was used by them. The maximum airstream velocity they achieved was 28.5 m/s for the unsteady measurement points.
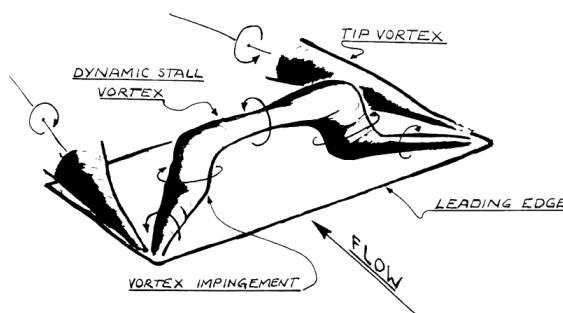
Figure 1.9: **Omega vortex at pitching 3D-configuration [34]**

Coton and Galbraith conducted wind tunnel tests with a straight wing of span b=1260 mm and chord c=420 mm ([35],[34]). The model was mounted and excited on its lower surface. It was located in the middle of the 2.13 x 1.161 meter octagonal cross section of Glasgow's Handley Page wind tunnel. Ramp-up pitch cases from -5° to 40° were carried out at different reduced frequencies. The authors confirm the previous mentioned works, where the peak C_n is increased and stall is delayed to higher incidence for increased pitching frequencies. Coton and Galbraith show that the peaks of C_n are significantly higher for the 68% of span location than at 57% span (50% = center of the wing). The peak values at 80% span are in between the peaks of the 57% and 68% of span location. Below α=20°, the gradient of C_n is non-linear at 95% and lower than the gradients of the other sections. Above 20°, the gradient of C_n increases as it does for the 68% and 80% spanwise sections. The effective reduced pitch rate k and the effective incidence are decreased at the wing tip by the tip vortex. The two effects counteract each other. Even if this leads to a simultaneous development of the dynamic stall vortex along the span, the outer

parts of the vortex are forced to the surface by the downwash of the tip vortices. The lower lift peaks at the mid-span are explained by the rise-up of the dynamic stall vortex from the wing. A sketch of the so-called omega vortex is shown in Fig 1.9.

Le Pape et al. [36] did extensive wind tunnel measurements in the ONERA F2 wind tunnel in order to enlighten the dynamic stall phenomenon. Two 2D models with different chord length and one 3D-model were investigated. The OA209 airfoil was used for all models. Le Pape confirms what McCroskey already suspected in 1969 and Chandrasekhara et al. presented in 1998: the strong adverse pressure gradient at the leading edge leads to a laminar separation bubble. This holds for low Mach and Reynolds numbers and for most airfoils with a strong leading edge curvature. A characteristic pressure plateau develops at the location of the bubble. At high angles of attack the bubble bursts and generates a dynamic stall vortex. The bubble gets smaller for increasing Reynolds numbers and the bursting of the bubble seems to appear later. Thus, the static stall angle of the OA209 airfoil is significantly increased for higher Reynolds numbers. However, the lift and moment stall are stronger for the lower Reynolds number for the dynamic test cases. Even for the 2D-configuration the flow is highly three-dimensional as soon as the flow separates. The transverse velocity component reaches up to 20% of the incoming freestream velocity. The $C_l(\alpha)$ slope is decreased for the 3D-configuration. The inboard section r/R=0.5 shows the same sharp stall as the 2D-configuration at higher angles of attack. For a deep stall case the moment hysteresis and the pitching moment is decreased towards the blade tip. Only at the very outer section (r/R=0.99) the moment hysteresis is strongly decreased and the pitching moment drops significantly.

Merz et al. ([37],[38]) did intensive wind tunnel measurements on a pitching blade tip in the Side Wind Test Facility Göttingen from 2014-2015. Results at Ma=0.16 and Re=0.9·10^6 are presented. The DSA-9A airfoil and a parabolic blade tip is used for the wind tunnel model with an aspect ratio of AR=6.2. The model is negatively twisted by $5.5°$ towards the blade tip. Merz shows the onset of dynamic stall and the development of a leading edge vortex at a radial position of r/c=4 by means of pressure transducers and PIV. At this position the influence of the reduced frequency on the lift coefficient is also strongest. From k=0.025 to k=0.075 the lift peak is increased by $\Delta C_L \approx$0.3 for a deep dynamic stall case. The minimum pitching moment is found at the same spanwise position, but it is nearly not affected by the reduced frequency. Further outboard, at r/c=5.19, the maximum lift does not change significantly for different pitching frequencies. However, the pitching moment coefficient decreases when decreasing the frequency.

1.2.4 Investigations on Double-Swept Blade Tips

The experimental investigations on double-swept blade tips are very limited to this day. In 1990 A. Brocklehurst published experimental and numerical results of the British Experimental Rotor Programme (BERP) blade [39]. This double-swept blade was flewn on a Westland Lynx helicopter and held the world speed record of 249.1 mph (400.87 km/h) until 2014. Brocklehurst used the outer 30% of the full-scale blade for the wind tunnel test. A total of 915 pressure taps are integrated in the model. Static measurements at $Re \approx 1 \cdot 10^6$ and Ma=0.16 are carried out at different angles of attack. Fig. 1.10 shows the pressure distributions at three different
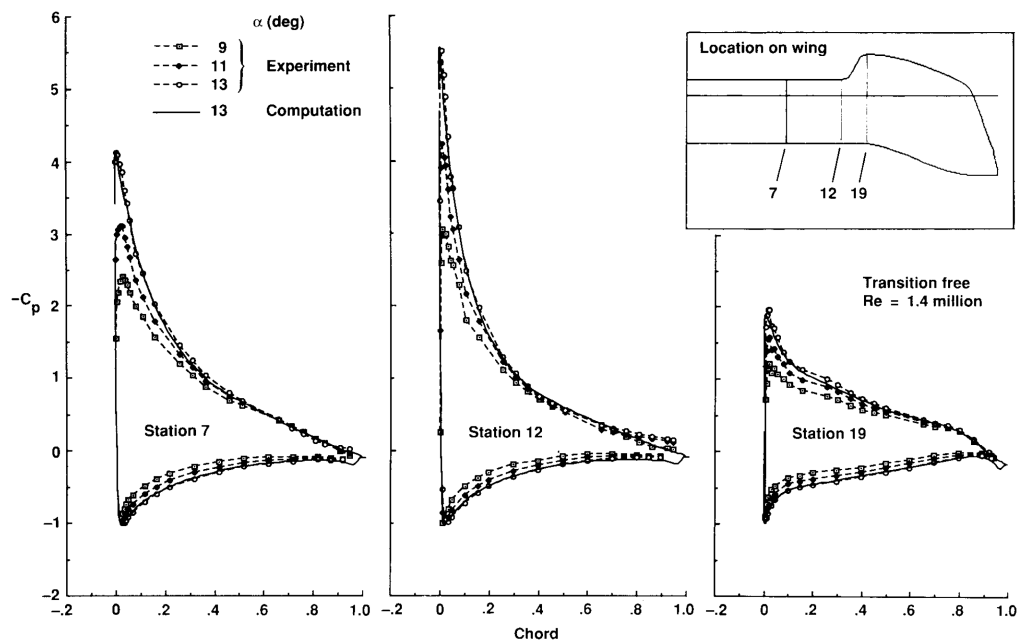
Figure 1.10: **Static pressure distribution on three spanwise sections [39]**

stations for three different angles of attack. The leading-edge suction is remarkably increased at the beginning of the forward sweep. At station 19 it is significantly reduced, further inboard at station 7 it shows nearly two-dimensional behavior. Flow visualizations confirm a stable circulation at the notch.
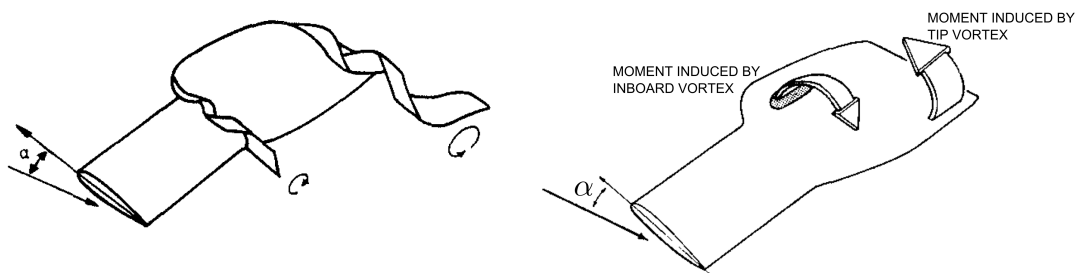
Figure 1.11: **Moment and vortices on BERP [40]**

In [40], Scott et al. did similar experiments as Brocklehurst and compared the BERP blade to other helicopter rotor blade tips numerically and experimentally. Besides the tip vortex, Scott approves the strong influence of the inboard vortex which occurs at the forward sweep for higher angles of attack (Fig.1.11). Both vortices lead to a downwash which energizes the boundary layer along the "paddle" part of the planform. The local angle of attack is reduced and the flows stays attached at higher angles of attack. The suction applied ahead of the pitch axis balances the

nose-down moment at the tip (Fig. 1.11) only till the flow separates. Since the inboard vortex detaches at relatively low angles of attack from the surface a strong gradient in the pitching moment was observed. The authors propose different airfoils to solve this problem. At high Mach numbers the planform of the BERP reduces the maximum Mach number and shocks are diffused significantly.

In 1997, Yeager et al. [41] published experimental results of a model helicopter equipped with BERP-type blades tested in the Langley Transonic Dynamics Tunnel. Compared to a set of rectangular baseline blades, the BERP-type rotor showed no performance improvements in either forward flight or hover. Pitch-link oscillatory loads are increased for the advanced configuration and only the 4-per-rev vertical fixed-system loads are lower for the BERP-type rotor. However, neither the same airfoils as on the Lynx helicopter have been used, nor is the structural dynamics of the blade and the rotor the same as on the original.

In [42] P. Rauch et al. present flight test data of the double-swept rotor blade Blue Edge^{TM}, developed for the reduction of blade-vortex interaction (BVI). Within the preceding French-German ERATO program, the double-swept ERATO blade was tested in the DNW-LLF wind tunnel and in the Modane S1MA wind tunnel [43]. In these tests a significant noise reduction due to the double-swept planform could be shown. Based on the ERATO program [44], Airbus Helicopters launched the Blue Edge^{TM} program where the further optimized Blue Edge^{TM} blades are operated in flight. Besides final flight test data, the development from the ERATO blade to the Blue Edge^{TM} blade is shown in [42] and [45]. One main issue is the high bending-torsion coupling which leads to high torsion deformations and high control loads. Therefore, the sweep angles and the structure of the initial blade were modified, so that the center of gravity is moved in front of the aerodynamic center. The final flight tests are done on a five blade rotor on a EC155, the data compared to the 7AD baseline configuration. The noise is significantly reduced, BVI mostly eliminated. Static and dynamic control loads are reduced for many flight conditions. Only at low rotor loadings the dynamic control loads are increased. Hover performance shows significant benefits. In forward flight, the performance is similar to the reference.

1.3 Objective

The literature review has shown that a lot of research has been done on the topic dynamic stall for more than 70 years. Pitching airfoils and blade tips have proven to show many of the most important aerodynamic phenomena which a helicopter rotor blade experiences. The unsteady aerodynamics get more complex on double-swept configurations like the BERP blade. The review of helicopter rotor blade tip shapes of Brocklehurst and Barakos [46] shows the research which has been done to find the best helicopter rotor blade tip. However, due to the large number of geometric, structural and aerodynamic parameters it is impossible to find the one and only blade tip. A new double-swept blade tip has been established on the H160 but detailed experimental aerodynamic investigations have not been published so far.

Therefore the overall objectives of this thesis are:

(1) the aerodynamic and structural design of an advanced, pitching double-swept helicopter blade tip for the investigation of dynamic stall in the Transonic Wind Tunnel Göttingen (DNW-TWG). The following additional conditions are stated:

- ↗ A high degree of instrumentation is required in order to detect local flow phenomena.

- ↗ A high stiffness of the model should reduce the aeroelastic influence of the model which would be totally different to a real helicopter rotor blade.

(2) the experimental investigation of dynamic stall by means a highly instrumented wind tunnel model. The specific objectives of this research are to:

- ↗ analyze the surface pressure distribution and the flow separation at different Mach and Reynolds numbers, pitching frequencies and angles of attack.

- ↗ evaluate the influence of the double-swept planform on the flow and a comparison to two-dimensional results.

- ↗ address the question how the pitching moment may be effected by the advanced planform.

- ↗ investigate if the use of unsteady pressure sensitive paint is appropriate for the investigations mentioned above.

(3) to establish a numerical setup which supports the flow analysis and could be used for rotational cases in the future. Thus, the influence of rotation could be determined numerically and compared to the non-rotational results.

1.4 Outline

The remaining of this thesis is organized as follows:

In chapter 2.1, the wind tunnel and the experimental setup are described. A short overview of the applied computational fluid dynamic (CFD) simulations is given. The background of the structural analysis (finite element method) is briefly described.
In chapter 3, the wind tunnel model is presented in detail. A high fidelity 3D finite element (FE) model of the carbon fiber reinforced plastic (CFRP) structure has been built. The experimental and numerical modal analyses are compared. Two different modal analyses have been carried out: one with the model on a solid steel block, the other with the final clamp condition in the wind tunnel. At the end of this chapter, the loads analysis is presented. The setup of the CFD-computations and the loads applied on the finite element are shown. Detailed insights in the strength analysis of the carbon fiber reinforced plastic model are given.
The global loads and local flow phenomena at static angles of attack are presented in chapter 4. The agreement between the experimental and the computational results is excellent. The focus is on high angles of attack where flow separations sets in.

In chapter 5, the phenomenon dynamic stall on the pitching double-swept rotor blade tip is investigated. The influence of the Reynolds number, the Mach number, the mean angle of attack, the pitching frequency and the oscillation amplitude are shown. The quality of the computational setup for the presented test cases is evaluated.

Finally, in chapter 6 the conclusions drawn from this work are summarized and suggestions for future work are laid out.

2 Experimental and Numerical Methods

2.1 Transonic Wind Tunnel and Hydraulic Test Oscillation Rig

The experiment has been designed for the Transonic Wind Tunnel Göttingen (DNW-TWG) with its 1 x 1 m cross section. The flexible top and bottom wall of the adaptive test section are adapted to minimize the interference velocities at the wall. The walls are adapted to the steady flow at the mean angle of attack. The wall adaptation method uses the static pressure measured at 32 positions in the midsection of the upper and lower wall. The one-step method of wall adaptation is based on the potential theory and uses a Cauchy-type integral [47]. The position data of the walls is recorded and can be also used for numerical simulations. The aerodynamic and thermodynamic data of the wind tunnel are listed in Table 2.1. The Mach number can be varied from $Ma = 0.3 - 0.9$. The wind tunnel can be pressurized in the range from $0.3 < p_0 < 1.5$ bar. The maximum Reynolds number capability is $Re = 1.2 \cdot 10^6$ for dynamic stall test cases based on the used model with a reference length of $c = 160$ mm. The support of the hydraulic test rig and the optical accesses of the adaptive measurement section are shown in [48] and in Fig. 2.1.
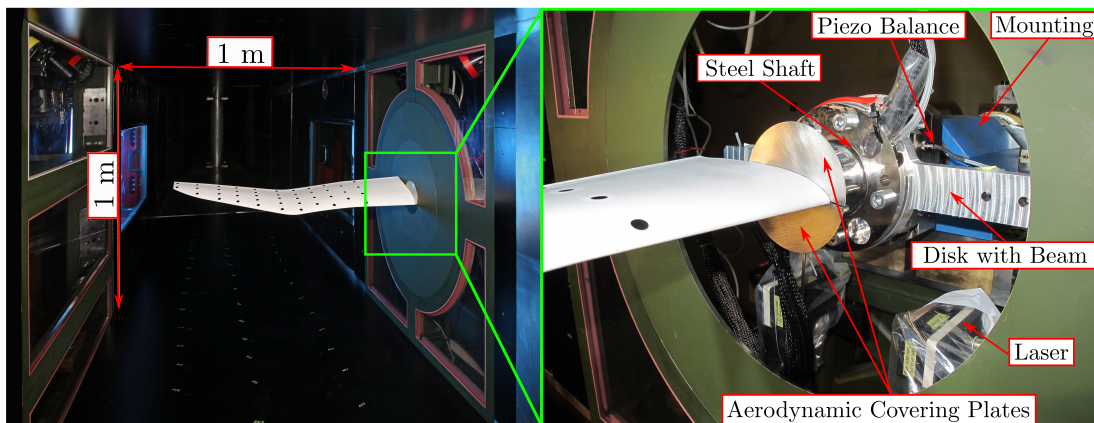

Figure 2.1: **Double-swept rotor blade tip in the DNW-TWG [49]**

As one can see in Fig. 2.1, the model or the piezoelectric balance, respectively, are mounted to the drive shaft which is supported by two double-row ball bearings in the mounting. The drive shaft is attached to a hydraulic rotational cylinder via a bellow. An electronically controlled

Table 2.1: **Transonic Wind Tunnel Göttingen - thermodynamic data with** $c_{ref} = 0.16$ **m**

p_0 in bar	T_0 in K	Ma	Re_{max}	$\alpha_{osc,max}$ ($f = 6.6$ Hz)	$\alpha_{osc,max}$ ($f = 13.2$ Hz)
0.3-1.5	293-315	0.3-0.9	$2 \cdot 10^6$	6°	4°

servo valve controls the fluid flow rate and flow direction into the hydraulic cylinder. A magnetic dependent resistor is positioned on the hydraulic cylinder and measures the angle of attack. The measured signal is used as input for the control circuit of the hydraulic control. The maximum possible frequencies and amplitudes for a sinusoidal harmonic motion of the test rig are given in Table 2.1. With increasing pitching frequency the maximum possible amplitude decreases. More information concerning the hydraulic test oscillation rig can be found in [50].

2.2 Applied Measurement Techniques

2.2.1 Angle of Attack, Motion and Deformation of the Model

The angle of attack is measured in two possible ways. As mentioned above, the angle of attack is measured with a magnetic dependent resistor (MDR) mounted on the hydraulic cylinder. The second angle of attack measurement is located close to the model root: two fixed triangulation-based laser range finders measure the distance to the beam, see Fig. 2.1. The distance $L1$ measured by the laser on the right side and the distance $L2$ measured by laser on the left side of the pitching axis are summarized and divided by the distance x between the lasers. Then, the angle of attack measured by the lasers is given by

$$\alpha_L = \arctan\left(\frac{L1 - L2}{x}\right) \tag{2.1}$$

The sensitivity of the laser is 2.5 mm/V and its resolution 20 μm. Further technical details of the MICRO-EPSILON range finders optoNCDT 1607-50 can be found in the technical data sheets and in [50]. The slope of the beam, the non-perfect surface of the beam and the resolution of the optics leads to a maximum error of measurement of $\alpha_{L,err} \approx 0.07°$. The same error is expected for the MDR. At the beginning of the experiment, both α-measurement techniques are adjusted and tested with a digital level which is put on a model template parallel to the chord. The digital level CLINOTRONIC of the Wyler AG is also used for the daily calibration of the MDR. It is accurate up to 0.02°, so that the absolute error of measurement is still less than $\alpha_{L,err} < 0.1°$. However, this error is neglected and not indicated in the results.

The model deformation is recorded with optical real-time measurements using the stereo pattern recognition (SPR) method [51]. Two cameras observe discrete, adhesive markers of 0.03 mm thickness on the model surface. The Mikrotron 1310 CMOS cameras with a reduced chip size of 1024 x 660 px take pictures with a maximum frequency of 800 Hz. Objectives with a focal length of 16 mm were used. Four Rapp OptoElectronic high power LED arrays WLD121 provide about 4000 Lux at the model surface. The detailed calibration procedure of the SPR-system
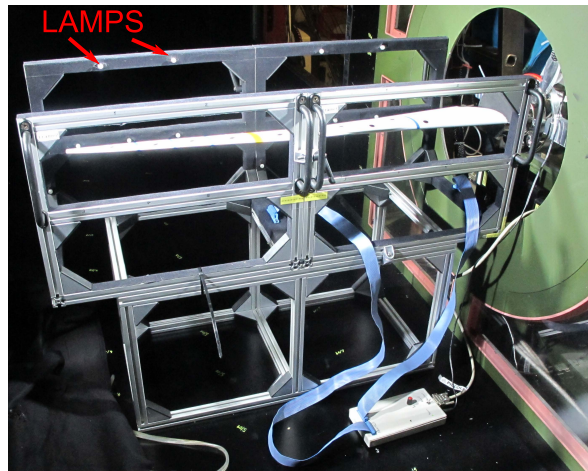
Figure 2.2: **Calibration of the 3D optical deformation measurement system**

is described in [52]. A frame with previously determined marker positions, which cover the measurement volume, is required. The applied frame, shown in Fig. 2.2, has 32 lamps serving as markers: 16 lamps on three different z-levels on the back side and 16 lamps on the front side. Each lamp is recorded separately and the 2D-chip position of the centroid is calculated. Recording at least 7 same markers with the cameras a matrix is generated which multiplied by the 2D-chip positions of unknown recorded points yield the 3D-coordinates physical coordinates. The measurement accuracy depends on many parameters: position and angle of the cameras, lens distortion, quality of the calibration procedure, illumination, depth of field, exposure time, vibration level and marker diameter. In [53] the measurement accuracy is determined for laboratory conditions. In the experiment, the model was recorded at two defined angles without wind. Then, the difference angle was calculated by the sectional markers and compared to the measurements of the CLINOTRONIC. The maximum error of measurement is $\alpha_{Pic,err} \approx 0.1°$ for an oscillation amplitude of $\alpha = \pm 5°$.

Accelerometers are used to record the acceleration and the vibration of the model during the experimental modal analysis and the wind tunnel test. The specifications of the used sensors PCB 352C22 are given in Tab. 2.2.

Table 2.2: **Technical data of the accelerometer PCB 352C22**

Sensitivity ($\pm 15\%$)	mV/g	10
Measurement Range	g/pk	$\pm$ 500
Frequency Range ($\pm 5\%$)	Hz	1.0 to 10000
Broadband Resolution (1 to 10000 Hz)	m/s^2 rms	0.02
Non-Linearity		$\leq 1\,\%$
Transverse Sensitivity		$\leq 5\,\%$

Their sensitivity is about 10 mV/g, the exact values of each transducer are defined in the according data sheets and used in the setup of the measurement software.

2.2.2 Global Forces - Piezoelectric Balance

The global forces and moments are measured by a piezo-multicomponent balance. The principle of the balance which consists of four three-component piezoelectric transducers was developed by Schewe [54]. Several aerodynamic applications are described in [55], [56] and [57]. A 3D-sectional view of the balance is shown in Fig. 2.3 on the right. On the left, the balance is shown from the back in mounted position. The four piezoelectric elements are arranged between the top plate and the bottom plate. Each of the four rectangular located elements (9047C and 9048C, see Fig. 2.4) consists of three different cutted quartz crystal plates. Their sensitive axes show in x-, y- and z-direction, respectively. The crystals become electrically polarized when stress is applied to them. The charge is proportional to the force and depending on the direction. It is collected via the electrodes inserted into the stack of crystal plates. The bolts between the balance plates are preloaded to ensure sufficient friction between the elements and the plates. Thus, the shear forces (lift and drag) can be transferred to the piezoelectric elements. The disc with the beam, shown in Fig. 2.3 on the left, is mounted to the top plate of the balance. Four M6 screws around each element are used to provide optimal load transfer. Before the wind tunnel test, the balance is calibrated by applying defined loads in all relevant directions.
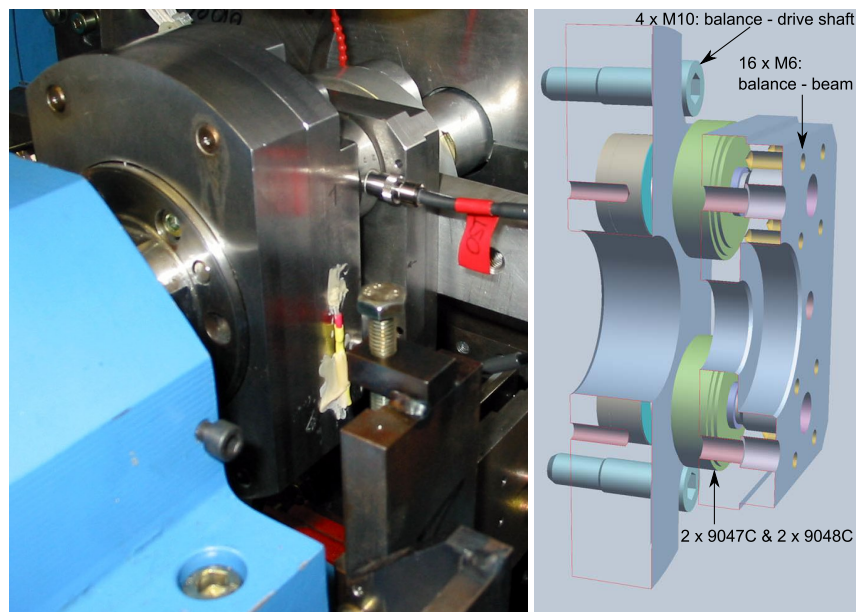

Figure 2.3: **Piecoelectric balance: mounted position (left) sectional view (right)**
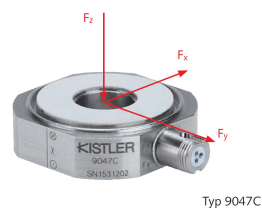

Figure 2.4: **Single piezoelectric element of KISTLER**

Table 2.3: **Technical data of a piezoelectric element Type 9047C, 9048C of KISTLER**

Range	F_x, F_y	kN	-15 ... 15
	F_z	kN	-30 ... 30
	M_x, M_y	Nm	-150 / 150
	M_z	Nm	-150 / 150
Sensitivity	F_x, F_y	pC/N	$\approx$-8.1
	F_z	pC/N	$\approx$-3.7

2.2.3 Differential Pressure Transducers

Fifty-eight differential pressure transducers "Kulite XCQ-132C-093" with a range of $\pm$70 kPa are installed in the model. An extract of the technical data sheet is given in Tab. 2.4.

Table 2.4: **Technical data of the pressure transducer "Kulite XCQ-132C-093"**

Pressure Range	bar	0.7
Full Scale Output (FSO)	mV	100
Natural Frequency	kHz	150
Perpendicular Sensitivity	% FS/g	$1.5 \cdot 10^{-3}$
Transverse Sensitivity	% FS/g	$2.2 \cdot 10^{-4}$
Operating Temperature Range	$^\circ$C	-55 to 120
Compensated Temperature Range	$^\circ$C	25 to 80

The measurement principle of the transducer is based on a strain sensitive membrane. The transducer is glued into a bracket which is connected to the pressure tap on the model surface. Thus, the static pressure p is applied on one side of the membrane. The reference pressure p_∞ is measured in the pressurized plenum and applied on the other side of the membrane via a silicon tube. Dividing the measured pressure difference $\Delta p = p - p_\infty$ by the stagnation pressure yields the pressure coefficient c_p. A daily calibration of the pressure transducers is done by applying discrete pressure levels from the reference side by means of the pressure calibrator unit DPI 510 of the Druckmesstechnik company. The polynomial coefficients of each transducer are defined by a second-order least-square fit. The pressure transducers show a linear behavior between -70 kPa $< p < 70$ kPa. The transducers are temperature compensated between so that no temperature dependency is taken into account in the calibrations. The brackets of the pressure taps at the trailing edge are up to 40 mm long since the transducers need sufficient instrumentation space. Mai [50] has shown that the transfer function of similar sensors with 65 mm extension tubes to the surface pressure have an amplitude ratio $p_{SENS}/p_{REF} = 1.026$ and a phase shift of -2° up to 50 Hz. Due to the short dimensions of these extended brackets and pitching frequencies below $f = 15$ Hz no transfer function between pressure tap and membrane has been taken into account.

2.2.4 Infrared Measurements

Static infrared (IR) measurements have been done on the upper side of the model with a FLIR A655sc IR-camera. Two different objectives with the focal lengths 13.1 mm (angle of view 45° x 33.7°) and 24.6 mm (angle of view 25° x 19°) have been used in the experiment. The camera is placed directly behind a germanium window. However, the optical access is small and shadowing and reflections of the window frame are visible. The maximum resolution of this camera is 640 x 480 px. The integrated uncooled microbolometer detectors are sensitive in the IR spectral range of $\lambda = 7.5 - 14$ μm. The skin friction is proportional to the heat transfer coefficient at the wall [58]. Thus, turbulent and laminar flows have different heat transfer coefficients and can be detected by infrared measurements [59]. Shocks and major flow separation can be detected as well. However, a temperature difference between model and flow is desirable in order to increase the signal to noise ratio.

2.2.5 Pressure Sensitive Paint

The unsteady pressure sensitive paint measurements have been carried out by the DLR's department "Aerodynamic Experiments" of the "Institute of Aerodynamics and Flow Technology". The coating consists of two layers which are subsequently applied. The basecoat layer is a mix of particles and a polymer. The second layer is a mix of luminophore and solvent. The model is illuminated at a specific wavelength where the luminophore molecules absorb light and are promoted to a higher energy state. When these high energetic molecules fall back to the ground state, they emit light. The intensity is dependent on the oxygen partial pressure. Thus, the higher the pressure, the lower is the intensity of the light emitted by the luminophores. The detailed process and its theory are described in detail by Liu and Sullivan [60]. The second layer is quiet porous in order to allow a short reaction time and consequently a high sampling frequency of $f_S = 422$ Hz. The drawback is an averaged roughness of $R_a = 2.3\mu m$ and $R_z = 10.6\mu m$. The start of all measurements is synchronized by a TTL signal.

2.2.6 Function Generator and Data Acquisition (DAQ)

The data acquisition (DAQ) is done by means of a computer of the company Dewetron with two modules of 128 channels of 24-bit Delta-Sigma A/D-converters. The external function generator (Yokogawa FC300) produces the analog input signal for the hydraulic actuator and two digital synchronous square wave signals. One digital transistor-transistor logic (TTL) signal is the excitation frequency, the other is a 512-times oversampled signal of the sampling frequency. The oversampled signal is used in the Dewetron to generate the sampling frequency. The data acquisition starts on a rising edge of the excitation signal and a TTL-signal is generated in the Dewetron which triggers the acquisition of the marker deformation measurement system.
The steady measurement points are recorded at a sampling frequency $f_S = 1200$ Hz. The unsteady measurement points are recorded with 1024 data points per pitching period. Thus, the data can be phase averaged.

2.3 Computational Fluid Dynamics (CFD) Simulations

Three-dimensional CFD simulations have been carried out to design and support the experiment. The edge-based finite volume solver DLR TAU ([61], [62]) has been used for the steady and unsteady Reynolds-averaged Navier-Stokes (RANS) computations. Turbulence closure is achieved by using the SST k-ω turbulence model described in Menter [63]. The inviscid fluxes are discretized using a second order central scheme. An implicit Euler scheme is used for the time discretization, the CLF number is set to $CFL = 10$. These settings lead to a fast but stable convergence. The converged steady solution is used as the initial condition for the unsteady computations. The dual time-stepping approach is applied with 2000 physical time steps per period. The computational performance was enhanced by means of a two-grid V-cycle multigrid method. The domain was split into up to 128 blocks for parallel computation. Since fluid-structure interaction (FSI) simulations, presented in [64] and [49] showed no significant differences in comparison to the CFD computations with the rigid contour, the faster converging CFD computations are presented in this thesis only. The inflow vector is rotated sinusoidally for the unsteady computations. This setup is compared to a setup with grid deformation technique in Section 3.5.1. Different grids, their convergence and the detailed boundary conditions are presented in Section 3.5.1.

2.4 Applied Finite Element Methods (FE)

A high-fidelity three-dimensional finite element model (Section 3.3) was built for the detailed loads analysis of the wind tunnel model [65]. The modeling and analyses were carried out by means of ANSYS$^{\text{TM}}$ [66]. As will be shown in Section 5.2, the deflections of the wind tunnel model are small because of the desired stiff design. Thus, a linear finite element method approach was considered to be sufficient. The maximum aerodynamic loads $\mathbf{f}_a$ calculated by means of CFD are inserted into the general equation of motion

$$\mathbf{M\ddot{u}} + \mathbf{D\dot{u}} + \mathbf{Ku} = \mathbf{f}_a + \mathbf{f}_g + \mathbf{f}_I \qquad (2.2)$$

In the applied linear static strength analysis, the mass $\mathbf{M}$, the damping of the structure $\mathbf{D}$ and the inertia forces $\mathbf{f}_I$ are neglected which reduces Eq.2.2 to

$$\mathbf{Ku} = \mathbf{f}_a + \mathbf{f}_g. \qquad (2.3)$$

Due to the small weight of the model, the gravitational forces $\mathbf{f}_g$ are negligible as well. The aerodynamic forces calculated on the CFD meshgrid $\mathbf{f}_a$ are interpolated on the surface nodes of the structural finite element model by

$$\mathbf{f}_s = \mathbf{H}^T \mathbf{f}_a \qquad (2.4)$$

The transposed coupling matrix $\mathbf{H}^T$ is generated by using a radial basis function approach as presented in [75]. Finally, the linear static strength analysis is done by solving

$$\mathbf{Ku} = \mathbf{f}_s. \qquad (2.5)$$

The inertia forces $\mathbf{f}_I$ which are caused by the pitching motion are generally not negligible, so that a harmonic analysis is done to incorporate the forces or stresses caused by the strong angular accelerations. This solution is superposed to the static solution from Eq.2.5 where only the pure aerodynamic forces $\mathbf{f}_a$ are taken into account. In case of a pure harmonic motion

$$\mathbf{u} = \hat{\mathbf{u}} \cdot e^{j\omega t} \tag{2.6}$$

given by the hydraulic test rig this equation becomes

$$\left(-\omega^2 \mathbf{M} + j\omega \mathbf{D} + \mathbf{K}\right)\hat{\mathbf{u}} = 0. \tag{2.7}$$

Furthermore, the damping is neglected and the y-rotation constraint is adapted. The equation of motion is split into two parts, namely, unknown displacements $\mathbf{u}_a$ and prescribed displacements $\mathbf{u}_b$.

$$\begin{pmatrix} \mathbf{M}_{aa} & \mathbf{M}_{ab} \\ \mathbf{M}_{ba} & \mathbf{M}_{bb} \end{pmatrix} \begin{pmatrix} \ddot{\mathbf{u}}_a \\ \ddot{\mathbf{u}}_b \end{pmatrix} + \begin{pmatrix} \mathbf{K}_{aa} & \mathbf{K}_{ab} \\ \mathbf{K}_{ba} & \mathbf{K}_{bb} \end{pmatrix} \begin{pmatrix} \mathbf{u}_a \\ \mathbf{u}_b \end{pmatrix} = \mathbf{0}. \tag{2.8}$$

With the harmonic approach

$$\mathbf{u} = \hat{\mathbf{u}} \cdot e^{j\omega t} \tag{2.9}$$

the equations can be rewritten as

$$\left(-\omega^2 \mathbf{M}_{aa} + \mathbf{K}_{aa}\right)\hat{\mathbf{u}}_a = \left(\omega^2 \mathbf{M}_{ab} - \mathbf{K}_{ab}\right)\hat{\mathbf{u}}_b \tag{2.10}$$

and

$$\left(-\omega^2 \mathbf{M}_{ba} + \mathbf{K}_{ba}\right)\hat{\mathbf{u}}_a = \left(\omega^2 \mathbf{M}_{bb} - \mathbf{K}_{bb}\right)\hat{\mathbf{u}}_b. \tag{2.11}$$

As one can see from the equations above, the resulting $\hat{\mathbf{u}}_a$ is generally complex

$$\hat{\mathbf{u}}_a = \hat{\mathbf{u}}_{a,Re} + j \cdot \hat{\mathbf{u}}_{a,Im}. \tag{2.12}$$

Inserting Equation (2.12) into Equation (2.9) and extracting the physically relevant real part leads to

$$\mathbf{u}_a(t) = \Re(\hat{\mathbf{u}}_a e^{j\omega t}) = \hat{\mathbf{u}}_{a,Re} \cdot \cos(\omega t) - \hat{\mathbf{u}}_{a,Im} \cdot \sin(\omega t) \tag{2.13}$$

Finally, the stresses are derived from the overall deformation [65]. The results of the stress analysis are shown in Section 3.5.2.

A undamped modal analysis is performed in order to determine the eigenfrequencies ω_i and the mode shapes ϕ_i of the wind tunnel model. Using the harmonic approach, the classical eigenvalue problem

$$\mathbf{K}\phi_i = \omega_i^2 \mathbf{M}\phi_i \tag{2.14}$$

is solved using the Block Lanczos method [67]. The results are compared to the experimental results in Section 3.4.

3 Helicopter Rotor Blade Tip Model

The geometry of the blade tip wind tunnel model has been derived from the parametrized AIRBUS-helicopter patent [68]. It was adapted to the experimental boundary conditions in the DNW-TWG. The structural components of the carbon fiber reinforced plastic (CFRP) model were chosen not only for stability but also for instrumentation purposes. A high fidelity 3D finite element model (FE) has been established. An experimental modal analysis has been carried out to validate the numerical model. Finally, a strength analysis of the complex CFRP model could be carried out which is demanded by the wind tunnel operator. Most of the figures presented in this chapter have been published in [69] and [49]

3.1 Aerodynamic Design - Geometry

The tip vortex reduces the effective angle of attack and dynamic stall usually appears at around 70-90% radial position of a real helicopter rotor blade. Thus, a high aspect ratio is required for the investigation of dynamic stall at a blade tip model. Since decreasing the chord length leads to a reduced Reynolds number and instrumentation space, a trade-off had to be made. A maximum span width of $s = 750$ mm is chosen in order to minimize the interaction of the blade tip vortex and the wind tunnel wall. Thus, the aspect ratio yields $AR = 4.5$ dividing the span by the chord length at the root ($c_{root} = 166.5$ mm). The Reynolds number and the reduced frequency are based on the reference chord length $c_{ref} = 160$ mm.

The top view of the planform is shown in Fig.3.1. The radial sweep angle shown in Fig. 3.1 is calculated with regard to the quarter chord line. The forward sweep of $\Lambda \approx 11°$ begins at $r = 200$ mm and ends at $r = 390$ mm. In the linear backward swept part ($\Lambda = 25.7°$), the chord length reduces from $c = 166.5$ mm to $c = 106$ mm at $r = 638$ mm. The parabolic tip leads to a minimal tip chord length of $c_{min} = 45$ mm. In the swept parts of the blade tip the local Mach number is reduced. Thus, the effects of compressibility are reduced, shocks are diffused. The combination of forward and backward sweep keeps the aerodynamic center and the center of gravity near the quarter chord feathering axis of the blade. Thus, vibrations and pitch link loads can be reduced. The pitch axis of the wind tunnel model is positioned at the quarter-chord of the root section. The axis is orthogonal to the wind tunnel wall. A gap of 1.5 mm between axis and wall and between root airfoil and wall ensures contactless operation. As shown in Fig. 2.1, aerodynamic covering plates are fixed on the root in order to reduce cross flow effects from the plenum. Since the outer part of a rotor blade experiences a higher inflow velocity than the inner part, the twist
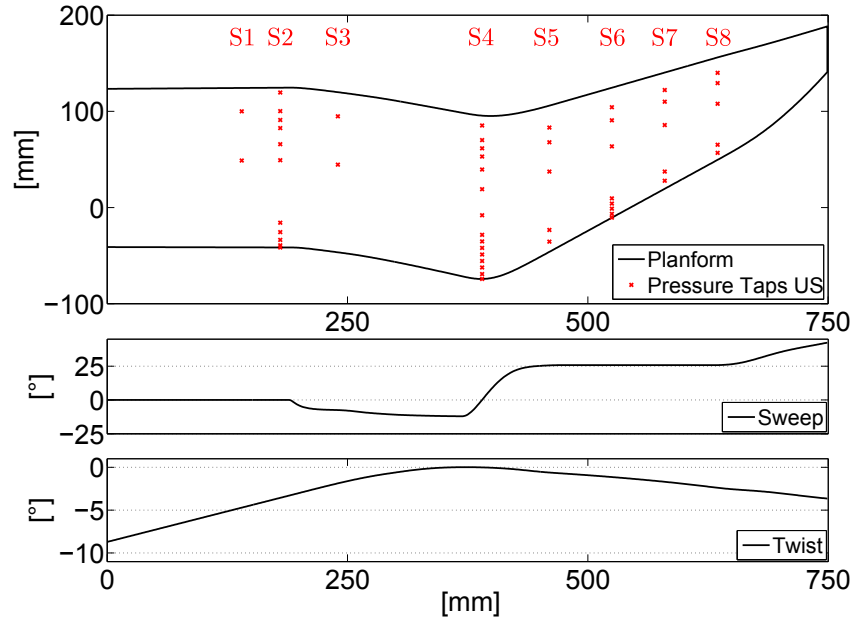
Figure 3.1: **Planform, sweep and twist; pressure transducers upper side (US)**

angle usually decreases from the root to the tip. Thus, a more homogeneous lift distribution is employed in spanwise direction. In case of the pitching blade tip, the twist is decreased at the root so that dynamic stall is not triggered by separation at the wind tunnel wall. The position of inboard dynamic stall is expected to move to a radial position of $r \approx 250$ mm where forward sweep begins and the sectional lift is at its maximum. Anhedral is not incorporated in the model in order to reduce measurement complexity.

The EDI-M112 airfoil is used from the root to the beginning of the forward sweep. It has an airfoil thickness to chord ratio of 12 %. According to Gardner et al. [24], it shows soft trailing edge stall at low Mach numbers ($0.3 \leq Ma \leq 0.4$). The EDI-109 airfoil is used for the forward/backward swept part. It has a 9 percent airfoil thickness to chord ratio and is well suited for higher Mach numbers [24]. A low drag coefficient is expected due to the lower airfoil thickness and the tapered backward swept part of the blade. A not closer specified splining is used in between the two airfoils. Both airfoils are oriented in streamwise direction. At the outer part of the blade tip, the trailing edge is slightly thickened to maintain a minimum thickness of $t_{TE} = 0.5$ mm. The pressure is measured at eight spanwise sections (S1-S8) by means of 58 unsteady pressure transducers, depicted as red points in Fig. 3.1. A drawing of the instrumentation of the upper side of the model is shown in Fig. 3.2. Besides the 51 pressure transducers which are installed in the upper side of the model, two accelerometers in x- and z-direction are positioned at section A. A few distributers can be seen where the reference tubes of the pressure transducers are brought together. Only four reference tubes leave the model. The drawing becomes more clear with a look on the structural components of the model.
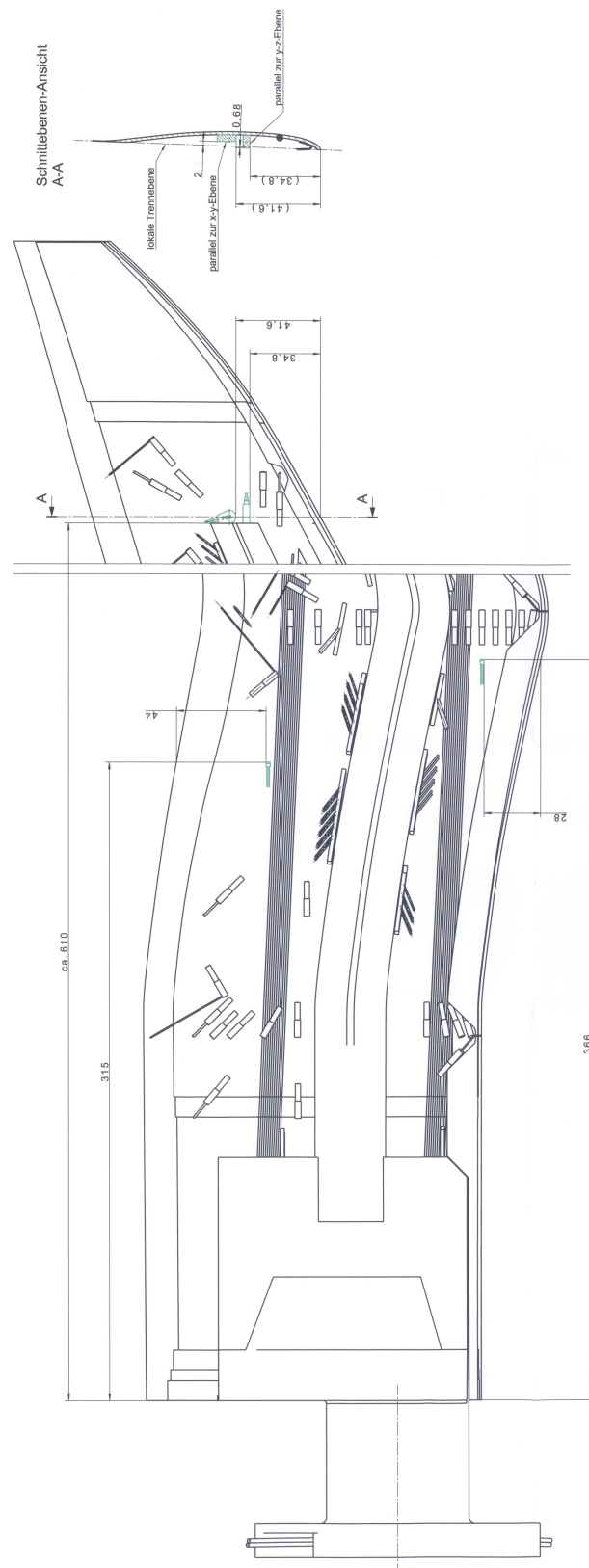
Figure 3.2: **Drawing of the instrumented upper side of the wind tunnel model**

3.2 Structural Components and Manufacturing Model

The pitching wind tunnel model is in large part made out of carbon fiber reinforced plastic (CFRP). Thus, a high bending and torsional stiffness, low weight, and sufficient mounting space for instrumentation are obtained. A strong bending-torsion coupling and a high mass moment of inertia around the pitching axis due to the planform are expected [42]. A specific bending-torsion coupling in order to reduce the positive elastic twist is another design goal. Thus, the stability is increased. The high bending stiffness is required since no centrifugal stiffening effects as under real flight conditions occur in the experiment.
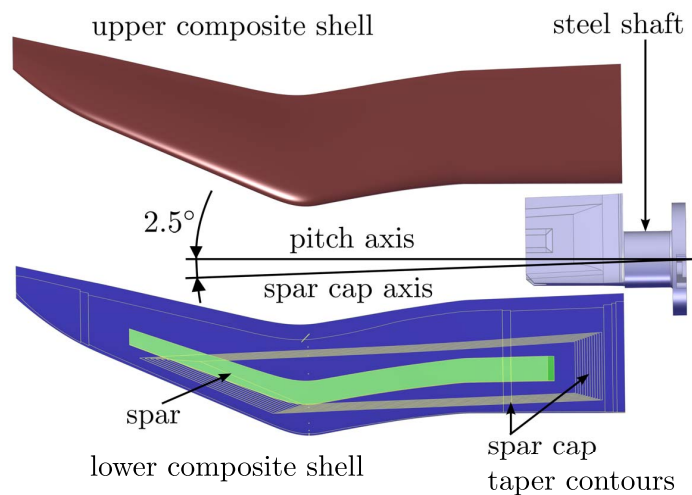

Figure 3.3: **Catia V5 model of the rotor blade tip**

The wind tunnel model is built up of a lower and an upper carbon composite shell which are bonded to a spar and a steel shaft (Figs. 3.3 and 3.4). At the leading edge the lower and upper shell are connected by a leading edge support structure, shown in Fig. 3.5. In Fig. 3.4 on the right, the two CFRP half shells with integrated spar caps are shown. They carry the main bending loads. A central spar resists shear forces and prevents buckling. Torsional loads are carried by the closed shells and the spar. A hollow steel shaft is adhesively connected to the shells and the spar at the model root and transfers the loads to the hydraulic oscillation rig. Vacuum bag molding is used for all composite parts of the model.

Aluminium Molds

The upper and lower half shell are hand layed into the aluminum molds, shown in Fig. 3.4 on the left. The high surface quality with $R_z < 3\mu m$ and the reusability along with the robustness compensate the high costs of the mold. Each mold has five hollow, removable inserts located at the main instrumented sections. The holes for the discrete pressure measurements with a diameter $d = 0.3$ mm are drilled from the half shell through the hollow inserts. Thus, the pressure
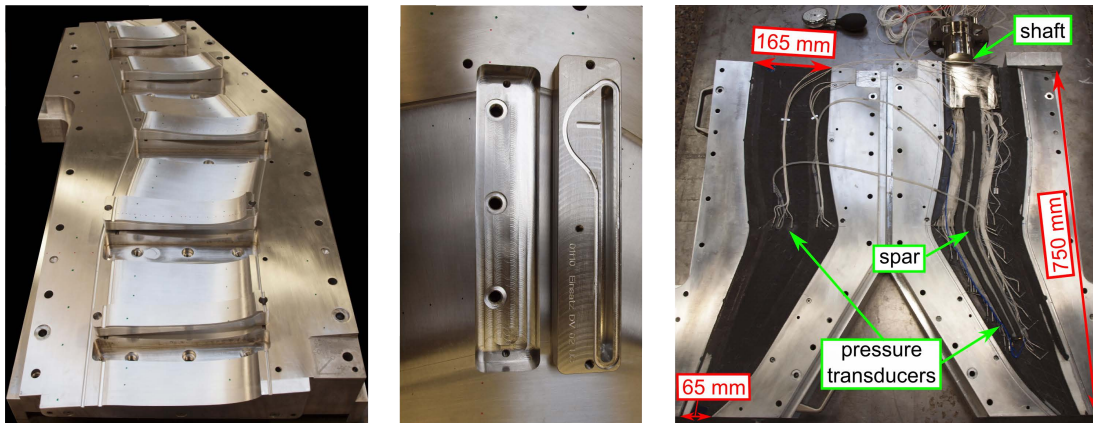
Figure 3.4: **Aluminium mold with removable inserts; instrumented half shells**

transducers are not destroyed by overpressure when inserting them into the brackets (Fig. 3.5). Furthermore, the leak-tightness of the installed transducers can be tested by applying pressure through the brackets while keeping the shells in the molds. If the half shells detach accidentally during the instrumentation process the inserts can be removed from the mold and the shells can be retained in the mold by partial vacuum for the final bonding procedure.
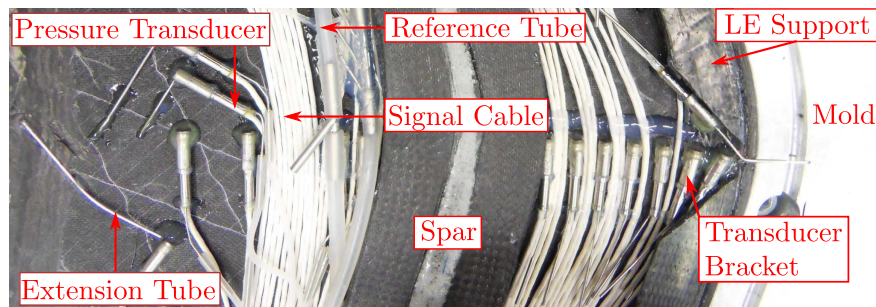
Figure 3.5: **Detail of the instrumentation at the forward/backward kink (S4)**

Carbon Fiber Half Shells

The high modulus, unidirectional M46J-lamina and the epoxy LR385 are used for the half shells. A maximum fiber volume fraction of 50 % is chosen for the complex geometry. Thus, the risk of dry spots is decreased. The ply layout is listed in Table 3.1. The integrated spar caps (Ply 7-18) are orientated $2.5°$ in forward direction in order to follow the spar contour and enforce the bending-torsion coupling. The spar caps are 8:1 tapered in chordwise direction and taper out in spanwise direction right behind the kink. The position of the spar caps is shown in Fig. 3.3. A spanwise tapering of 26:1 is used at the connection to the steel shaft. Hence, stress concentrations are reduced and the loads are smoothly transferred from the half shells to the steel shaft [70]. Plies 3-4 and 21-22 are dropped at the beginning of the parabolic tip since loads decrease in tip direction and space for instrumentation is limited due to the tapered planform. The first six and the last six plies as well as the integrated spar caps are laminated in separate

steps. The correct fiber volume fraction is essential to ensure strength and the correct thickness for a perfect integration of steel shaft and spar. An adhesive gap of 0.4 mm thickness between the components is not exceeded. Before the shaft and the spar are bonded to the upper shell, the holes for the pressure transducers and the corresponding brackets are drilled. The leading edge (LE) support structure is glued in the upper shell, before the pressure transducer brackets are glued in the half shells with epoxy. Cut outs at the positions of the transducers and the brackets are provided. Vibration resistant silicone is used to glue the pressure transducers into the brackets.

Table 3.1: **Laminate of outer shells with M46J plies**

Number	Thickness in mm	Orientation in °
1	0.115	-45
2	0.115	45
3	0.115	90
4	0.115	0
5	0.115	23
6	0.115	-23
7-18	1.38	-2.5
19	0.115	-23
20	0.115	23
21	0.115	0
22	0.115	90
23	0.115	45
24	0.115	-45

Leading Edge Support Structure

At the beginning of the manufacturing of the leading edge support structure, a support shell is required. This is laminated in the front part of one original aluminum mold. A carbon half mold is laminated on the outer contour of this support shell and connected to the other original aluminum mold. Then, the leading edge support structure is laminated in the U-contour of the original aluminum mold and the connected carbon front mold. The flexible weave Style469 has been used since it remains in the small radii during the lamination process.

Spar

The contour of the central spar follows the contour of the blade tip. The milled foam core (ROHACELL) is covered with two C-shapes $\pm 45°$ weave Style469, shown in Fig. 3.6. In the middle of the foam core a lower and an upper bump define the end of the C-shapes. Furthermore, the milled bumps define the thickness limit of the spar for an optimal integration into the half shells. The weave is not easy to be fixed on the core with its small dimensions and radii. Thus,
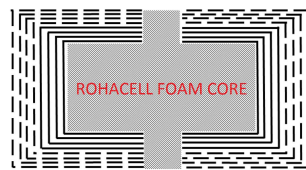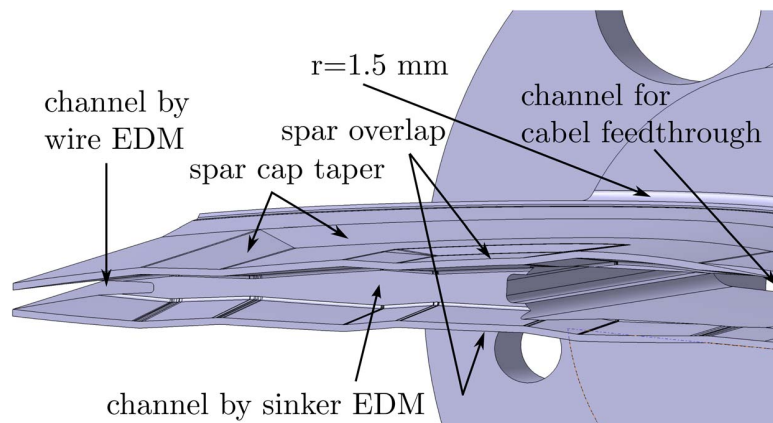
Figure 3.6: **Cross section of the spar**

Figure 3.7: **42CrMo4 steel shaft with tapered channels**

an exact fiber volume fracture of =50% is difficult to guarantee. Only one pressure transducer is placed in the region of the spar in order to minimize any weakening of the spar. At this position, a notch is cut in the foam. For a homogeneous stress distribution the spar has a connection to the steel shaft on the upper and lower side. A plastic support construction is used to laminate the upper connection on the spar. Then, the spar with the upper connection is bonded to the upper shell. Finally, the steel shaft is glued in place and the connection on the lower side is laminated.

Steel Shaft and Connection to the Test Rig

The steel shaft is milled of a 42CrMo4 steel block. One main channel is used for cable feedthrough. One spanwise and chordwise channel reduce stress concentrations and save weight. The steel shaft has a corner radius of $r = 1.5$ mm. Thus, stress concentrations are minimized. Milled slots are provided for the spar connection. The steel shaft is fixed with 4 M10 screws to a distance disc with cantilever beams, shown in Fig. 2.1. Two hole patterns are provided for different angles of incidence. The distance disc is fixed with 16xM6 screws to the piezoelectric balance on the hydraulic test oscillation rig. An internal centering is provided between the balance and the disc, an external centering is provided between the disc and the steel shaft.

Final Bonding Procedure and Surface Quality

The model is cured for 15 hours at 55°C after the final bonding procedure. An average thickening of the outer contour of about 0.1 mm can be observed. One measured spanwise cross section of the upper surface is shown in Fig. 3.8. No signs of the inserts of the mold can be seen.
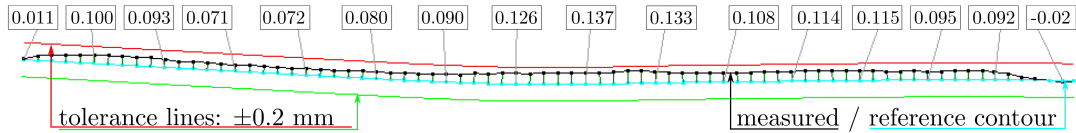
Figure 3.8: **Measured upper surface along the span, 15 mm in front of the TE**

3.3 FE model

High fidelity finite element (FE) models have been established and investigated by means of ANSYS^{TM} [66]. Two different modeling approaches which have been used for the modal and strength analysis are presented in the following. For both approaches, the laminate is modeled using shell elements which have three translational and three rotational degrees of freedom at each node. They are described by the first-order shear-deformation theory (Mindlin-Reissner). The spar, the bonding and the shaft are modeled using solid elements which have three translational degrees of freedom at each node. The material properties and deformations are considered linear.

The structured shell elements simulating the half shells are placed on the outer contour of the model. There is a gap between the outer contour and the inner parts. This gap corresponds to the laminate thickness.

Figure 3.9: **First finite element (FE) model of the blade tip - V1**

For the first modeling approach V1, shown in Fig. 3.9, the gap is closed by volume elements with the properties of the adhesive. The modeling is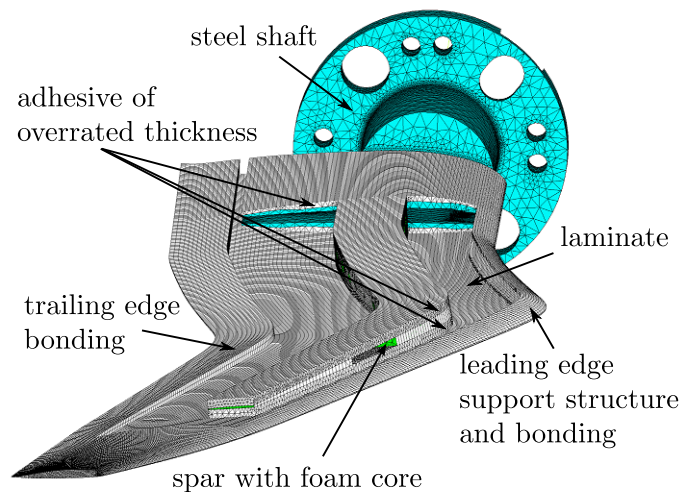 easy to accomplish but leads to an adhesion thickness which is up to 10 times too thick. Thus, the simulated mass of $m_{V1} = 4.9$ is higher than the real model mass of $m = 4.6$ kg although the instrumentation have not been taken into account in the finite element model. Furthermore, stress peaks in the adhesive might be underestimated. Holes for cable-feedthrough have been integrated in the spar. They have been eliminated in the final version V2 since considerable stress peaks occurred at the holes.
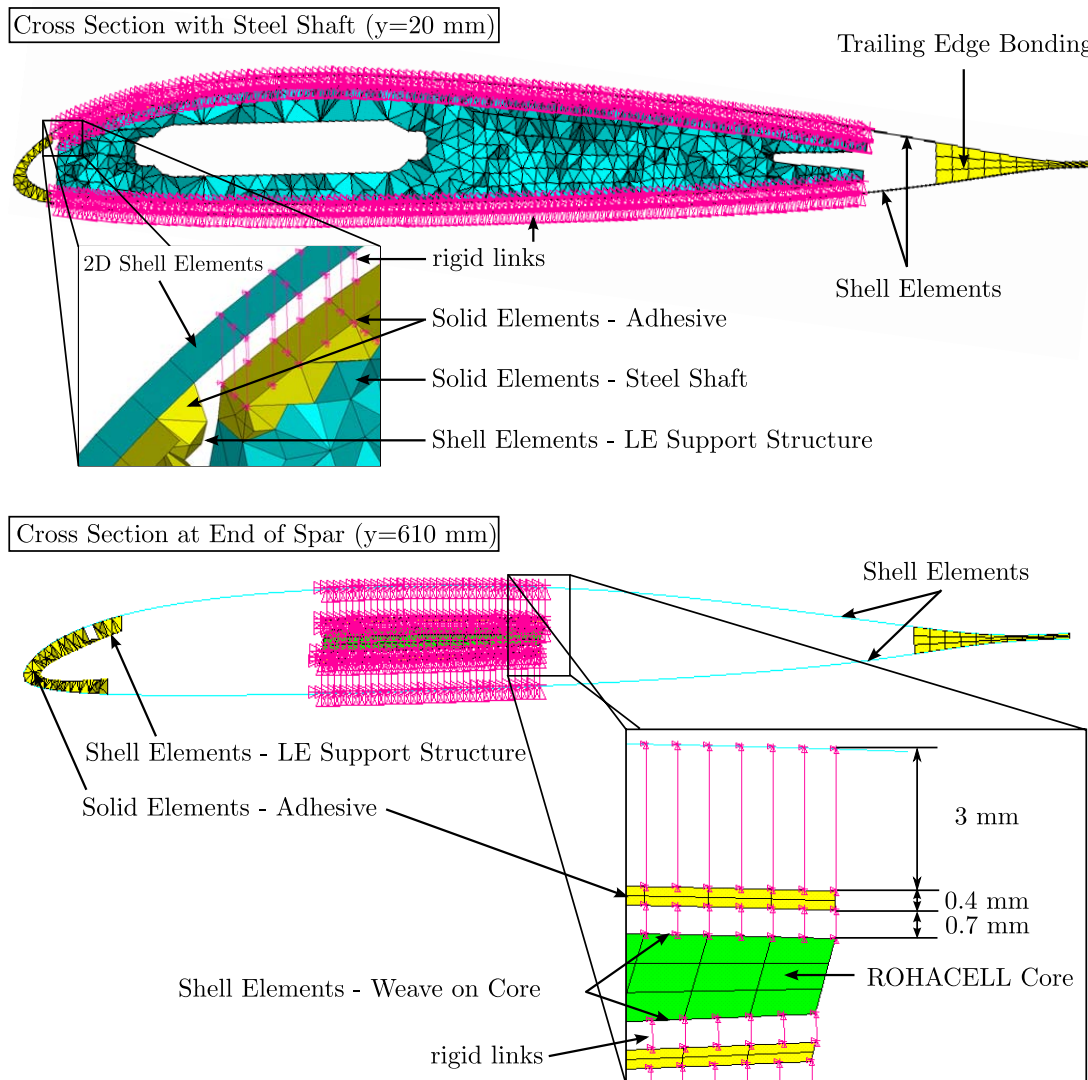
Figure 3.10: **Final FE model of the blade tip - V2 (distorted illustration of the airfoils)**

For the more sophisticated modeling approach V2, shown in Fig. 3.10, the adhesive of 0.3 mm real thickness between the half shells and the steel shaft is simulated using unstructured solid elements. They are placed on the shaft and have a structured surface on their free faces. They have the same node distribution as the structured elements simulating the half shells. The nodes are linked by rigid links with the length of the final laminate thickness.

The weave of the spar is simulated using structured shell elements which are placed on the faces of the structured solid elements simulating the foam core. The opposite nodes of the solid elements representing the adhesive are linked to the nodes of the spar via a distance equal to the weave thickness t=0.7 mm by rigid links. The nodes on the other side of the t=0.4 mm thick adhesive are linked by rigid links to the nodes of the half shell elements. The leading edge support structure is modeled with shell elements which are connected to the shell elements of the half shells by solid elements. These solid elements have the properties of the adhesive. However, due to this modeling the bonding thickness is overestimated. The simulated mass of $m_{V2} = 4.2$ kg is 0.4 kg lower than the real model mass $m = 4.6$ kg.
The date of the two modeling approaches V1 and V2 are compared in Table 3.2.

Table 3.2: **Data of the two finite element models V1 and V2**

-	V1	V2
Adhesive	too thick	realistic
Connection 2D-3D-Elem.	3D-solids (epoxy)	rigid links
Mass in kg	4.88	4.23
No. of shells	65k	108k
No. of solids	638k	870k

Beam elements are used for modeling the drive shaft. At the position of the bearings the nodes are fixed: one is simulated as a floating bearing with fixed displacements in x- and z-direction, the other is simulated as a fixed bearing with all degrees of freedom fixed (Fig. 3.11).

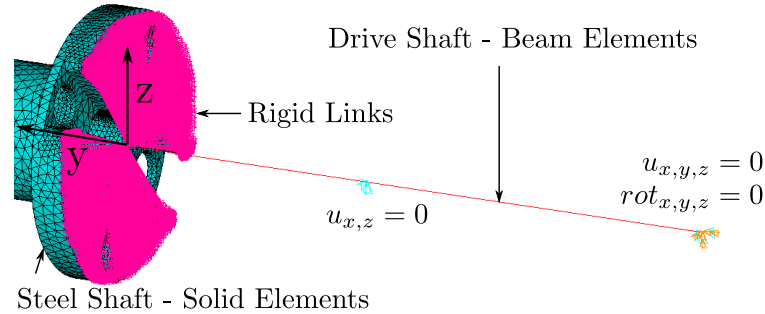Figure 3.11: **FE - modeling of the wind tunnel boundary condition**

The cross section of the beam elements reflects the cross section of the drive shaft. However, the disc with the cantilever beam, shown in Fig. 2.1 is not included in the FE model. The beam element closest to the model is connected via rigid links to the solid elements of the steel shaft. This might lead to a too stiff behavior of the numerical model.

3.4 Structural Dynamics of the Wind Tunnel Model

The identification of the structural dynamics of the the wind tunnel model has been carried out by the DLR department AE-SAS. During the first experimental modal analysis, the model was clamped on a massive steel block. This test was used to validate the finite element model of the blade tip. The second test was carried out in the wind tunnel in order to qualify the influence of the hydraulic oscillation rig on the structural behavior of the model.

3.4.1 Experimental Modal Analysis - Model clamped on a Massive Steel Block

The first experimental modal analysis has been done before the wind tunnel test. The model was clamped on a steel block and instrumented with accelerometers, as shown in Fig.3.12. The numerical boundary condition represents the reality as good as possible.
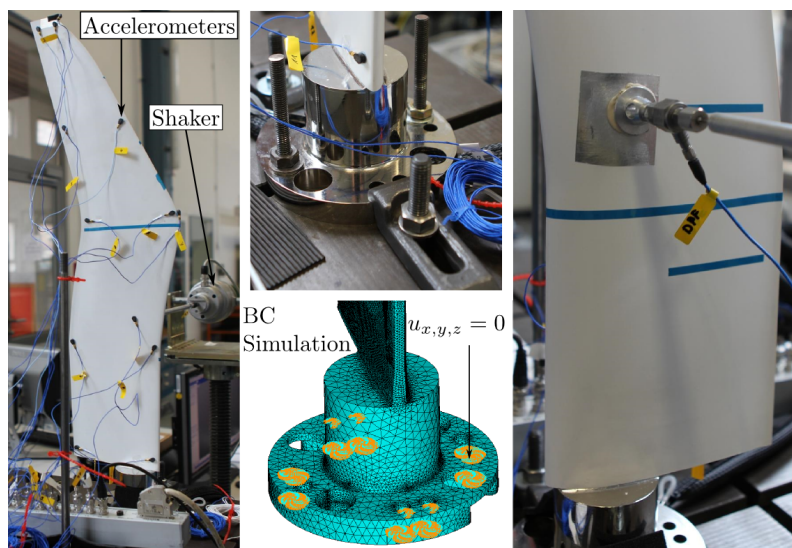
Figure 3.12: **Model on steel block; FE modeling of the clamping condition**

Two different excitation methods were used: the first one is an impact hammer, the second one is the shaker, shown in Fig.3.12. The two methods yield approximately the same results. The experimental eigenfrequencies show an excellent agreement to the numerical eigenfrequencies of the final modeling approach V2, depicted in Fig,. As shown in Table 3.3, even the third eigenfrequency at $f = 275$ Hz shows a deviation of less than 10 %. The eigenfrequencies of the modeling approach V1, depicted in Fig. , are lower than the experimental eigenfrequencies due to the higher weight and the reduced stiffness. Even for the advanced modeling approach V1, the results could be further improved integrating the instrumentation into the FE model. In Fig. 3.13 the experimental mode shapes (blue arrows) of V1 are compared to the numerical ones (contour). Therefore, the modal assurance criterion (MAC), which is described in [71], is used.

Table 3.3: **Eigenfrequencies of the model on the steel block [Hz]**

Mode No	1	2	3	4	5	6
Experimental	69.6	196	275	434	463	729
Numerical V1	62.0	175	258	408	435	674
Numerical V2	69.4	198	299	429	499	752

The MAC-coefficient correlates the numerical and experimental mode shapes. Even for the third mode shape the coefficient shows an agreement higher than 93 %. Although this modeshape has slight torsional parts the first real torsional eigenmode is at $f = 434$ Hz. In general, the high eigenfrequencies confirm the stiff design of the model and should not be excited by the pitching frequency.
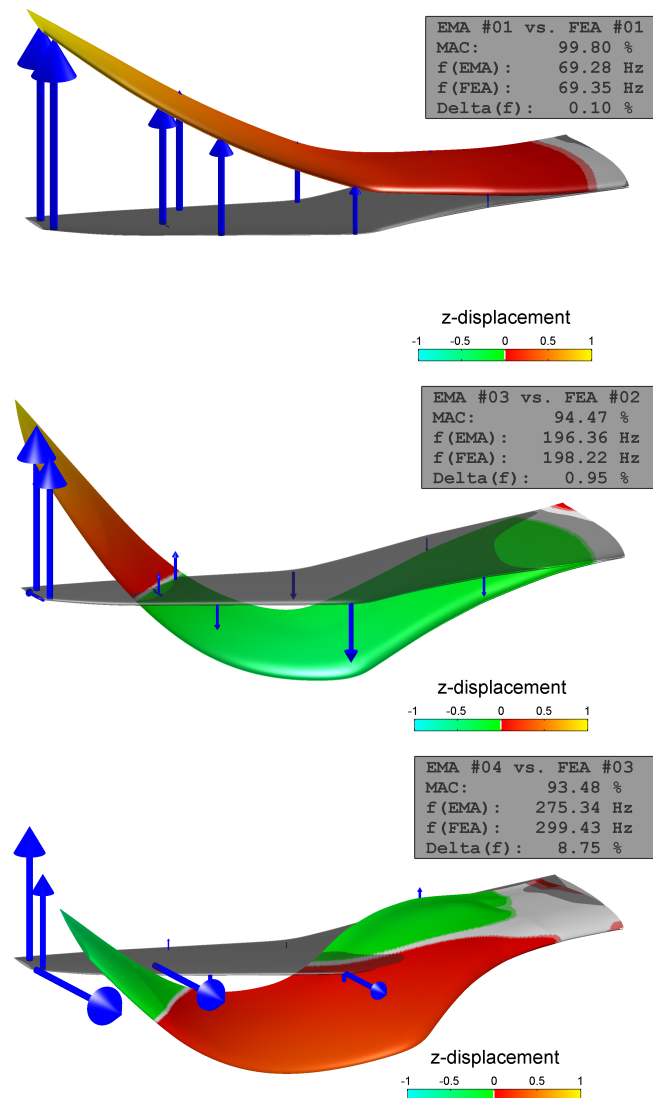

Figure 3.13: **First three experimental and numerical (blue arrows) modeshapes**

3.4.2 Experimental Modal Analysis - Model in the Transonic Wind Tunnel

As shown in Fig.3.14, the final experimental modal analysis is carried out in the wind tunnel.
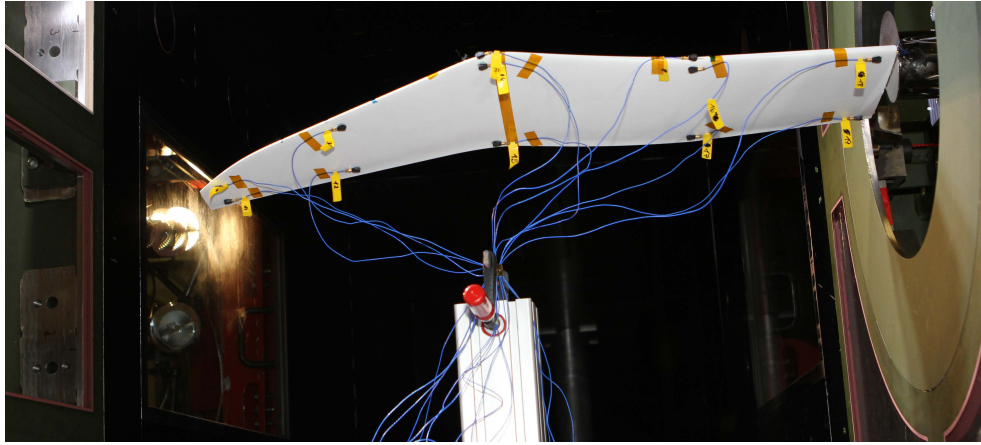
Figure 3.14: **Experimental modal analysis in the transonic wind tunnel**

The accelerometers are installed at the same positions as in the modal analysis on the steel block. The different boundary conditions change the eigenfrequencies significantly. As shown in Table 3.4, they are generally lowered compared to the eigenfrequencies in Table 3.3.

Table 3.4: **Eigenfrequencies of the model in the wind tunnel [Hz]**

Mode No	1	2	3	4	5	6
Experimental	67.3	153	186	273	466	515
Numerical V1	60.3	158	176	325	471	595
Numerical V2	67.7	181	201	369	430	530

This is caused by the attached axis. Still, the eigenfrequencies are well separated. The computations V2 overpredict the eigenfrequencies which might by caused the rigid connection of drive shaft and steel shaft, presented in Fig. 3.11. Since the modeling of the connection is the same for V1, the eigenfrequencies 2-5 are coincidently closer to experimental results. The mode shapes are very similar to the mode shapes shown in Fig. 3.13.

3.5 Loads Analysis

The loads analysis in this thesis consists of unsteady CFD computations and a strength analysis where the maximum CFD-loads are applied to the Finite Element Model. The harmonic motion of the pitch oscillations is superimposed to incorporate the inertial forces. Finally, the stresses in each ply are determined and compared to the failure criterions of Puck [72]. Furthermore, the stresses in the bonding and the steel shaft are determined.

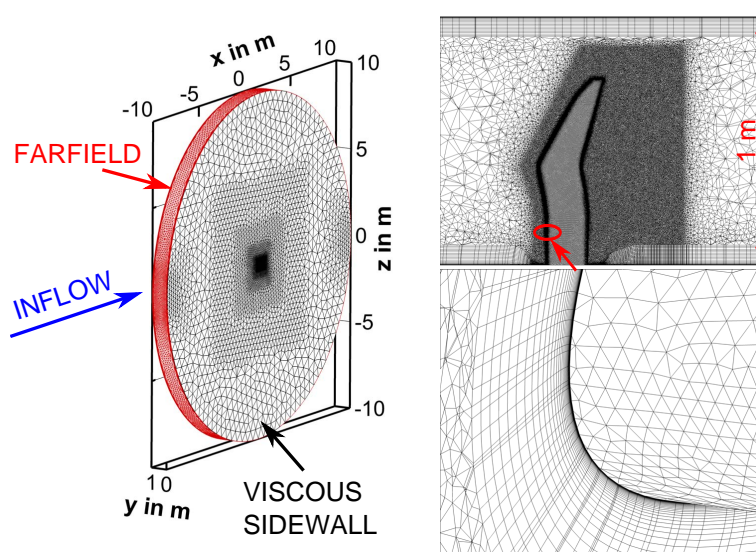### 3.5.1 CFD Simulations - Setup and Load Cases for the Strength Analysis

Figure 3.15: **CFD-grid Version G4; geometric properties**

Preliminary CFD simulations have been carried out in order to determine the loads for the strength analysis. However, these test cases could not be experimentally investigated due to the limitations of the hydraulic test oscillation rig. Thus, pressure distributions and local flow phenomena are not investigated in detail in this section. In Sections 4 and 5 different test cases, which could be directly compared to the experimental results, are shown.

In the following, the final computational setup is presented. Furthermore, the global loads of the test cases LC-S1$_{pre}$ - LC-DS2$_{pre}$ which were exclusively performed for the strength analysis are shown.

At the beginning, four different grid have been used for a mesh convergence study at a static angle of attack of $\alpha = 10°$ at $Ma = 0.4$ and $Re = 1.6 \cdot 10^6$. Steady, fully turbulent RANS computations with the SST k-ω turbulence model [63] have been carried out. All grids have the same boundary conditions and geometric properties. Version G4 of the grid is depicted in Fig. 3.15. The grid depth equals the wind tunnel depth of 1 m. Viscous sidewalls and a farfield with radius $r = 10$ m (60 times the chord length) are used as boundary conditions. For this setup the growth of the sidewall boundary layers corresponds with the inflow conditions of the TWG [73]. The root airfoil section is connected to the viscous wall and the gap of 1.5 mm is not taken into account. The grid properties and the global coefficients of version G1-G4 are shown in Table 3.5.

Above grid G2 only minor changes in the aerodynamic coefficients are given. A thorough grid convergence study for unsteady cases at high angles of attack is not possible to be carried out in a reasonable time with a reasonable budget. Grid G4, presented in Fig. 3.15, is used for all final steady and unsteady simulations. For unsteady cases this grid has the best convergence behavior. The surface resolution is higher than for grid G2 and surface nodes are more physically distributed than they are in grid G1. Grid G3 was neglected because of its huge size. The value of $y^+_{max} > 1$ occurs only in very small regions of the domain. Furthermore, the Reynolds number was decreased to $Re = 1.2 \cdot 10^6$ in the structural design process which consequently leads to lower values of y^+.

Table 3.5: **LC-S1**$_{pre}$ **computed with different Grids**

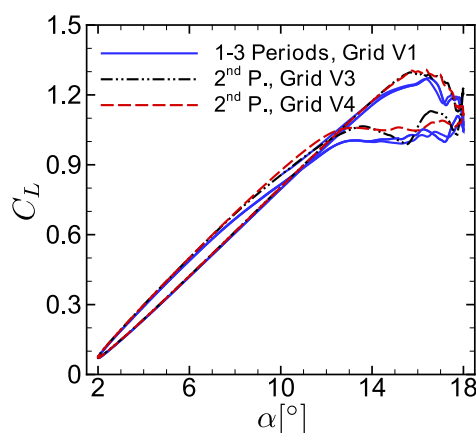|	G1	G2	G3	G4
No. of Points ($\cdot 10^6$)	9.0	6.7	11.1	8.3
No. of Surf. P.	170k	109k	182k	127k
No. of Surf. TE P.	15.6k	2.1k	16.3k	5.4k
No. of B.-Lay.	30	40	40	40
max. y^+	1.49	1.35	1.85	1.42
C_L	0.837	0.849	0.850	0.849
C_D	0.038	0.036	0.036	0.036
C_{My}	-0.065	-0.068	-0.069	-0.068

Figure 3.16: **LC-DS1**$_{pre}$**:** $Ma = 0.4$, $Re = 1.6 \cdot 10^6$**;** $C_L - \alpha$ **distribution for different grids**

In the second step, unsteady RANS computations with a rotating grid are performed. This configuration leads to fast converging results, starting with a converged steady solution. A single period is simulated with 2000 physical time steps per period and 100-1000 inner iterations, depending on a Cauchy convergence criterion. The lift distribution of the first unsteady test case LC-DS1$_{pre}$ is shown in Fig. 3.16. The Mach number is $Ma = 0.4$, the Reynolds number is $Re = 1.6 \cdot 10^6$ and the reduced pitching frequency is $k = 0.05$. In order to check the influence of the different grids, LC-DS1$_{pre}$ is simulated with grid G1, G3 and G4 (Fig. 3.16). More than two periods are only calculated with grid G1 in order to check periodicity. The second period is already in good agreement with the third period, as can be seen in Fig. 3.16. The grids G3 and G4 show a better agreement in the lift coefficient peaks $C_{L,peak}$, which are significantly higher

than in the steady case. However, the reattachment region differs significantly and a second lift peak is only resolved by grid G3, which is probably less dissipative. Due to the lower number points and its numerical robustness, grid G4 is used for all further simulations. The unsteady load case presented above, yields a maximum global force $F_{Z,max} = 1766$ N. This leads to a violation of the safety margin in the FE analysis. Therefore, the Reynolds number is reduced by 25% for the load case LC-DS2$_{pre}$ which was used for the final strength analysis, shown in Fig. 3.17. The maximum unsteady loads are statically applied on the FE model in the strength analysis.
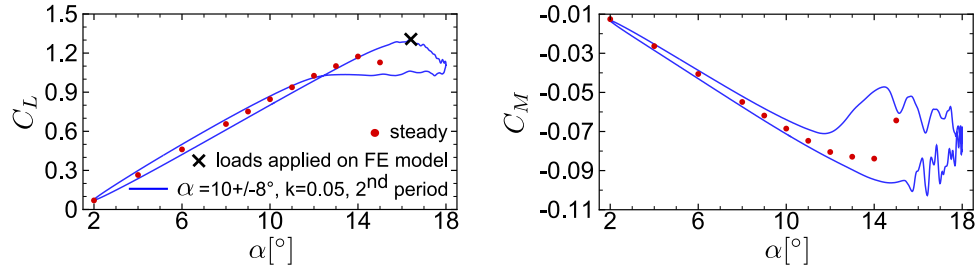

Figure 3.17: **Load case LC-DS2**$_{pre}$ **for the final strength analysis -** $Ma = 0.4$**,** $Re = 1.200.000$

The delayed and increased lift peak in comparison to the steady case is clearly visible. There is no significant global pitching moment peak in the $C_{My} - \alpha$ distribution as presented for the two-dimensional cases in Gardner et al. [24].

The rotating viscous sidewalls do not match the non-rotating wind tunnel walls since they introduce momentum into the domain (no-slip condition). Therefore, unsteady RANS computations with grid deformation are carried out using the DLR-TAU deformation tool which is based on radial basis functions [74]. All surface points of the aerodynamic mesh of the blade tip are moved in a rigid body motion. The instantaneous flow fields at $\alpha_{inst} = 16.08°$ ↗, which are computed with rotating sidewalls and with grid deformation technique, are compared in Fig. 3.18. The differences in the pressure distribution c_p and in the streamlines are so small that the simulation configuration with the rotating grid seems accurate enough to investigate the flow phenomena of the pitching blade tip. Comparing the F_Z-peak of one period, the difference is $\Delta F_{Z,peak} = 12$ N
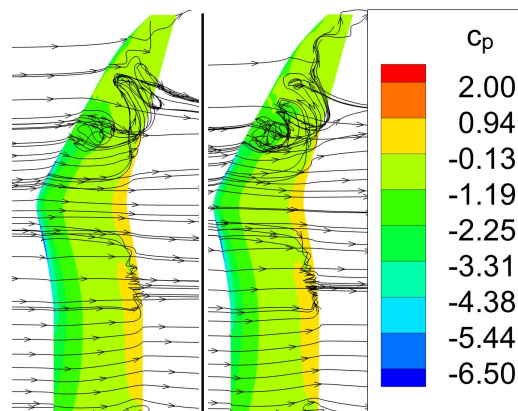

Figure 3.18: **LC-DS2**$_{pre}$ **at** $\alpha_{inst} = 16.08°$ ↗**; Grid deformation (left) vs. rotating grid (right)**

which is negligible for structural design criteria. The tip vortex merges with the dynamic stall vortex of the backward swept part. A smaller inboard separation occurs at $r \approx 250$ mm at the trailing edge. Inner and outer vortices pass the trailing edge at different angles of attack. Therefore, no single pitching moment peak appears in Fig. 3.17. There are two regions of attached flow: one at the kink and one between the corner stall at the root and the desired separation region at r ≈ 250 mm.

3.5.2 Finite Element Strength Analysis

The strength analysis procedure is presented for the load case LC-DS2$_{pre}$ shown in Fig. 3.17. The aerodynamic forces are selected from the unsteady CFD-simulation at the angle of attack where the highest lift, $F_Z = 1322$ N, occurs. The loads acting on the CFD-nodes $\mathbf{f}_a$ are interpolated to the FE-nodes $\mathbf{f}_s$.

$$\mathbf{f}_s = \mathbf{H}^T \mathbf{f}_a \tag{3.1}$$

The transposed coupling matrix $\mathbf{H}^T$ is generated by using a radial basis function approach as presented in Neumann et al. [75]. A static analysis is performed with the interpolated loads in ANSYS. The almost pure bending deformation for the FE-modeling approach V2 is shown in Fig. (3.19). The deformation in z-direction reaches its maximum $u_z = 18$ mm at the trailing edge of the tip. That indicates a light negative elastic twist at the tip.
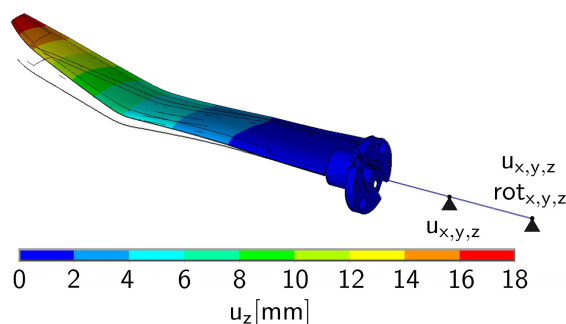

Figure 3.19: **Elastic deformation of LC-DS2$_{pre}$ for statically applied loads; $F_Z = 1322$ N**

In the next step, the forced pitching motion is simulated by means of a harmonic analysis. The deformation in z-direction of the real part $\hat{\mathbf{u}}_{a,Re}$ and the deformation of the imaginary part $\hat{\mathbf{u}}_{a,Im}$ of Equation (2.13) are shown in Fig. 3.20. Only the more sophisticated modeling approach V2 is depicted since the difference to the approach V1 is negligible.

Thanks to lightweight construction the moments of inertia are small which leads to very small deflections due to the harmonic motion. The real part shows the blade tip at time $t = 0$, where the rotational acceleration is at its maximum. The elastic deformation is obtained by subtracting the rigid motion from the overall deformation. The maximum elastic deformation $u_z = 0.1$ mm is small compared to the deformation due to the statically applied loads.
The imaginary part shows the blade tip at time $t = T/4$. The elastic deformation in the z-direction $u_z = 0.018$ mm shows that the phase difference should be generally taken into account

$f = 6.86[\text{Hz}]$, $\alpha_{\pm} = 8[^{\circ}]$

REAL

$u_{z,\text{elas}} = 0.1\text{mm}$

$-26.1 \qquad -13.0 \qquad -1.9 \qquad 10.2$

$u_z[\text{mm}]$

IMAGINARY

$0.0 \qquad 0.006 \qquad 0.012 \qquad 0.018$

$u_z[\text{mm}]$
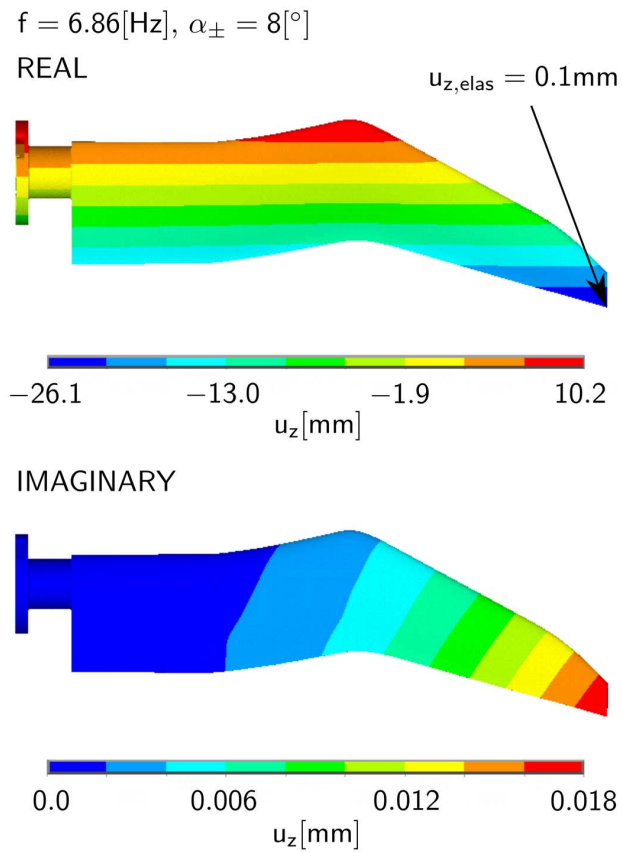
Figure 3.20: **Harmonic motion and elastic deformation due to inertia forces (V2)**

for high frequencies and amplitudes. For the presented case, the real part is superimposed on the static solution only which is a conservative approach for small phase differences.
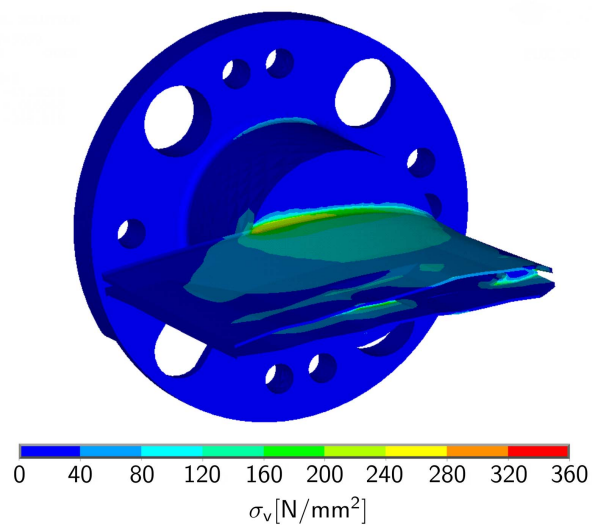
$0 \quad 40 \quad 80 \quad 120 \quad 160 \quad 200 \quad 240 \quad 280 \quad 320 \quad 360$

$\sigma_v[\text{N/mm}^2]$

Figure 3.21: **Von Mises stress in the steel shaft of the FE-model V2**

The stresses in laminate, bonding and shaft are presented for the superposed load case in the following. They are presented for the final modeling approach V2 only, except for the bonding where the results of both approaches are compared. The highest von-Mises stresses occur at the root section (Fig. 3.21) of the steel shaft. Assuming a yield point of $R_{p0.2} = 720$ MPa for the 42CrMo4 steel shaft, the factor of safety is $FoS = 2$.
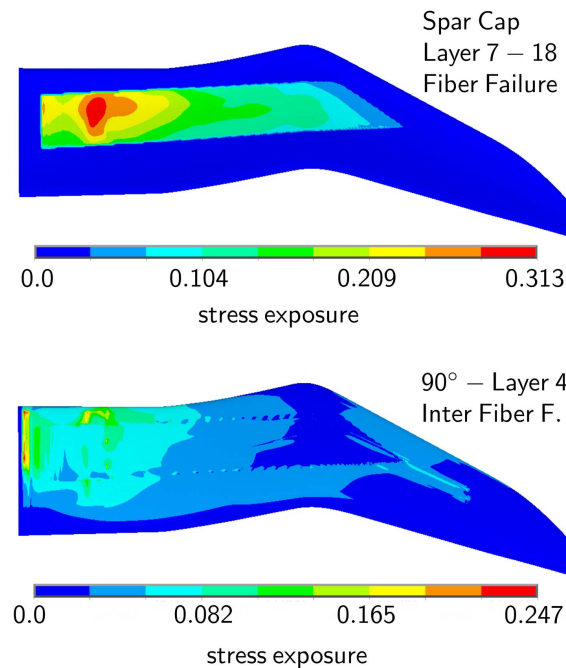

Figure 3.22: **Strength analysis with the FE-model V2 for the load case LC-DS2**$_{pre}$ **(Fig. 3.17)**

The Puck criterion [72] identifies fiber failure (FF) and inter-fiber failure (IFF) in the unidirectional lamina. It has been used to determine the stress exposure of each unidirectional ply of the laminate. The four Puck inclination parameters and the out-of plane properties of the M46J lamina have been estimated with data from similar materials. The other material properties have been determined experimentally by the Institute of Composite Structures and Adaptive Systems. In Fig. 3.22, the fiber failure stress exposure is depicted for the 2.5° - spar cap - layers in the upper shell. The highest stress peaks are detected at the spanwise end of the steel shaft where the loads are transferred from the spar cap to the shaft. However, the factor of safety is $FoS > 3$. The elevated stress level shows that the minimization of the stiffness discontinuities is important. Without the tapered channel at the spanwise end of the steel shaft the stress exposure would be higher.

The stress exposure according to the inter-fiber failure (IFF) criterion of Puck is shown for the 90°-layer of the lower half shell on the bottom of Fig. 3.22. The upward bending causes tensional loads in the lower half shell. Since the IFF criterion is sensitive to tensional loads, the stress exposure is highest in the 90°-layer of the lower half shell. It increases towards the root where the bending moment reaches its maximum. Small discontinuities can be seen at the free corners of the spar cap reinforced shells. The effect is enforced by the neglected chordwise tapering in the FE model. The stresses in all layers show peaks at the root section since global forces and bending moments reach their maximum. Furthermore, the material thickening of

the shaft leads to a strong change in stiffness. Spanwise tapering at the root section in order to prevent edge delamination is included in the FE model.
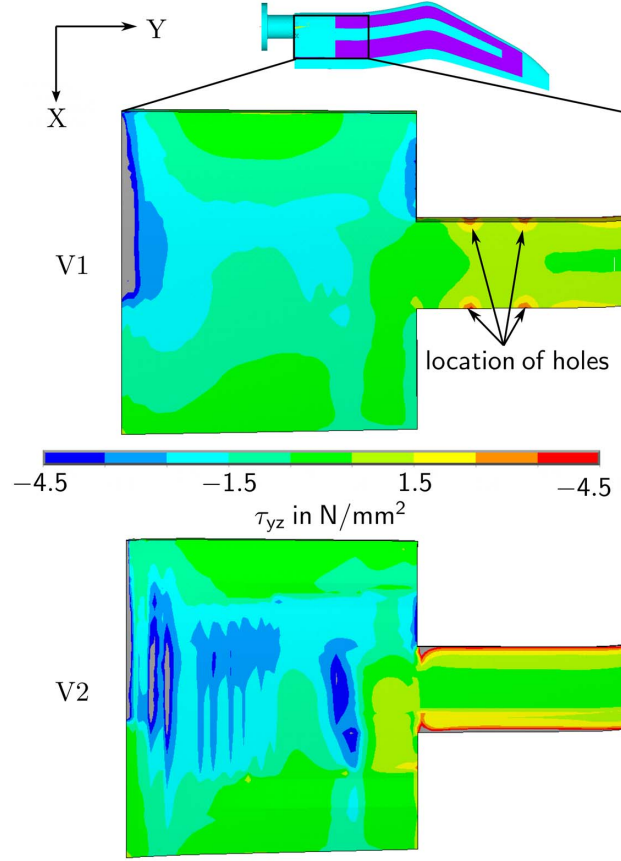

Figure 3.23: **Shear stress τ_{yz} in bonding on upper shaft and spar**

The resulting spanwise shear stress distributions τ_{yz} of the bonding are shown in Fig. 3.23. The first modeling approach V1 with the too thick adhesive layer is compared to the final modeling approach V2. Considerable stress peaks occur at the spanwise end of the shaft for both modeling approaches. In order to reduce these stress peaks, a channel with higher and more homogeneous tapering is introduced in V2. Furthermore, the tapering of the spar overlap is included and preliminary holes for cable feedthrough in the spar are eliminated. However, the realistic modeling of the adhesive layer leads to stronger stiffness discontinuities and consequently to higher stresses for the approach V2. The mean shear stress in the bonding on the upper side of the shaft is often calculated by

$$\tau_{yz,mean} = \frac{F}{A} = \frac{18873\,\text{N}}{15000\,\text{mm}^2} = 1.26\,\text{MPa} \tag{3.2}$$

where F are the internal section forces in spanwise direction summed over the nodes of the upper shells and A is the upper surface area of the steel shaft. The maximum mean shear stress $\tau_{yz,mean,max} = 7$ MPa divided by the mean shear stress of the shaft yields a factor of safety of $FoS = 5.6$. However, due to the inhomogeneous stress distributions shown in Fig. 3.23 a $FoS = 2.0$ seems more realistic.

4 Static Polars and Flow Phenomena at High Static Angles of Attack

More than 1000 measurement points were taken over the course of two wind tunnel experiments. During the first campaign the deformation was measured on the upper side of the model. In the second measurement campaign, the surface pressure of the upper side was investigated by unsteady pressure sensitive paint (iPSP) and the deformation was measured on the lower side of the model. Static polars are compared to computations for different Mach and Reynolds numbers in the following. Local flow phenomena are shown for static measurement points at high angles of attack. Reproducibility tests are used to evaluate the accuracy of the measurement equipment and the wind tunnel itself. The most relevant test cases with regard to dynamic stall are presented in the subsequent chapter.

The global lift, drag and moment determined by the piezoelectric balance are shown in Figs. 4.1-4.3 for several static polars. The standard deviation of the experimental data is indicated by the error bars.

In general, the CFD-computations with the TAU-code show a good agreement with the experimental results even though neither a laminar-turbulent transition model nor the elastic deformation (up to 20 mm bending deformation at the tip) has been taken into account.

Global Lift Polars

For the presented polars, the lift increases up to the maximum angle of attack of $\alpha = 15°$ for $Ma = 0.3$ and $Re = 0.72 \cdot 10^6$. The data of the piezoelectric balance is only available up to $\alpha = 13.5°$ where the lift curve is still nearly linear and the standard deviation is only slightly increased. The computed data shows some deviations at $11° \leq \alpha \leq 12°$, but stall occurs at $\alpha > 15°$ only. The maximum lift coefficient is $C_{L,NUM,max} = 1.17$.
At $Ma = 0.5$ and $Re = 0.72 \cdot 10^6$, the experiment and the computations indicate stall for $\alpha > 12.5°$. One can deduce highly unsteady, separated flow from the increased standard deviation at this point. The maximum lift coefficient, $C_{L,EXP,max} = 1.07$, is slightly underpredicted by the computations. It is remarkable, that the PSP-coated model shows a decreased slope of the C_L-curve and a reduced maximum lift coefficient of $C_{L,EXP-PSP,max} = 1.01$. The decreased standard deviation at $\alpha = 13°$ might indicate a slightly increased stall angle. The slope of the linear part of the curves is increased for the higher Mach number, but it is approximately the same for

the different Reynolds numbers at $Ma = 0.5$. Due to the high forces and the strong separation, it was not possible to measure at angles of attack higher than $\alpha = 12.5°$ for $Ma = 0.5$ and $Re = 1.2 \cdot 10^6$. At $\alpha = 12.5°$ the standard deviation is significantly smaller than for the lower Reynolds number. However, in the computations the lift reaches its maximum at $\alpha = 12.5°$ for both Reynolds numbers. The difference at this point is less than $\Delta C_{L,NUM} = 0.005$.

Global Pitching Moment Polars

The slope of the pitching moment is very similar for all curves. There is a nearly linear decrease till $\alpha = 12°$ for $Ma = 0.3$ and $\alpha = 11°$ for $Ma = 0.5$. The minimum moment is $C_{M,EXP,min} = -0.09$ at $\alpha = 13.5°$ for $Ma = 0.3$. It is $C_{M,EXP,min} = -0.07$ at $\alpha = 11.5°$ for $Ma = 0.5$ for the same Reynolds number $Re = 0.72 \cdot 10^6$. The PSP-coated model has a less negative C_M-slope but shows a strong decrease at $\alpha > 12°$ where the pitching moment of the uncoated model increases. Its minimum $C_{M,EXP,min} = -0.08$ is at $\alpha = 13°$. The minimum is $C_{M,bal} = -0.07$ at $\alpha = 12.5°$ for the higher Reynolds number $Re = 1.2 \cdot 10^6$. The computations yield nearly the same values as for the uncoated model. Only at $Ma = 0.5$ and $Re = 1.2 \cdot 10^6$ the experimental pitching moment falls below the computed pitching moment at $\alpha > 12°$.

Global Drag Polars

The drag is increased for higher Mach numbers but shows hardly any difference between the two different Reynolds numbers. For all test cases the drag shows a nonlinear behavior over the whole range and increases significantly for higher angles of attack. Similar to the lift, the standard deviation increases significantly at $\alpha = 12.5°$ at $Ma = 0.5$ and $Re = 0.72 \cdot 10^6$. At this angle of attack, the standard deviation is significantly lower for the higher Reynolds number. The computations show a good agreement up to $\alpha = 5°$. The experimental drag is higher than the numerical results at higher angles of attack.
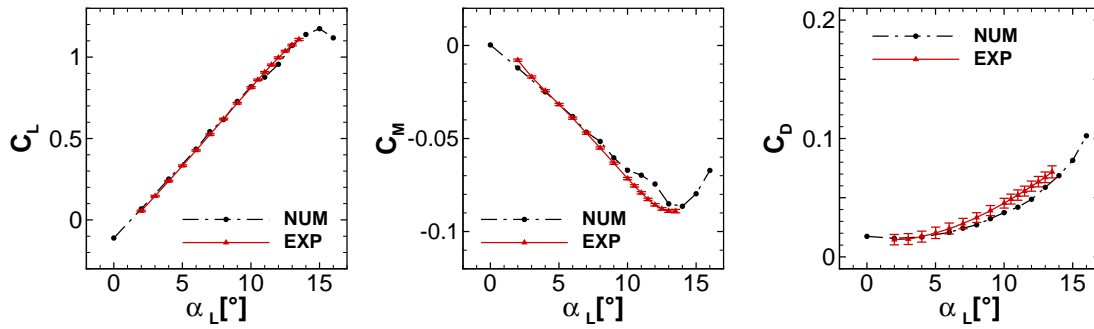
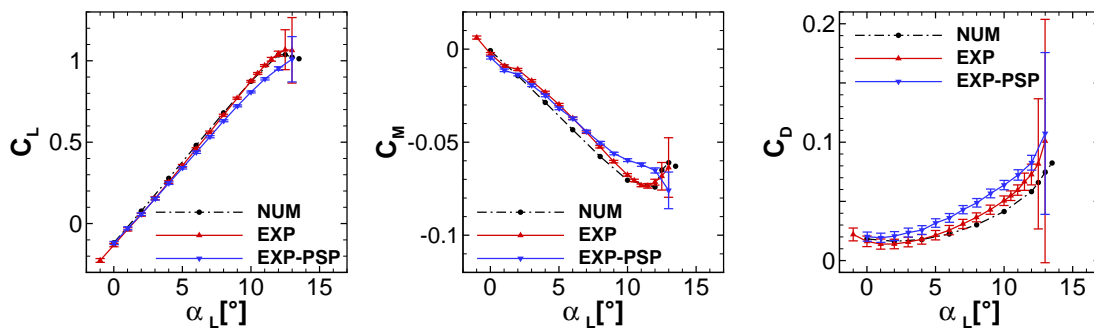Figure 4.1: **Static polar at** $Ma = 0.3$ **and** $Re = 720.000$

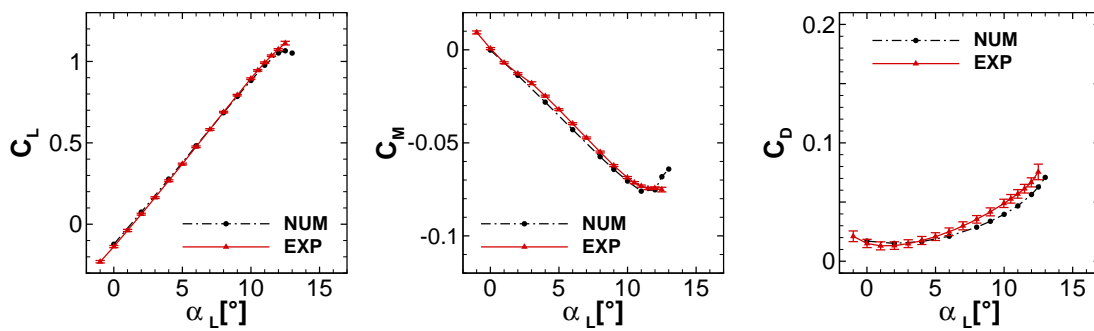Figure 4.2: **Static polar at** $Ma = 0.5$ **and** $Re = 720.000$

Figure 4.3: **Static polar at** $Ma = 0.5$ **and** $Re = 1.200.000$

Local Flow Phenomena and c_p-Distributions at High Static Angles of Attack

In the following, local flow phenomena at high angles of attack are presented by means of CFD simulations, discrete pressure measurements and infrared measurements.

In Fig. 4.4, the c_p-distributions at sections S2, S4 and S6 are presented for the uncoated model at $Ma = 0.5$, $Re = 1.2 \cdot 10^6$ and $\alpha = 12.5°$. The global angle of attack is measured with respect to the maximum twist which is at the forward-backward kink (section S4). Considering the twist distribution, which is depicted on the bottom of Fig. 4.5, the geometric angle of attack is reduced to $\alpha = 8.9°$ at section S2 and to $\alpha = 11.4°$ at section S6. Therefore, it is remarkable that the suction peak is lowest at S4. The laminar turbulent-transition is located between $0.11 < x/c < 0.15$ where a light drop can be seen in the c_p-distribution. At section S6, the plateau of the high suction peak might indicate a laminar separation bubble ([36],[76]) followed by a shock. Due to the strong fluctuations of the laminar separation bubble there is a slight discrepancy between the two experimental c_p-distributions recorded on two different days. The agreement between the other experimental c_p-data (MR580 and MR1160) shows the excellent reproducibility of the measurements. The decreased suction level at the leading edge of section S4 can be explained by the double-swept planform which leads to strong crossflow velocities, shown in Fig. 4.5.
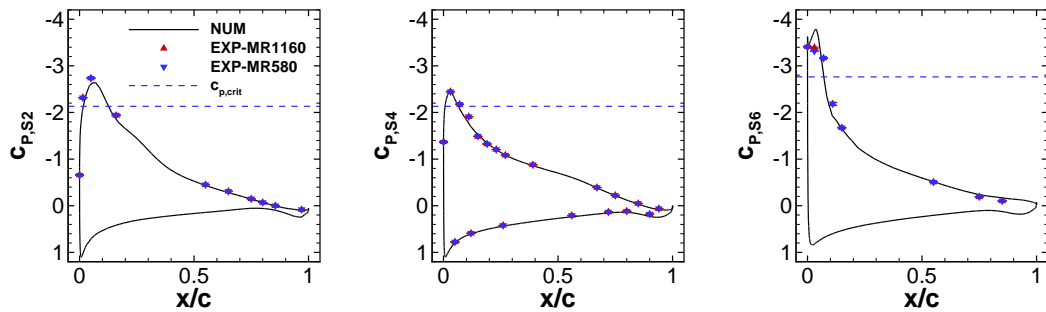

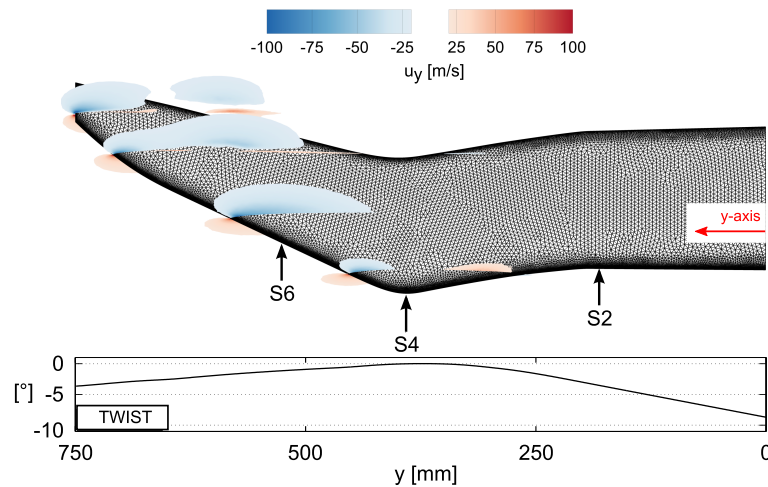Figure 4.4: **Sectional c_p-distributions at $Ma = 0.5$, $Re = 1.2 \cdot 10^6$ and $\alpha = 12.5°$**

Figure 4.5: **Computed spanwise velocities at $Ma = 0.5$, $Re = 1.2 \cdot 10^6$ and $\alpha = 12.5°$**

The spanwise velocity components are directed inboard at the leading edge of the backward swept part and directed outboard at the leading edge of the forward swept part. Thus, the spanwise velocities show in the opposite direction at the kink, which leads to a less accelerated flow and a reduced c_p at the leading edge. At the trailing edge, the spanwise velocities change their sign. They point in outboard direction at the backward swept part and in inboard direction at the forward swept part. This leads to a favorable pressure gradient for attached flow at the kink.
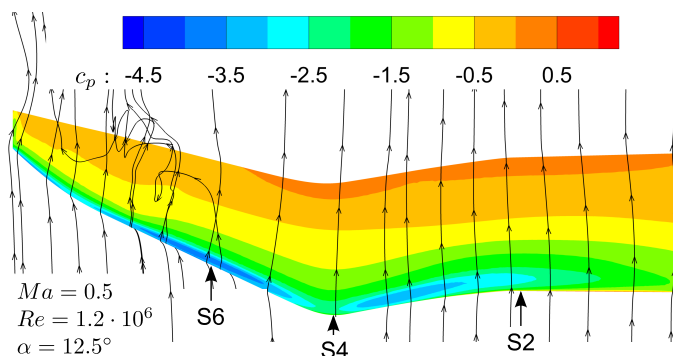

Figure 4.6: **Upper surface c_p-distribution and streamtraces at $Ma = 0.5$, $Re = 1.2 \cdot 10^6$ and $\alpha = 12.5°$**

In Fig. 4.6, the streamtraces and the c_p-distribution on the upper surface prove the statements above. Flow separation occurs outboard of section S6. A clearly reduced suction peak can be seen at the beginning of the parabolic part of the blade tip.
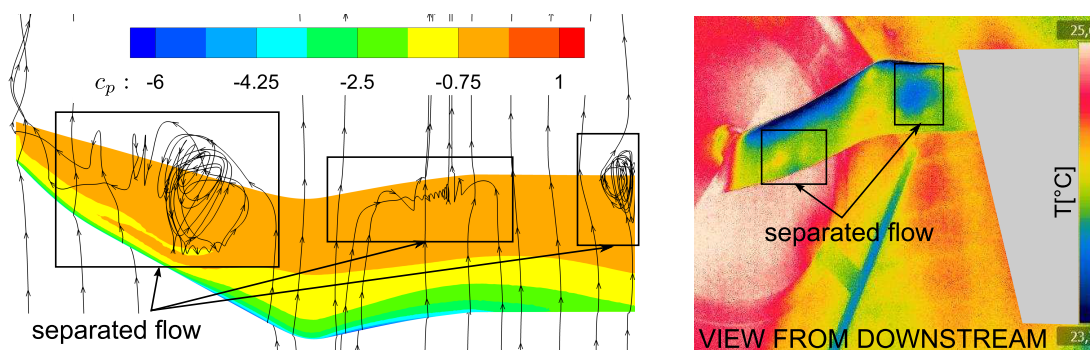
Figure 4.7: **Computations and infrared image at $Ma = 0.3$, $Re = 0.72 \cdot 10^6$, $\alpha = 16°$**

As one can see in Fig. 4.7, the infrared measurements at $\alpha = 16°$ show the same separated flow regions as the computations. Inboard and outboard of the kink, two regions of strong flow separation can be detected. Only the corner stall at the root cannot be completely confirmed by the infrared measurements due to the strong reflections of the wind tunnel wall. It is most likely decreased by an inboard vortex caused by the small gap of 1.5 mm between the wall and the model [77]. The greyed-out data is ambiguous due to reflections of the window frame where the camera is mounted. As shown in Fig. 4.8, stronger flow separation is detected at the same locations at $\alpha = 17.5°$. The separated flow regions have significantly spread.

Figure 4.8: **Infrared image at** $Ma = 0.3$**,** $Re = 0.72 \cdot 10^6$ **and** $\alpha = 17.5°$

5 Dynamic Stall at the Double-Swept Blade Tip

In this chapter, experimental dynamic test cases with no stall, light stall and deep stall are presented. All the test cases described in this thesis are listed in Tab. 5.1. The influence of mean

Table 5.1: **Dynamic test cases investigated in this thesis**

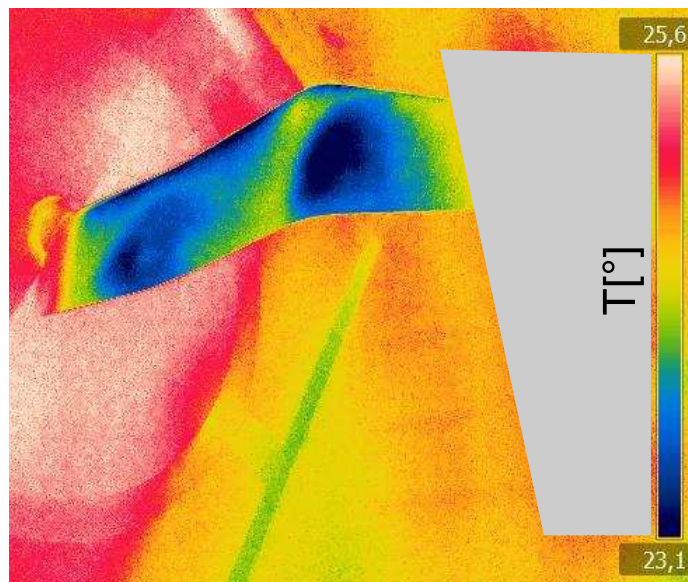| Test Case	Ma	$Re/10^6$	$\alpha[°]$	$f[Hz]$	k	PSP coating
LC-WO1	-	-	0.22 ± 3	6.6	-	no
LC-DS0	0.5	1.2	8 ± 3	6.6	0.039	no
LC-DS1	0.5	1.2	8 ± 5	6.6	0.039	no
LC-DS2	0.5	0.72	8 ± 5	6.6	0.039	no
LC-DS3	0.5	0.72	10 ± 5	6.6	0.039	no
LC-DS4	0.5	0.72	10 ± 5	3.3	0.020	no
LC-DS5	0.5	0.72	10 ± 5	9.9	0.059	no
LC-DS6	0.5	0.72	8 ± 5	6.6	0.039	yes
LC-DS7	0.5	0.72	8 ± 4	6.6	0.039	yes
LC-DS8	0.5	0.72	8 ± 6	6.6	0.039	yes
LC-DS9	0.4	0.72	8 ± 6	6.6	0.039	yes

angle, oscillation amplitude, Mach number, Reynolds number and deformation are investigated. Data of numerical simulations are evaluated and support the experimental results by means of flow field plots. The most important of the numerous unsteady measurement points are presented in this work. A preselection of test cases is done by means of the piezoelectric balance data. Preliminary wind-off measurements are used to evaluate the forced motion and inertial effects on the balance data.

5.1 Wind-Off Measurements

Wind-off measurements are done in order to evaluate the influence of the inertial forces on the global balance data. The acceleration and the inertial forces caused by the dynamic motion at a discrete frequency and amplitude can be easily compared to analytical calculations. The pitching

angle is defined by

$$\varphi = A \cdot \sin(\omega t) = A \cdot \sin(2\pi ft) \tag{5.1}$$

with the first and second derivatives being:

$$\dot{\varphi} = A \cdot \omega \cdot \cos(\omega t) = A \cdot 2\pi f \cdot \cos(2\pi ft) \tag{5.2}$$

$$\ddot{\varphi} = -A \cdot \omega^2 \cdot \sin(\omega t) = -A \cdot 4 \cdot \pi^2 f^2 \sin(2\pi ft) \tag{5.3}$$

The vector from the rotation point at the wind tunnel wall to the accelerometer is

$$\vec{r} = \begin{pmatrix} \cos\varphi \cdot r \\ y_{acc} \\ \sin\varphi \cdot r \end{pmatrix} \tag{5.4}$$

with the second derivative being:

$$\ddot{\vec{r}} = r \begin{pmatrix} -\cos\varphi \cdot \dot{\varphi}^2 - \sin\varphi \cdot \ddot{\varphi} \\ 0 \\ -\sin\varphi \cdot \dot{\varphi}^2 + \cos\varphi \cdot \ddot{\varphi} \end{pmatrix} \tag{5.5}$$

The moment caused by the dynamic motion is the moment of inertia I_{yy} multiplied by the angular acceleration $\ddot{\varphi}$:

$$M_y = I_{yy} \cdot \ddot{\varphi} \tag{5.6}$$

In Fig. 5.1 a wind-off measurement point at $\alpha_{mean} = 0.22°$, $\alpha_{osc} = 3°$ and $f = 6.6$ Hz is shown.
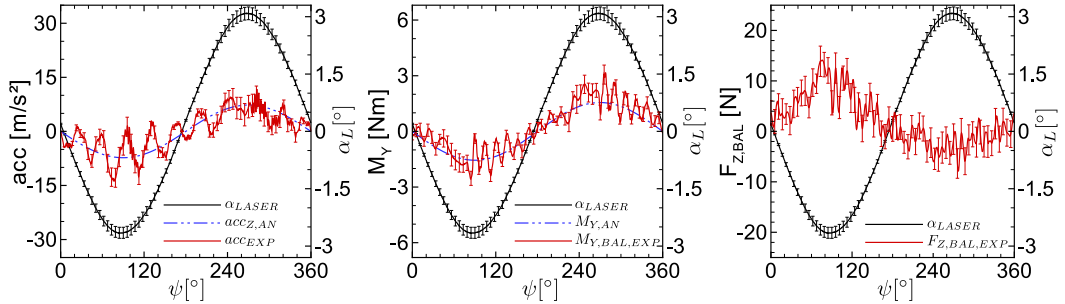

Figure 5.1: **Wind-off measurement (LC-WO1) at** $f = 6.6$ **Hz and** $\alpha = 0.22° \pm 3°$

The data is phase-averaged, the standard deviations to the according phase-averaged values are indicated by the error bars. The angle of attack is shown in each diagram of Fig. 5.1 for convenience. In the left diagram the z-component of the acceleration vector in Eq. 5.5 is compared to the data of the accelerometer positioned in z-direction of the blade. This is an acceptable approximation since only small angles are investigated. In the middle diagram the analytical pitching moment calculated in Eq. 5.6 is compared to the experimental pitching moment measured by the piezoelectric balance. In the right diagram the inertial force in z-direction of the wind tunnel is shown. The accelerometer and the balance data show strong higher harmonic oscillations and strong standard deviations. The (1/rev) motion is clearly seen only for $\mathbf{acc}_{EXP}$ and $\mathbf{F}_{Z,BAL}$. The balance data of the pitching moment $\mathbf{M}_{Y,BAL}$ show a good global agreement to the analytical solution but the oscillations are not noticeable. The deviation of α indicates a non-perfect input signal. A non-perfect sinusoidal motion usually generates higher harmonics

of the (1/rev)-motion. In Fig. 5.2, the spectral content of the α-signal, the moment and the force in z-direction are shown. The data is transformed into the frequency domain using Fast Fourier Transform (FFT). The transformation is done on the entire signal. The signal is neither averaged nor filtered. Every spectrum has a small DC-part since the signals are not symmetric to zero. The maximum peak of the α-signal is the excitation frequency. The higher harmonic parts of the α-signal are reduced by approximately two orders of magnitude. However, even small amplitudes are sufficient to cause relatively high moments and forces. Thus, considering the moment $M_{y,bal}$, a broad spectral content for nearly all harmonics can be observed. The highest peaks occur at the eigenfrequencies of the model which are labeled in Fig. 5.2. The bending mode-shapes are emphasized in the forces in z-direction, the lag mode shape (2nd) in the moment. One can deduce, that it is impossible to thoroughly filter the inertial forces from the balance data in wind-on measurements.
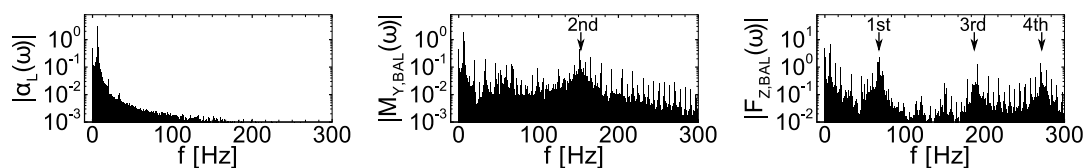

Figure 5.2: **Frequency spectrum of LC-WO1 with labeled eigenfrequencies of the model**

5.2 Light Dynamic Stall

The light dynamic stall case (LC-DS1) investigated in detail is at $Ma = 0.5$, $Re = 1.2 \cdot 10^6$, $\alpha = 8° \pm 5°$, and $f = 6.6$ Hz ($k = 0.039$). At this test case, the limiting loads of the structure occur due to the high stagnation pressure and strong oscillations around the maximum angle of attack. Computations with a rigid structure are compared to the experimental results. At first, the global forces and moments are presented. The sectional loads are shown before the local flow phenomena are interpreted. At the end, detailed insights in the separated flow at selected high angles of attack are given.

Global Lift, Moment and Drag

The data of the piezoelectric balance give insights in the dynamic behavior of the global lift, moment and drag of the blade tip. Furthermore, it indicates if significant separation occurs on the model. Due to the drawbacks concerning the high sensitivity to inertial forces, the pitching moment and the drag show high oscillations. Still, comparing LC-DS1 to the test case LC-DS0, which has a lower amplitude, one can see in Fig. 5.3 that the forces and moments show a rather smooth distribution for LC-DS0. The nearly linear lift curve has no hysteresis. Except for the lower oscillations, the moment and drag also show a nearly linear behavior. In contrast, LC-DS1 shows a light drop in the lift right behind the maximum angle of attack $\alpha_{max} = 13°$. Due to the high oscillations in the pitching moment it is not possible to determine which peaks are due

to the structural dynamics and which are due to the aerodynamics. However, the total pitching moment coefficient is very small and does not drop below $C_{M,bal} = -0.1$ in the entire cycle. This corresponds to a pitching moment of $M_{y,bal} \approx -20$ Nm. The range of the oscillation amplitudes is similar to the range in the wind-off measurements, shown in Fig. 5.2. A significant increase and strong peaks can be seen in the drag coefficient close to the maximum angle of attack. As mentioned in Section 1.2, this is a typical characteristic of dynamic stall. It is interesting to note, that in the dynamic test case, separation sets in only 0.5 degrees later than in the static stall polar, shown in Fig. 4.3. In Fig. 5.4 the phase averaged balance data is compared to the fifth cycle
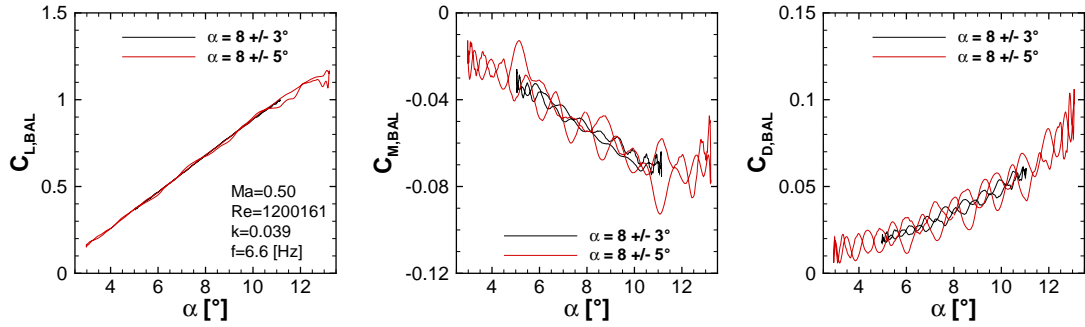

Figure 5.3: **LC-DS0 ($\alpha = 8 \pm 3$) vs LC-DS1 ($\alpha = 8 \pm 5$), experimental balance data**
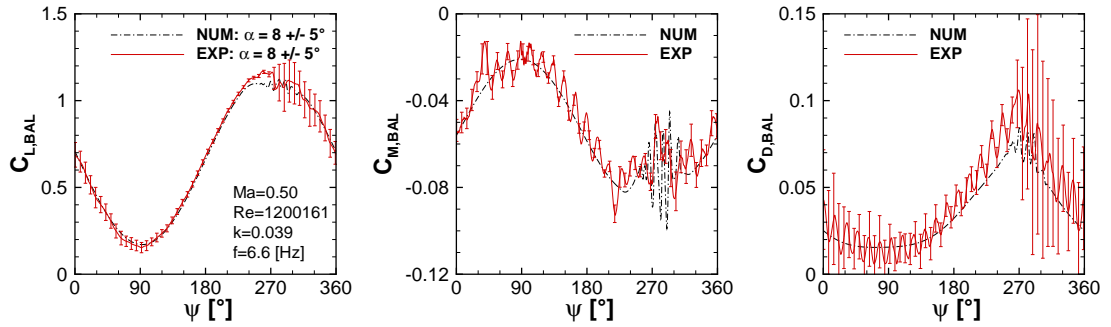
Figure 5.4: $Ma = 0.5$, $Re = 1.2 \cdot 10^6$, $\alpha = 8 \pm 5$, **global balance vs numerical data**

of the according numerical URANS computation with rigid contour. The data is plotted over the phase angle where $\alpha_{max} = 13°$ is at $\psi = 270°$. The general behavior of global lift, moment and drag is in good agreement between the experimental and the numerical data. The error bars indicate the experimental standard deviation from cycle to cycle. Right behind the drop in the lift the deviation increases which indicates separation. Besides the highest oscillations, the strongest gradients in the experimental pitching moment occur around $\psi = 270°$ at the highest angle of attack. The same counts for the numerical global pitching moment. The standard deviations in the regions of detached flow are highest for the drag. The high standard deviations of the experimental coefficients result from phase-shifted oscillations, as will be shown later.

Sectional Lift, Moment and Drag

In Fig. 5.5 and 5.6 the integrated sectional C_l- and C_m-distribution are shown for the sections S2-S5. In Fig. 5.7 and 5.8 the same curves are presented for the outboard sections S6-S8. The experimental results of one single, non-averaged period "EXP-SGL-PER" and the computed curve "NUM-SENSOR" are integral values over the discrete pressure tap positions. If these curves match, one can expect that the fully integrated computed curve "NUM-FULL" reflects well the reality. The pitching moment coefficients are calculated with respect to the local quarter-chord point.

The lift coefficients $C_{l,EXP}$ and $C_{l,NUM-SENS}$ show a good agreement for the sections S2-S5, shown in Fig. 5.5. The level of the lift coefficient of the fully integrated numerical solution is about $\Delta C_l = 0.1$ higher at the maximum angle of attack at S4. This is due to the suction peak which is not properly resolved by the limited number of pressure transducers. This discrepancy between the fully integrated lift coefficient and the reduced integrated value becomes more evident at the other sections with less pressure transducers. Considering the fully integrated numerical solutions, it is remarkable that the maximum lift increases from section S4 to S5 even though the local geometric angle of attack decreases (see Fig. 3.1). In section S5, small oscillations around the maximum angle of attack indicate the onset of separation. The experimental lift coefficient shows two drops at $\psi \approx 201°$ and at $\psi \approx 345°$. They are caused by the laminar-turbulent transition and the small number of pressure transducers. In section S2, a stronger drop at $\psi \approx 270°$ occurs for the same physical reasons. These phenomena are discussed later on in this thesis. Due to the fine resolution on the upper side of section S4 the drops do not occur in the integrated $C_{l,S4}$-coefficient. The fully turbulent URANS computation cannot resolve the phenomena since laminar-turbulent transition is not taken into account.
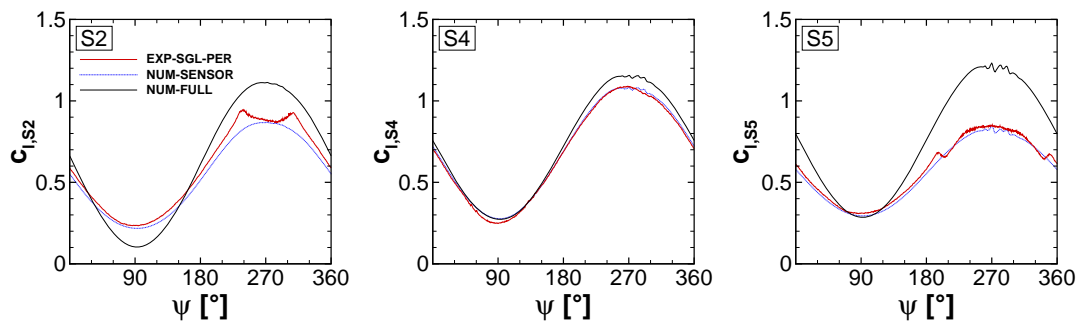
Figure 5.5: **Sectional lift coefficients for** $Ma = 0.5$, $Re = 1.2 \cdot 10^6$, $\alpha = 8° \pm 5°$

As shown in Fig. 5.6, the agreement between $C_{m,EXP}$ and $C_{m,NUM-SENS}$ is also very well. As for the lift, the discrepancy between the reduced numerical moment coefficient $C_{m,NUM-SENS}$ and the fully integrated solution $C_{m,NUM-FULL}$ is smallest for section S4 where many pressure transducers are located. The fully integrated numerical pitching moment does not fall below $C_m = -0.06$ for any section. The oscillations at $\psi \approx 270°$ for S4 and S5 do not occur in the experimental data. For S5, the discernible peak indicates flow separation in the computation around the maximum angle of attack.

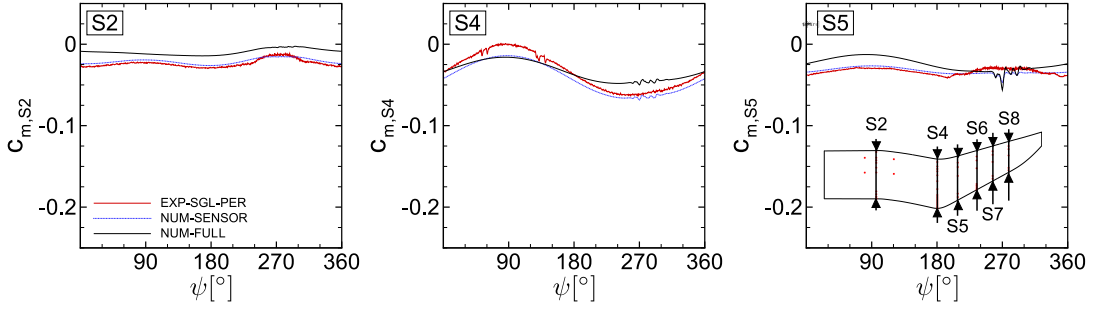Figure 5.6: **Sectional moment coefficients for** $Ma = 0.5, Re = 1.2 \cdot 10^6, \alpha = 8° \pm 5°$
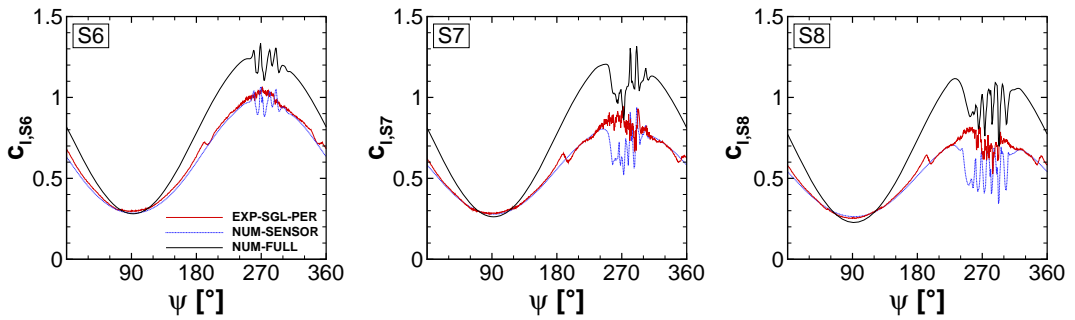
Figure 5.7: **Sectional lift coefficients for** $Ma = 0.5, Re = 1.2 \cdot 10^6, \alpha = 8° \pm 5°$
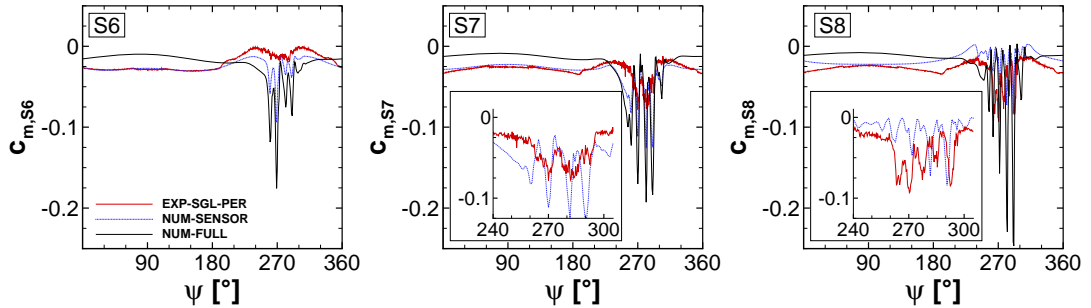
Figure 5.8: **Sectional moment coefficients for** $Ma = 0.5, Re = 1.2 \cdot 10^6, \alpha = 8° \pm 5°$

Stronger separated flow can be deduced from the lift and moment coefficients of the outboard sections S6-S8, shown in Fig. 5.7 and 5.8. All C_l-coefficients, except the $C_{l,S6,EXP}$-coefficient, show discernible drops followed by strong oscillations which increase from S7 to S8. The computations predict earlier and stronger drops for all lift coefficients and show higher oscillations than the experimental data. It is remarkable that the level of $C_{l,NUM,FULL}$ increases from S4 to S6 even though the geometric angle of attack decreases from S4 to S6. This yields for the entire cycle. At S7, two strong secondary peaks behind $\psi = 270°$ indicate strong vortical structures introducing additional suction on the upper side of the blade tip. At S8 the tip vortex leads to a reduction of the local angle of attack and consequently of the lift. The transition drops occur at $\psi \approx 180°$ and $\psi \approx 360°$ in all three experimental lift distributions.

Separated flow is indicated in all C_m-coefficients of sections S6-S8: drops occur close to the

highest angle of attack and are followed by oscillations. Similar to the lift, these oscillations increase from S6 to S8 in the experimental and numerical data. The computations seem to predict stronger flow separation for the sections S6 and S7. At section S8, the oscillations are qualitatively well captured by the computations but slightly phase-shifted. There is a strong discrepancy between the fully integrated solution and the reduced integration method due to the limited number of transducers. At section S8, the difference between the full and reduced moment is $\Delta C_m = 0.17$ at $\psi = 292°$.

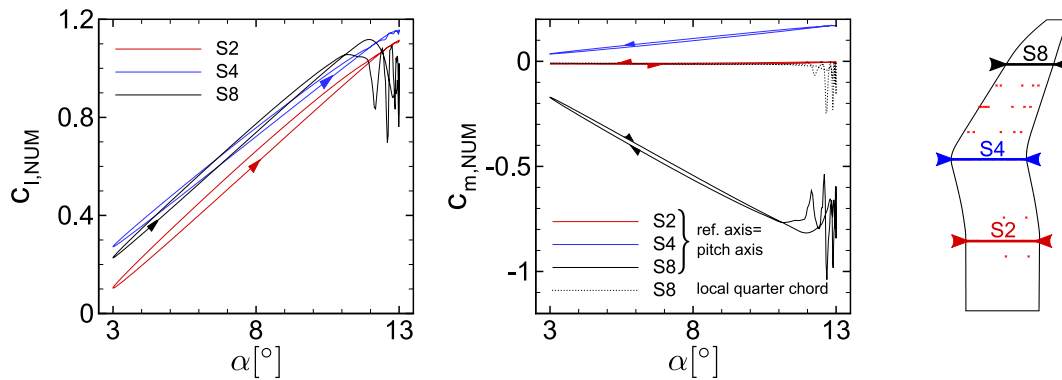Figure 5.9: **Computed sectional C_l- and C_m-distributions - fully integrated**

In Fig. 5.9, the fully integrated $C_{l,NUM}$- and $C_{m,NUM}$-distributions are shown for the sections S2, S4 and S8. The coefficients are plotted along the angle of attack. The moment coefficients are now calculated with respect to the pitching axis. Since S4 is located in front of the root chord, $C_{m,S4}$ becomes positive. The moment coefficient of section S8 is strongly decreased due to its backward shifted position. The hysteresis of the sections S2 and S4 are small due to non-separated flow in these regions. In the separated flow region S8, strong hysteresis can be seen in the lift and moment coefficient. Compared to the moment coefficient calculated with respect to the local quarter chord, one can state that the moment hysteresis has increased due to the backward position. The peaks and gradients close to the maximum angle of attack have also increased. However, comparing the results of Fig. 5.9 with the small global pitching moments of the balance in Fig. 5.4, one can state, that the model is extremely well-balanced around the pitching axis. The local flow phenomena which directly influence the C_l- and C_m-distributions are investigated in the following.

Local Flow Phenomena and Detailed Validation of the Computations

In Fig. 5.10 and 5.11, the pressure signals on the suction side of the six sections S2 and S4 - S8 are compared to the numerical results. The sections start at the leading edge $x/c = 0.0$ and end near the trailing edge $x/c = 1$. The distribution of pressure transducers is adapted to the two-dimensional experiments [24]. Thus, the positions of the transducers are different between S2, where the airfoil EDI-M112 is located, and S4-S8 ,where the airfoil EDI-M109 is placed. In order to show the oscillations in the experimental data, one single period is compared to the computations.
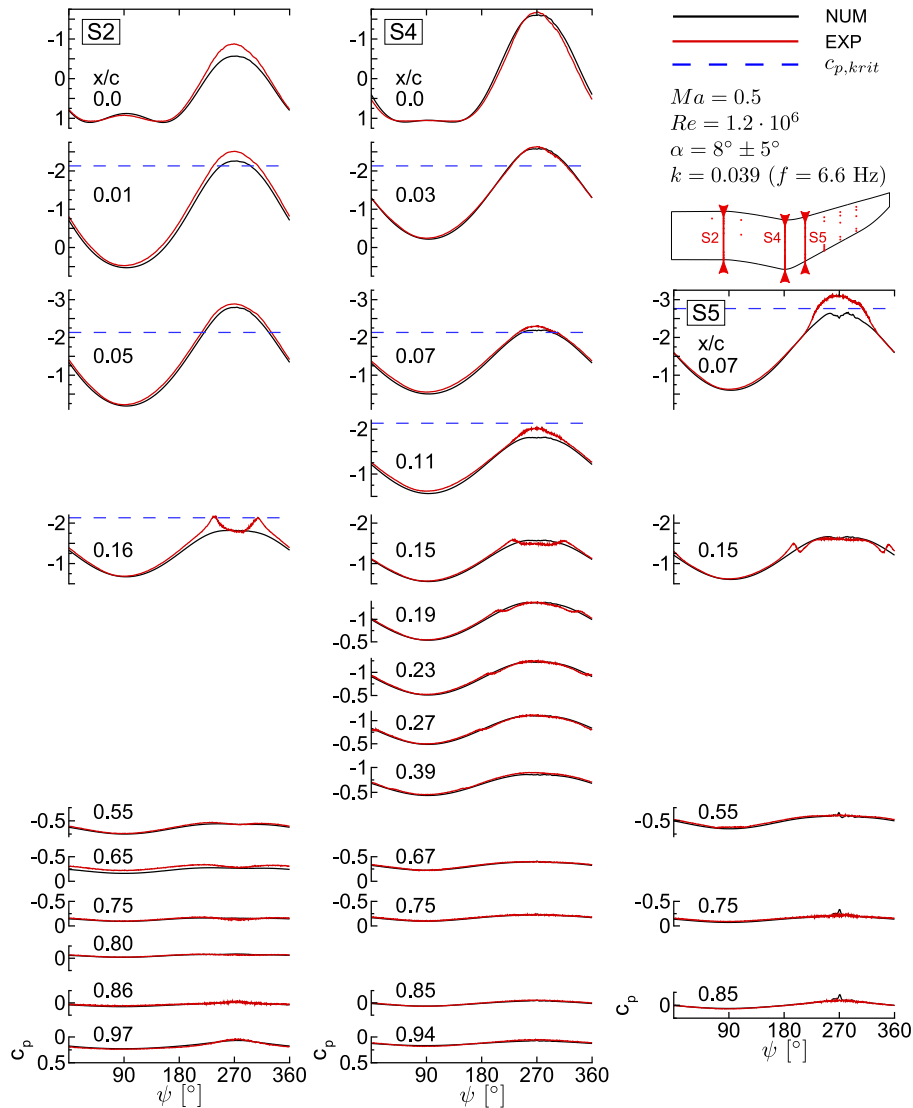
Figure 5.10: $Ma = 0.5$, $Re = 1.2 \cdot 10^6$, $\alpha = 8° \pm 5°$, **pressure data of sections 2,4,5**

There is a good agreement between the numerical and experimental data in section S2. The suction peak is slightly underpredicted at $x/c = 0.0 - 0.05$. Therefrom, one can deduce that the gap (1 mm) between wind tunnel wall and model, which is not taken into account in the simulations, does not significantly affect the flow. Otherwise, one would expect a decreased experimental lift due to the pressure compensation at the gap. The flow is attached almost over the entire cycle. Only small signs of separation at the trailing edge can be seen around the maximum angle of attack $\alpha_{max} = 13°$ ($\psi = 270°$): the reduced suction level from $x/c = 0.55 - 0.80$, the small oscillations and the nonsinusoidial, elevated suction level at $x/c = 0.97$ indicate reversed flow and trailing edge separation. The drop in the experimental c_p-curve at $x/c = 0.16$ might be due to a laminar-turbulent transition triggered by a shock. The numerical simulations cannot reproduce this behavior since transition is not taken into account.

At S4 similar, but significantly smaller drops can be seen in the experimental curves starting at $x/c = 0.39$ at $\psi \approx 148.2\circ$ ($\alpha = 5.37°$) and moving forward to $x/c = 0.15$ at $\psi \approx 231°$ ($\alpha =$

11.89°). The drops show zones where the flow velocity is suddenly reduced. They are part of the laminar-turbulent transition zone which moves forward with increasing angle of attack. The drops increase at the angle where $c_{p,crit}$ is reached in the section, as one can see at $x/c = 0.15$ at $\psi \approx 228°$. At the downstroke the transition occurs at $x/c = 0.15$ at $\psi \approx 313.9°$ ($\alpha = 11.60°$) and moves backward to $x/c = 0.39$ at $\psi \approx 35.8°$ ($\alpha = 5.08°$). The global angles of attack at which transition drops occur are listed for all sections in Tab. 5.2. Furthermore, the difference in the angles of attack at which transition occur between the upstroke and the downstroke are given. Similiar to the 2D-investigations of Richter et al. [22], the maximum of the hysteresis $\Delta\alpha = 0.77°$ is at $x/c = 0.23$. The data in S4 show no signs of flow separation. The general agreement between the numerical and experimental results is excellent.

The experimental and numerical results show stronger deviations at S5 at around $\psi = 270°$. The peaks in the numerical c_p-distribution at $x/c = 0.55 - 0.85$ indicate trailing edge separation. They cause the pitching moment peak seen in Fig. 5.6. The small oscillations in the experimental results at around $\psi \approx 270°$ might indicate the onset of separation as well. As already shown in the sectional lift and moment coefficients, a stronger separation is predicted by the computations. This confirms the tendency of the steady simulations towards flow separation at lower angles of attack in comparison to the experimental results. The elevated suction at $x/c = 0.07$ is not reproduced by the numerical simulations. The suction peak is higher than at S4, although there is a higher geometric angle of attack at S4 (see Fig. 3.1). This is caused by the double-swept planform which leads to strong crossflow velocities, as described in Chapter 4. It is remarkable that the transition drops at $x/c = 0.15$ occur at lower angles of attack then in S4, compare Table 5.2. One can conclude that the laminar-turbulent transition is located closer to the leading edge in the backward swept part.

Table 5.2: **Drops in the c_p-distribution due to transition**

	Position	S4	S5	S6	S7	S8
x=0.11	$\alpha \nearrow (\psi)[°]$			10.11 (204.9)		
	$\alpha \searrow (\psi)[°]$			9.52 (342.3)		
	$\Delta\alpha[°]$			**0.59**		
x=0.15	$\alpha \nearrow (\psi)[°]$	11.89 (231.0)	9.35 (195.7)	8.95 (190.9)	8.76 (188.8)	9.15 (193.3)
	$\alpha \searrow (\psi)[°]$	11.60 (313.9)	8.64 (352.6)	8.37 (355.8)	8.18 (357.9)	8.70 (351.9)
	$\Delta\alpha[°]$	**0.28**	**0.71**	**0.58**	**0.58**	**0.45**
x=0.19	$\alpha \nearrow (\psi)[°]$	10.28 (207.1)				
	$\alpha \searrow (\psi)[°]$	9.73 (339.8)				
	$\Delta\alpha[°]$	**0.55**				
x=0.23	$\alpha \nearrow (\psi)[°]$	9.21 (194.0)				
	$\alpha \searrow (\psi)[°]$	8.44 (355.0)				
	$\Delta\alpha[°]$	**0.77**				
x=0.27	$\alpha \nearrow (\psi)[°]$	7.63 (175.8)				
	$\alpha \searrow (\psi)[°]$	7.24 (8.8)				
	$\Delta\alpha[°]$	**0.40**				
x=0.39	$\alpha \nearrow (\psi)[°]$	5.37 (148.2)				
	$\alpha \searrow (\psi)[°]$	5.08 (35.8)				
	$\Delta\alpha[°]$	**0.29**				

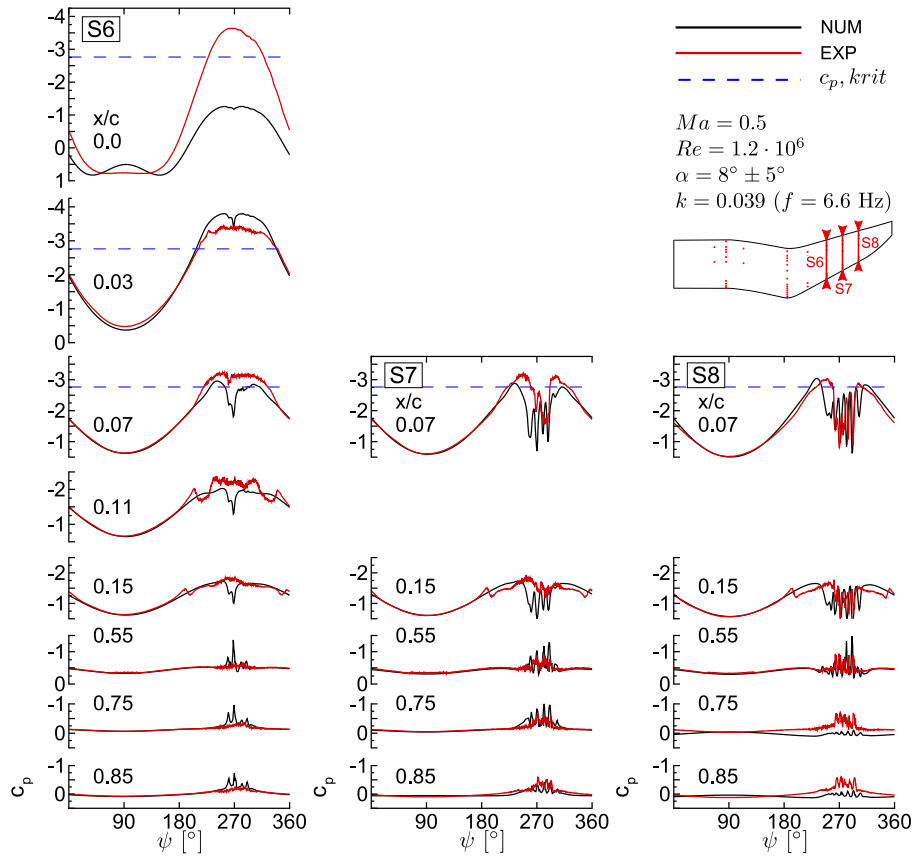Figure 5.11: $Ma = 0.5$, $Re = 1.2 \cdot 10^6$, $\alpha = 8° \pm 5°$, **pressure data of sections 6-8**

The almost same c_p-levels of the sections S6 and S7 (Fig. 5.11) in the parts of the cycle where the flow is not separated is remarkable: again, the influence of the planform seems to compensate the reduced geometric twist towards the tip. Furthermore, the position of the transition drops at $x = 0.15$ is nearly unchanged from S6 and S7. Only at S8 the transition is found at slightly increased angles of attack. This observation and the slightly reduced c_p-level in S8 indicate the influence of the tip vortex.

The experimental data in section S6 show small oscillations and a slightly elevated suction level at the trailing edge around the maximum angle of attack. A small but sharp drop can be seen at $\psi \approx 260$ at $x/c = 0.07$ which increases significantly at the further outboard sections. This drop is stronger in the numerical data and shows up slightly phase shifted from $x/c = 0.03$ to $x/c = 0.15$. This indicates a vortex traveling from the leading to the trailing edge which also explains the phase shifted suction peak which shows up from $x/c = 0.55$ to $x/c = 0.85$. However, in the experimental data of S6 the drop cannot be detected in the signals further downstream than $x/c = 0.03$. The experimental suction peak at the leading edge is significantly higher in S6 than in S4, although the geometric angle of attack is reduced from S4 to the tip. The suction peak is not captured by the computations at $x/c = 0.0$. However, there is a higher suction level for the numerical data at $x/c = 0.03$. This shift of the suction peak is discussed later on. The angles of attack at which transition occurs are marginally lower than in S5.

The c_p-distributions in the sections S7 and S8 show a very similar behavior. Around the maximum angle of attack $\alpha_{max} = 13°$ a sharp drop in the suction peak at $x/c = 0.07$ can be seen. This

drop occurs slightly earlier in the numerical data and is followed by strong oscillations. There is a slight phase shift between the oscillations in section S7 and S8 as well as between the computational and experimental oscillations. In section S7 the computations show stronger oscillations and better discernible peaks than the experimental data. In section S8 the experimental oscillations are strongest and are well captured by the computations. Only at the trailing edge there is a higher suction level in the experimental data. The five discernible oscillation peaks, the inversed gradients from $x/c = 0.15$ to $x/c = 0.55$ and the phase shift of the oscillations across the chord indicate up to five vortices traveling from the leading to the trailing edge. Dividing the distance between two sensors by the time shift of one discernible peak shown by both sensors yields the travelling speed of the vortices. At section S8, the speed varies between 27 m/s $< u_{vtx,EXP} <$ 52 m/s in the experiment and 28 m/s $< u_{vtx,NUM} <$ 43 m/s in the computations. In both cases, the last vortex has a slower travelling speed than the first one. The flow seems to be "blocked" by the first vortex which is travelling much slower than the inflow velocity $u_\infty = 169$ m/s. Further inboard the experimental c_p-peaks are too ambiguous to calculate $u_{vtx,EXP}$.

The spectral content of the measured angle of attack and two pressure transducers is shown in Fig. 5.12. Considering the angle of attack, the absolute value of all higher harmonics are almost two orders of magnitude lower than the desired pitching frequency. The absolute value of the second and third higher harmonics of the pressure signal at $x/c = 0.07$ of section S4 are slightly elevated. Still, they are more than 1.5 orders of magnitude lower than the pitching frequency. The pressure transducer of section S8 shows a very broad spectrum over the whole frequency domain. No specific peaks can be detected even though the signal in Fig. 5.11 showed strong oscillations. Thus, one can conclude that the model is not excited by the vortices passing over the structure.
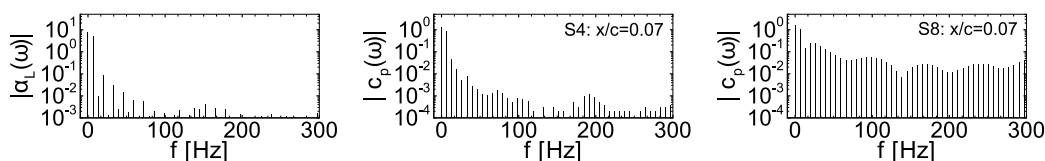

Figure 5.12: $Ma = 0.5$, $Re = 1.2 \cdot 10^6$, $\alpha = 8° \pm 5°$, **spectral content**

In order to enlighten which processes lead to the peaks and oscillations in the pressure distributions, the outboard section is investigated in detail at high angles of attack.

Flow phenomena at selected high angles of attack

The numerical and experimental c_p-distributions are investigated and compared in Figs. 5.13-5.17 for seven instantaneous points (A-G) at high angles of attack. For the convenience of the reader, these Figures are arranged in just two Figs. 5.18 and 5.19. Only the outboard part of the blade tip where flow separation is expected is considered. The numerical flow field is presented with the colorcoded spanwise velocities and the sectionswise streamlines which are computed by the velocities in x- and z-direction. A cutout of the fully integrated sectional numerical lift and moment coefficients are shown, on the top of each figure. The selected points have been chosen according to remarkable characteristics in the computed C_l- and C_m-distributions.
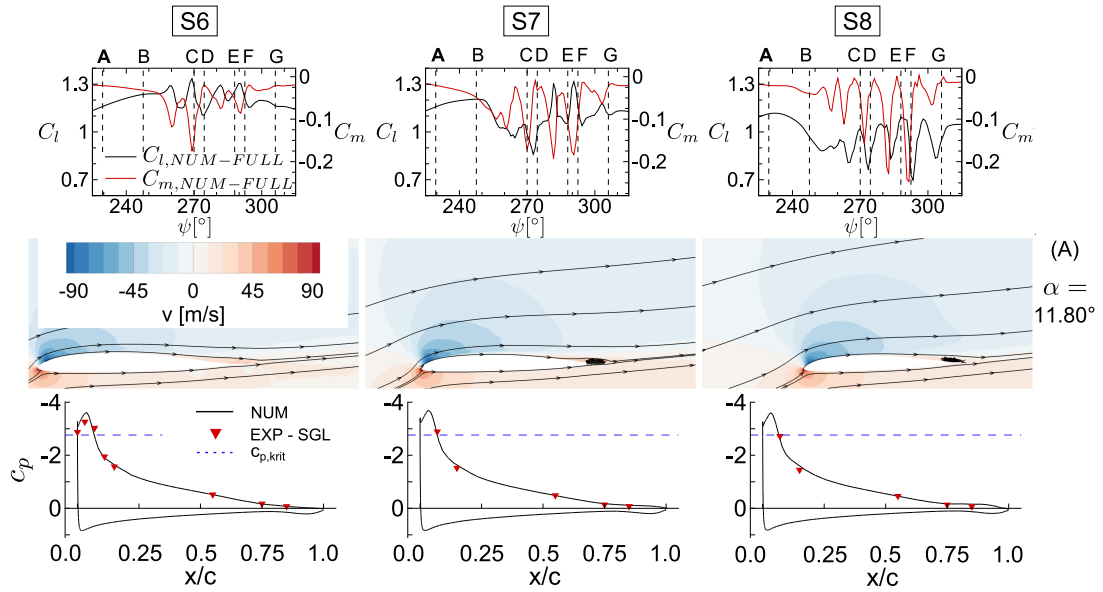
Figure 5.13: **Instantaneous flowfield and c_p-distributions for $\alpha = 11.8°$ ↗**

$\alpha = 11.8°$ ↗, shown in Fig. 5.13

S6-S8: The c_p-distributions look very similar for all three sections except for differences at the trailing edge. A tendency of increased flow separation towards the tip can be deduced from the streamlines and the increased suction level at the trailing edge of S7 and S8. The experimental data do not show this behavior at the trailing edge but generally fit in well to the computed c_p-curves. Even the agreement of the strong gradient at the shock position at $c_{p,crit}$ is good. At the leading edge, the computed c_p-distributions show a small peak with a sudden decrease in front of the proper suction peak. This phenomenon occurs at almost all subsequent presented angles of attack and might be due to a too coarse CFD-grid at the leading edge. A physical explanation could be a curvature discontinuity in the geometry. However, a much higher number of pressure transducers at the leading edge would have been required to resolve such a phenomena experimentally. The suction peak is sharper and slightly decreased at S8 which explains the reduced C_l-coefficient at S8. The C_m-coefficient, calculated with respect to the local quarter-chord is almost zero for the sections S6-S8. Due to the backward sweep, there is a strong pressure compensation at the leading edge which leads to high velocities in y-direction near the stagnation point. At the trailing edge, the sweep also leads to the strong spanwise deflection of the flow towards the blade tip. The y-velocity distribution is very similar for all three sections.

$\alpha = 12.62°$ ↗, shown in Fig. 5.14

S6: The computations show the onset of flow separation at the trailing edge. The reversed flow indicated by the streamlines lead to a slightly elevated suction level at the trailing edge. Thus, the $C_{m,NUM}$-coefficient is also reduced although the suction peak has further increased. The $C_{l,NUM}$-coefficient increases nonlinearly. The spanwise velocity components have slightly increased. The experimental results do not fit to the numerical suction peak. They show a plateau at the three transducers at the leading edge with the strongest suction at $x/c = 0.0$. The plateau often indicates a laminar separation bubble which cannot be reflected by fully turbulent URANS
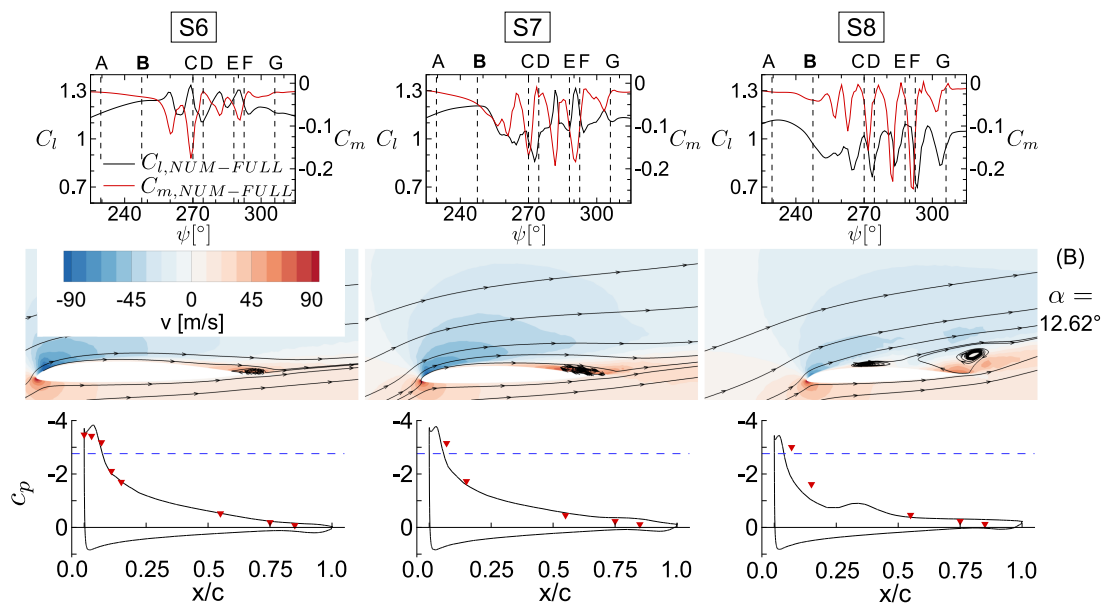
Figure 5.14: **Instantaneous flowfield and** c_p**-distributions for** $\alpha = 12.62°$ ↗

computations. The experimental flow is still attached.

S7: The trailing edge separation has extended, a broad vortex on the trailing edge can be seen in the computed data. This leads to an elevated suction at the trailing edge and consequently to the decreased $C_{m,NUM}$. This behavior is not reflected by the experimental data. No elevated c_p-level at the trailing edge indicating flow separation is visible. However, the experimental data shows a sharper and increased suction peak at the leading edge, as it can be seen in the numerical data. This explains the nonlinear increase of the lift coefficient $C_{l,NUM}$ which is close to its maximum.

S8: The computed suction peak has decreased and shows a sharper shape which leads to a negative slope of the lift curve $C_{l,NUM}$. Two vortical structures are visible in the streamlines. One has already detached from the trailing edge. Thus, its influence on the pressure distribution is limited and the c_p-level only slightly lower at the trailing edge. The vortex is highly three-dimensional and has strong spanwise velocity components. The roll up of the vortex is not exactly in upstream direction. Thus, the spanwise velocity component of the reversed flow has the opposite sign. The other vortical structure at $x/c \approx 0.35$ is closer to the surface. The induced suction at this position can be clearly seen in the c_p-distribution. Due to the elevated suction caused by the vortices, the $C_{m,NUM}$-coefficient has decreased but is still at about the same level as at section S7. The experimental data indicates attached flow.

$\alpha = 13.00°$, shown in Fig. 5.15

S6: The computations show strong flow separation. However, the sharp and slightly reduced suction peak at the leading edge does not collapse. The lift coefficient $C_{l,NUM}$ is below its second and absolute maximum. Two broad vortical structures significantly influence the c_p-distribution. An elevated suction at $x/c = 0.35$, which continues up to the trailing edge, can be seen. This leads to the second and absolute minimum in the C_m-distribution. From the three-dimensional streamlines plotted in Fig. 5.16 one can conclude that the two vortical structures belong together. The center of the flow separation is further outboard and the roll up of the vortex is not exactly
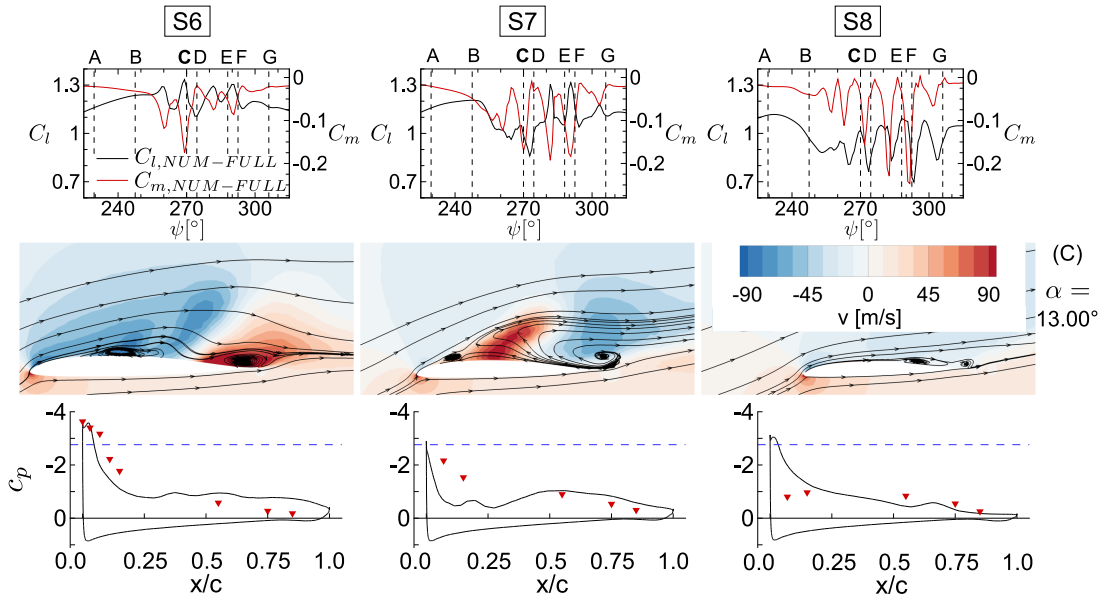
Figure 5.15: **Instantaneous flowfield and c_p-distributions for $\alpha_{max} = 13.0°$**

in upstream direction. The vortex structures are highly three-dimensional and seem to build a vortex ring. This explains the increased spanwise velocities. The incoming flow is deflected in inboard direction. Near the trailing edge, the flow is deflected in outboard direction. The experimental c_p-distribution does not show strong signs of flow separation. The suction at $x/c = 0.0$ is further increased and only a slightly elevated suction level at the trailing edge indicate the beginning of instabilities in the flow.

S7: The experimental data show undoubtable signs of separated flow. The suction level at $x/c = 0.07$ has decreased, and the suction level at the trailing edge has increased which leads to a negative pitching moment peak, shown in Fig. 5.8. The computations predict even stronger flow separation: the suction peak at the leading edge has collapsed. The C_l-curve is close to the absolute minimum. Its slope is negative. Two vortex structures are discernible in Fig. 5.15. As mentioned above, they both belong to the separated flow region, shown in Fig. 5.16. One big vortical structure leaves the trailing edge, still leading to an elevated c_p-level on the back half of the section. The small front vortex structure is located close to the quarter chord. The spanwise velocities are inverse to the velocities in section S6. Therefrom and from the three-dimensional streamlines in Fig. 5.16, one can deduce that the center of the separated flow is between the two sections S6 and S7. The incoming flow splits around the center of reversed flow. Near the trailing edge, the flow changes the spanwise direction towards the lowest pressure level. The moment coefficient is at its first significant minimum.

S8: The experimental c_p-values show strong flow separation. The suction peak around the leading edge has collapsed. The suction level at the trailing edge significantly increased. The computed flow is nearly attached. Only one small vortex close to the surface leads to the elevated c_p-level at $x/c \approx 0.65$. Thus, the $C_{l,NUM}$-coefficient is at a local maximum and the $C_{m,NUM}$-coefficient is close to zero. In Fig. 5.8, one can see the slight phase-shift between the experimental and computed moment distribution of section S8. Therefrom, one can deduce that stronger separated flow is found at a slightly higher angle of attack for the computations.
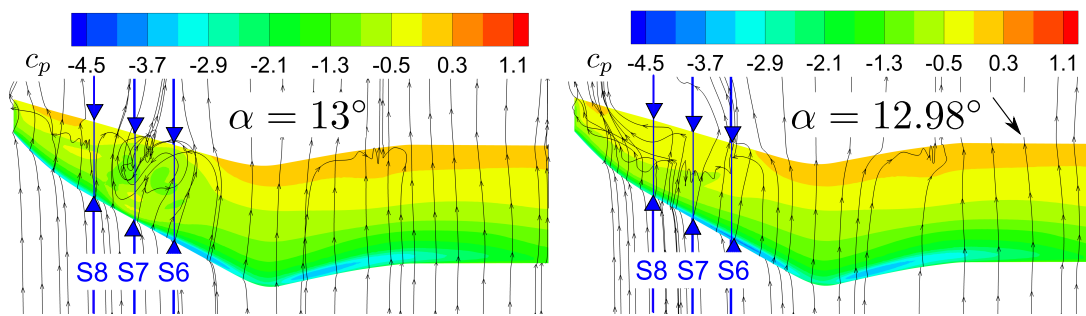
Figure 5.16: $Ma = 0.5$, $Re = 1.2 \cdot 10^6$, $\alpha = 8° \pm 5°$; **instantaneous flowfields**

$\underline{\alpha = 12.98° \searrow}$, shown in Fig. 5.17

S6-S8: All numerical pitching moments are close to zero.

S6: The experimental c_p-distribution is virtually unchanged in comparison to $\alpha = 13.00°$. The flow is fully attached. In the numerical data, an only slightly elevated suction level and reversed flow at the trailing edge are evident. Since the back part of the big vortex structures has just passed the trailing edge, the lift level has decreased to a local minimum. As one can see in Fig. 5.16 the separated flow has little influence on section S6 anymore.

S7: The flow has reattached at the leading edge. Thus, the suction peak is clearly visible again. The front part of the computed vortex structure has moved from $x/c \approx 0.2$ at $\alpha = 13°$ to $x/c \approx 0.5$. At the trailing edge, the computed suction level has decreased. The spanwise velocities and the 3D-streamlines in Fig. 5.16 indicate that the separated flow region has moved in spanwise direction towards the tip. The experimental data cannot resolve these detailed phenomena. However, the transducer closest to the leading edge shows a higher suction level than at $\alpha = 13.0°$. Furthermore, the c_p-level at $x/c = 0.85$ is higher than at $x/c = 0.75$. These are signs that a vortex travels from the leading to the trailing edge between $\alpha = 13.0°$ and $\alpha = 12.98°$. This phenomenon becomes more evident in the experimental data of section S8.

S8: The moment coefficient has nearly the same level as at $\alpha = 13°$. The lift has decreased and stronger separated flow is visible in Figs. 5.17 and 5.16 than at $\alpha = 13°$. The vortical structures near the trailing edge have strong spanwise velocities in root direction. The computed spanwise velocities and c_p-distribution have similar characteristics as section S7 at $\alpha = 13°$: a front vortical structure, here behind the local quarter chord. Another vortical structure near the trailing edge, here with less influence on the c_p-distribution. The separated flow regions seems to have shifted towards the tip. Separated flow is also seen in the experimental data: the suction near the trailing edge has increased, but the c_p-level at $x/c = 0.85$ is higher than at $x/c = 0.75$.

$\underline{\alpha = 12.76°\,(E) - 12.05° \text{ (G)}}$, shown in Fig. 5.17

S6: The computed c_p-distributions are very similar for all three angles of attack. The separated flow at the trailing edge has vanished at the last angle of attack and the moment coefficient is close to zero at point (G). The spanwise velocities are similar to point (A). The experimental data show no signs of separated flow. The plateaus at points (E) and (F) might indicate a laminar separation bubble. Besides the suction peak, the experimental and numerical data show an excellent agreement.
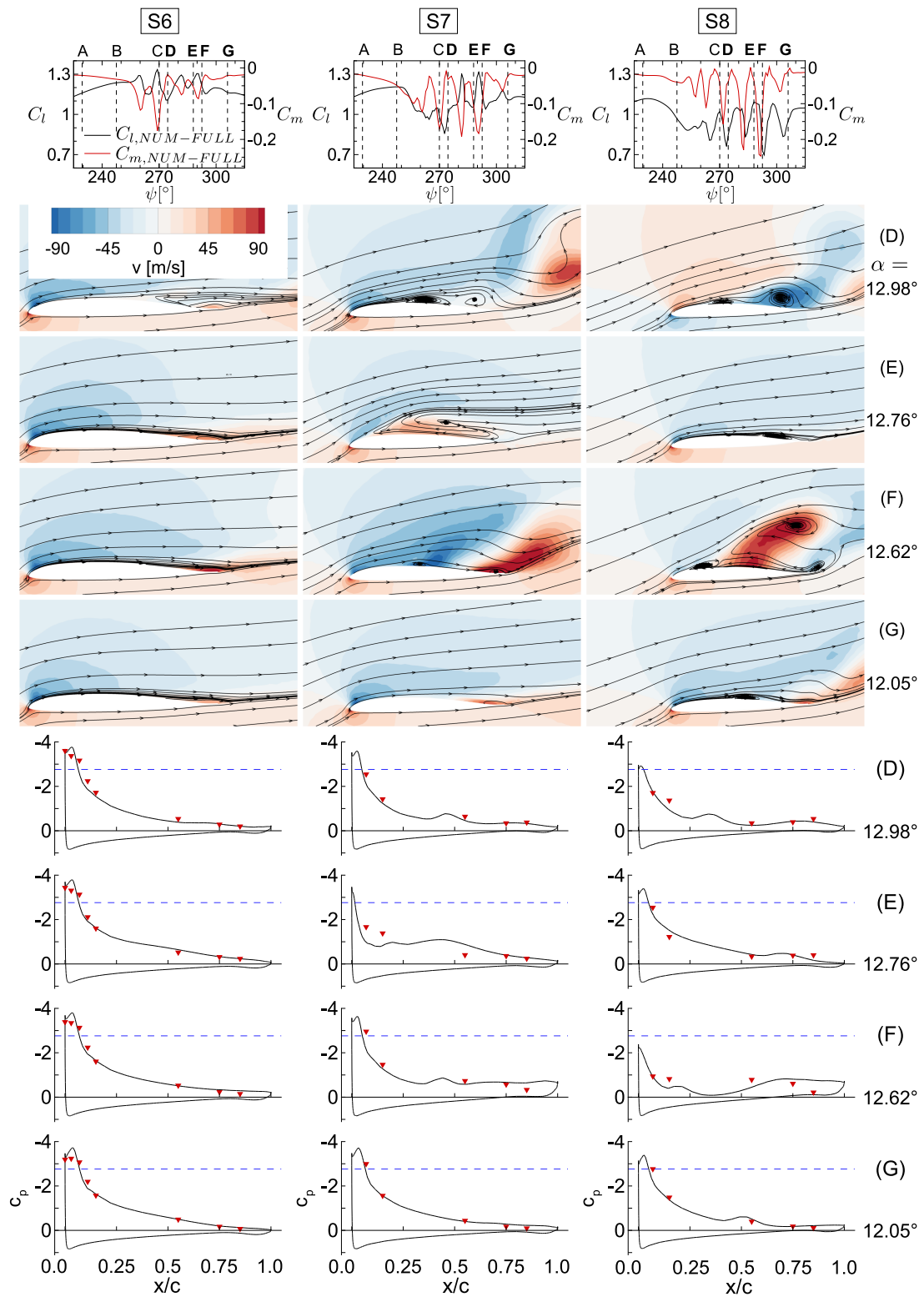
Figure 5.17: **Instantaneous flowfield and c_p-distribution for** $\alpha = 12.98° \searrow -12.05° \searrow$

S7: Points (E) and (F) are before and behind a secondary lift peak. The computed vortical structures are located downstream of the leading edge so that the suction peak is less affected than at point (C). Due to the vortices near the trailing edge, the pitching moment coefficient $C_{m,NUM}$ is reduced. Only at point (G), where the flow is nearly attached, the moment coefficient is again close to zero. The experimental data also show detached flow at point (E) where the suction at $x/c = 0.07$ has collapsed. At point (F) the suction peak has established again, but the transducers near the trailing edge show an elevated level. This indicates a vortex passing by. At point (G), the experimental data shows attached flow and fits perfectly to the computed c_p-curve.

S8: The computed flowfield, the c_p-distributions and the coefficients $C_{l,NUM}$ and $C_{m,NUM}$ at point (E) are similar to point (C). The same yields for the points (F) and (D). The separated flow is slightly stronger in (F) than in (D) and the $C_{l,NUM}$-slope is negative. The experimental and numerical data show a good agreement at point (E) and even for the strongly separated flow at point (F). The $C_{m,NUM}$-coefficient is short before a minimum, the $C_{l,NUM}$-coefficient is short behind a minimum at point (F).

Summary of the light dynamic stall case

The investigation of the light dynamic stall at $Ma = 0.5$, $Re = 1.2 \cdot 10^6$, $\alpha = 8° \pm 5°$ and $k = 0.039$ case has shown the following:

- ⇁ Dynamic stall can be clearly detected in the global balance data. The higher harmonic oscillations in the pitching moment cannot be captured by the numerical data whereas the global behavior shows a good agreement to the experimental data.

- ⇁ The sectional pitching moments increase to positive values at the forward-backward kink with an increasing angle of attack. The pitching moments decrease to high negative values at the backward swept outboard section. The global pitching moment shows an well-balanced model.

- ⇁ Drops in the c_p-distribution indicated laminar-turbulent transition. Compared to the forward-backward kink, the transition is located closer to the leading edge at the backward swept part.

- ⇁ Similar to the static data, first dynamic stall occurs at the backward swept part of the blade tip. The strong crossflow velocities, which are caused by the planform, stabilize the flow at the forward-backward kink.

- ⇁ As soon as stall sets in, the lift, the moment and the pressure data show strong oscillations at the backward swept part. The computations show a qualitatively good agreement to the experimental data. The states of attached flow and strong flow separation with discernible vortices alternate. The alternation is different at all spanwise sections. From this one can deduce that there is not one single big vortex, but rather small vortical structures. They are highly affected by the strong crossflow velocities.

In Fig. 5.18 and Fig. 5.19, the flow phenomena at high angles of attack are recapitulated.
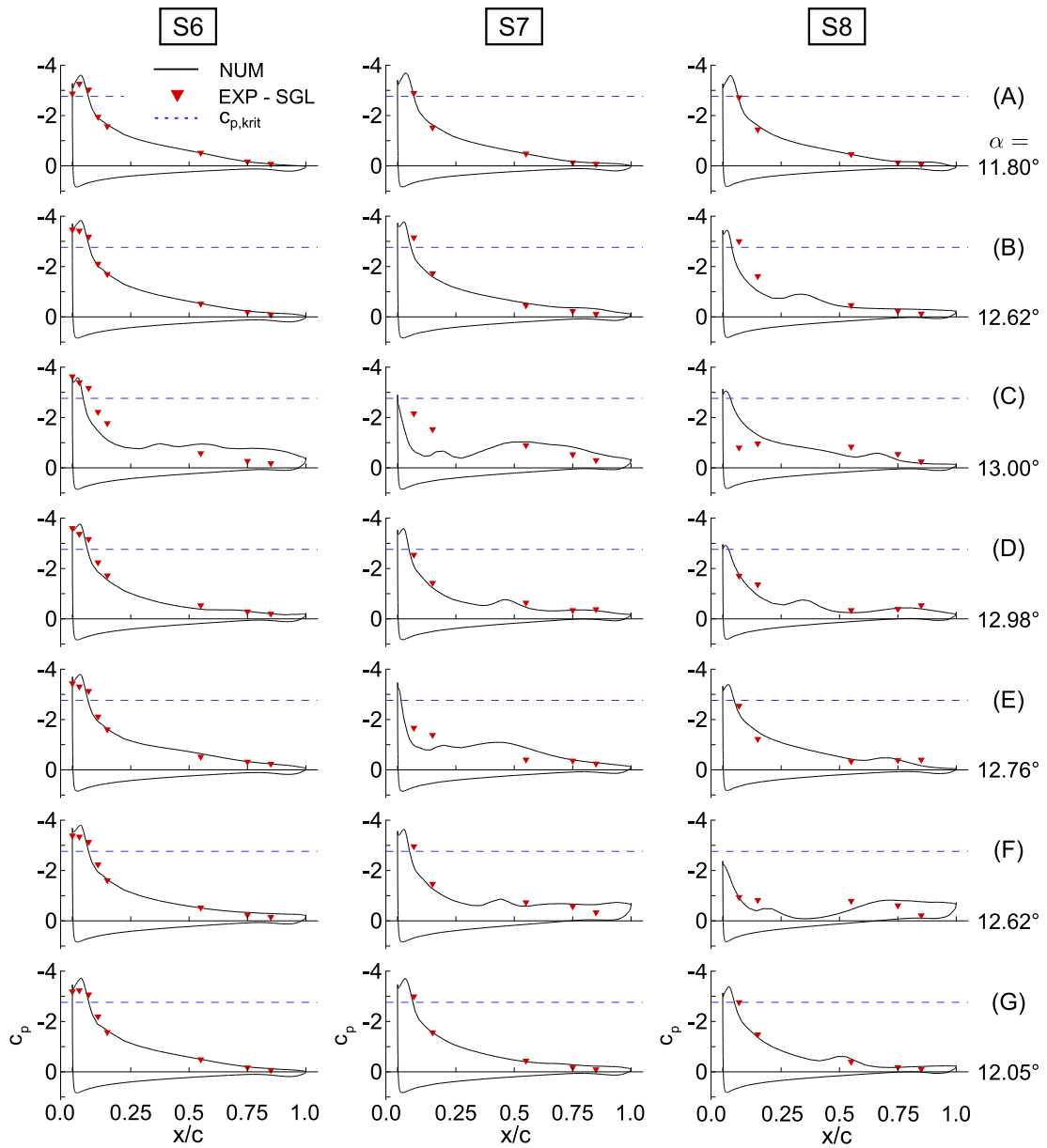

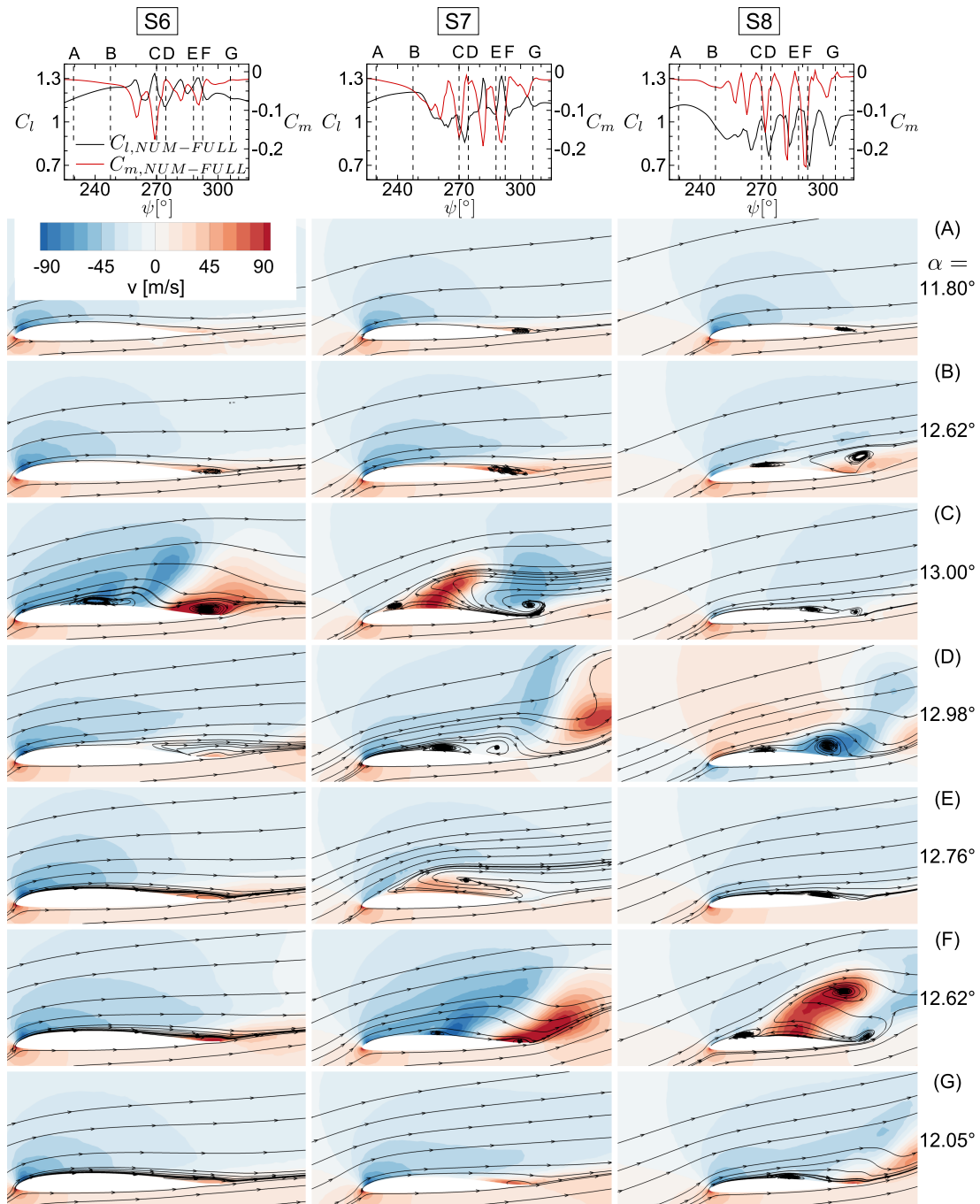Figure 5.18: $Ma = 0.5$, $Re = 1.2 \cdot 10^6$, $\alpha = 8° \pm 5°$, c_p-distribution

Figure 5.19: $Ma = 0.5$, $Re = 1.2 \cdot 10^6$, $\alpha = 8° \pm 5°$, **Flowfield**

Deformation of the Wind Tunnel Model

The deformation is maximum for the presented test case due to the high stagnation pressure and the high angles of attack which cause the maximum loads. In the left plot of Fig. 5.20, the total geometric angle of attack is plotted for two spanwise positions. In the middle plot, the elastic part of the geometric angle of attack α_{ELAS} is depicted. In the right plot, the elastic deformation in z-direction (lift) is shown. The most outboard position where marker could be recorded is at $y/R = 0.9$. The most inboard section which could be recorded was used for the calculation of α_{nom}.
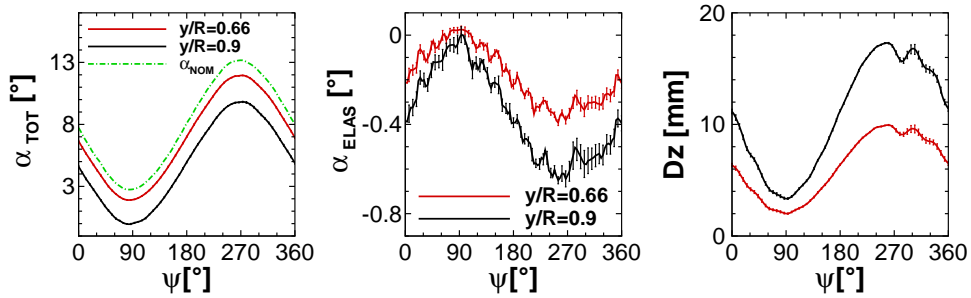

Figure 5.20: **Geometric angle of attack α_{TOT}, elastic part α_{ELAS} and z-deformation; measured with respect to the local quarter chord**

The elastic part of the angle of attack can hardly be seen in the left plot. First of all, the geometric twist distribution can be deduced from the difference between the curves. Only in the middle plot, one can see that the elastic angle of attack reaches up to $\alpha_{ELAS} \approx -0.7°$ at the tip. Most of the characteristic oscillations are found at $y/R = 0.66$ and at $y/R = 0.9$. Thus, the deformation seems to be global. One significant increase at the maximum angle of attack correlates with the drop in the elastic bending deformation D_z at $\psi \approx 270°$. The maximum bending deformation $D_z = 17$ mm is at $\psi = 258°$. As shown in Fig. 5.11, the minimum c_p-level at $x/c = 0.07$ of S7 and S8 is at $\psi = 251°$, then it is also followed by a strong drop. One can conclude, that the drop in the elastic bending deformation is caused by the separated flow at the outboard section. The phase difference between stall and deformation is about $\Delta\psi = 7°$. The phase difference at the reattachment point is close to zero. However, the meaning of the phase differences is arguable, since a local pressure distribution is compared to a sectional deformation which is caused by the pressure applied on the whole blade.

The maximum velocity which is induced by the deformation at $y/R = 0.9$ is estimated by

$$u_{ind} = \frac{\Delta D_z}{\Delta t}. \tag{5.7}$$

The calculation is done for $\psi_1 = 309.7°$ and $\psi_2 = 317\cdot5°$ where the strongest gradients occur. The induced velocity is about 0.27 m/s which is 0.12% of the inflow velocity. This influence is negligible. Thus, one can conclude that role of the elastic angle of attack which is caused by the bending-torsion coupling is much more important than the induced velocity caused by the deformation. Due to the high loads, investigations at higher angles of attack have been only carried out at lower Reynolds numbers. Before investigating a deep dynamic stall case at $\alpha = 10° \pm 5°$ and $Re = 0.72 \cdot 10^6$, the influence of the Reynolds number is presented. Therefore, LC-DS1 is compared to LC-DS2 where all parameters are kept constant except for the Reynolds number.

5.3 Influence of the Reynolds Number

The Reynolds number is varied from $Re = 1.2 \cdot 10^6$ in LC-DS1 to $Re = 0.72 \cdot 10^6$ in LC-DS2. The other parameters are unchanged. As in the preceding section, c_p-ψ-distribution of each pressure transducer is presented for the sections S2 and S4-S8 in Figs. 5.21 and 5.22. However, in this section the phase-averaged results are presented and no data of single periods are shown. The error bars indicate the cycle-to-cycle variation.
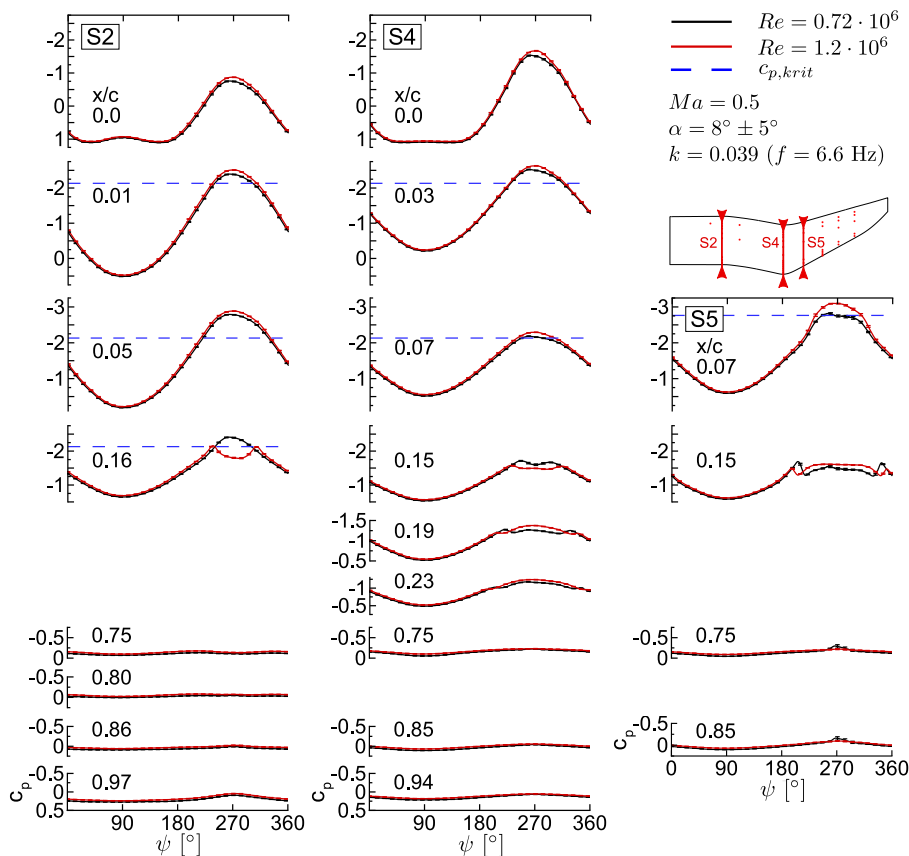

Figure 5.21: **Phase-averaged c_p-distributions of S2, S4 and S5 for different Reynolds numbers**

There is only little difference between the two Reynolds numbers in the sections S2 and S4. The suction level is slightly smaller and the laminar-turbulent transition drops are shifted in downstream direction for the lower Reynolds number. This can be clearly observed at $x/c = 0.15$ and $x/c = 0.19$ of section S4. However, comparing the drop at $x/c = 0.19$ at $Re = 0.72 \cdot 10^6$ to the drop at $x/c = 0.15$ at $Re = 1.2 \cdot 10^6$, one can state that the difference in the position of the drops is less than 4% of the chordlength.

At section S5, an elevated suction level at $\psi \approx 270°$ at the trailing edge can be observed for the lower Reynolds number. At slightly lower phase angles this small peak can be detected at the transducers located further upstream. A vortex travelling from the leading to the trailing edge could explain this behavior.
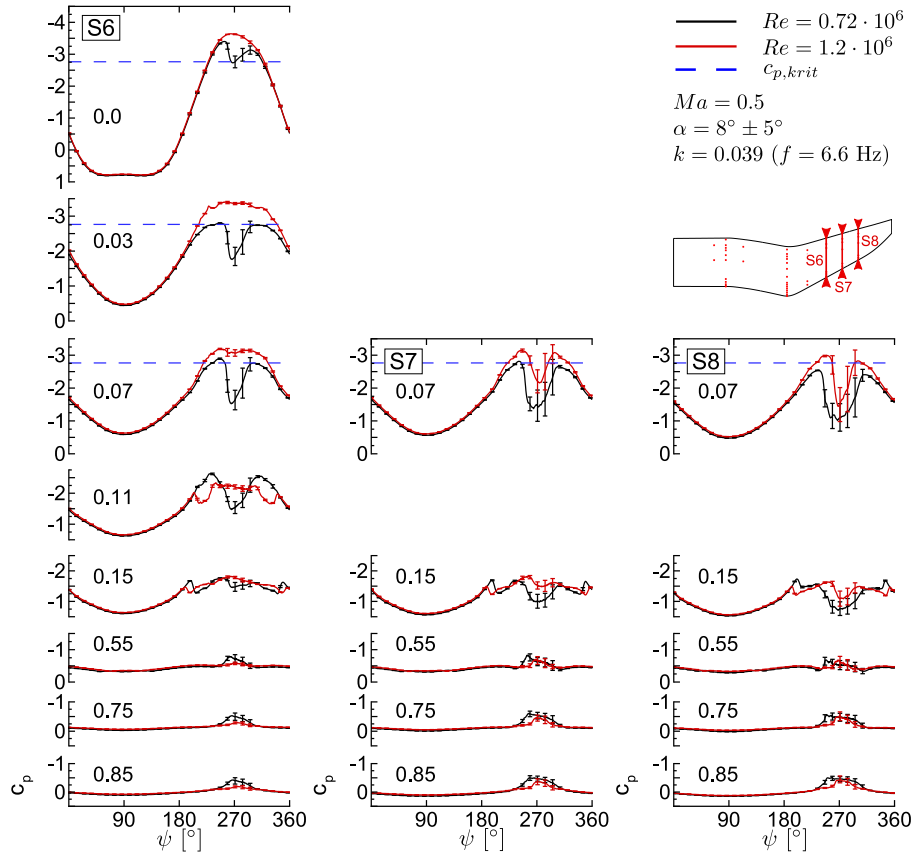
Figure 5.22: **Phase-averaged c_p-distributions of S6-S8 for different Reynolds numbers**

The tendency towards stronger separated flow for $Re = 0.72 \cdot 10^6$ is proved by the c_p-distributions of the outboard sections S6-S8. As one can see at $x/c = 0.15$ for S6-S8, the laminar boundary layer increases for the lower Reynolds number, similar to the inboard sections. As described in Schlichting [58], the laminar boundary layer is less stable then the turbulent boundary layer. Thus, stall is delayed to higher angles of attack at the higher Reynolds number where the laminar-turbulent transition is shifted upstream. Only small signs of flow separation can be observed for $Re = 1.2 \cdot 10^6$ at section S6. On the contrary, a collapsed suction peak at the leading edge and an elevated suction level at the trailing edge can be observed around the maximum angle of attack for $Re = 0.72 \cdot 10^6$. A stronger drop in the leading edge suction can also be observed at the sections S7-S8. A larger part of the cycle shows detached flow. The increased standard deviations indicate stronger oscillations.

5.4 Deep Dynamic Stall

Increasing the mean angle of attack by from $\alpha_{mean} = 8°$ to $\alpha_{mean} = 10°$ while keeping all other parameters of LC-DS2 constant leads to a deep dynamic stall case. In Fig. 5.23 and Fig. 5.24, one single period of each test case is shown. Whereas LC-DS2 with $\alpha_{mean} = 8°$ is attached over
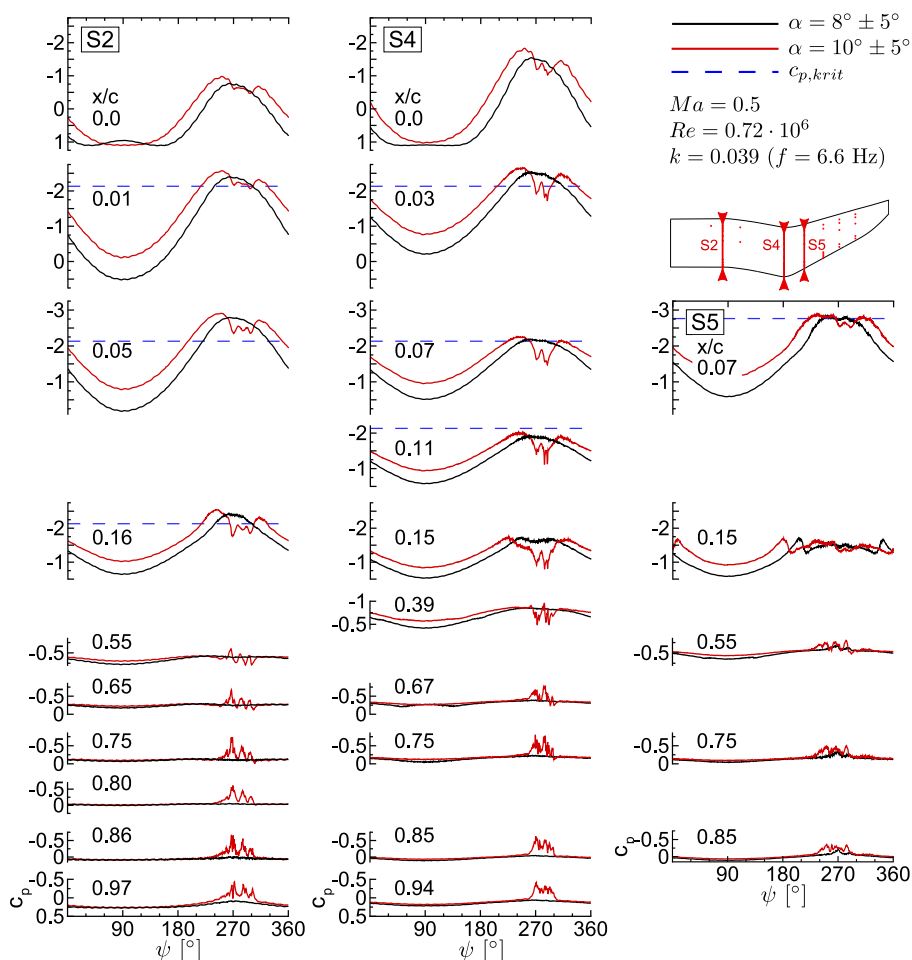
Figure 5.23: **Single periods of LC-DS2 ($\alpha = 8° \pm 5°$) and LC-DS3 ($\alpha = 10° \pm 5°$)**

the whole cycle at the inboard sections, LC-DS3 with $\alpha_{mean} = 10°$ shows separated flow around the maximum angle of attack at all sections.

At section S2, the suction level at the leading edge is higher for LC-DS3 before the maximum angle of attack. At $\psi \approx 240°$ a drop can be observed at $x/c = 0.0 - 0.16$. This drop is followed by well discernible oscillations. Except for the first drop, these oscillations occur at slightly higher phase angles at the trailing edge. The first drop starts at the trailing edge indicating trailing edge separation. The separated flow moves forward towards the leading edge with increasing angle of attack. The elevated suction at the trailing edge vanishes. When the separated flow is close to the leading edge the suction peak collapses. A discernible vortex separates close to the leading edge and starts travelling downstream. Now, elevated suction levels are moving in downstream direction. The flow reattaches and might separate again immediately in case of an unfavorable pressure gradient. At S2, the downstream velocity of the vortices is decreasing from $u_{vtx} \approx 80$ m/s of the first vortex to $u_{vtx} \approx 23$ m/s of the last vortex.

At section S4, the peaks of LC-DS3 cannot be unambiguously associated. Since S4 is the last section where flow separates, one might see effects of detached vortices further inboard and outboard. No clear vortices travelling across the blade at section S4 can be detected.

While section S5 shows only slightly separated flow around the maximum angle of attack, the
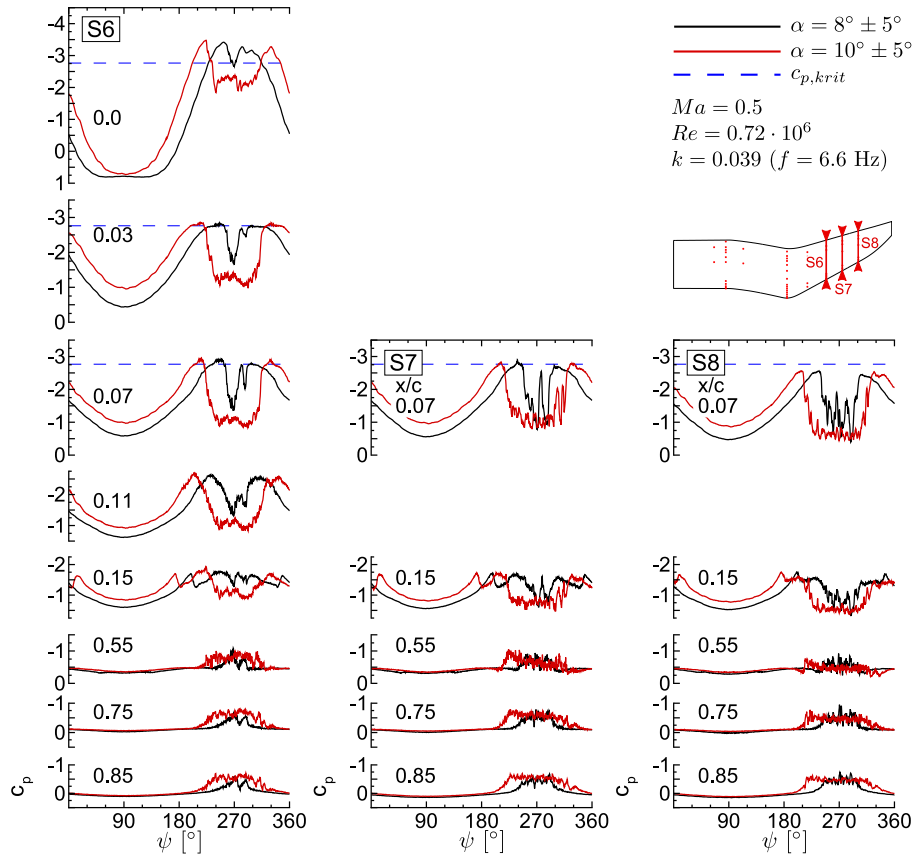
Figure 5.24: **Single periods of LC-DS2 ($\alpha = 8° \pm 5°$) and LC-DS3 ($\alpha = 10° \pm 5°$)**

separated flow region is increased drastically towards the blade tip. For both angles of attack, the maximum separation can be seen at S7-S8. For $\alpha = 10° \pm 5°$ the flow is detached from $\psi \approx 210°$ ($\alpha = 10.5\circ$ ↗) to $\psi \approx= 330°$ (($\alpha = 10.5$ ↘)). However, no discernible discrete vortices can be deduced from the c_p-distributions. For $\alpha = 8° \pm 5°$ the flow is detached from $\psi \approx= 240°$ ($\alpha = 12.33°$ ↗) to $\psi \approx= 300°$ ($\alpha = 12.33°$ ↘) at the sections S7-S8. The maximum suction level is reached, one clearly discernible peak can be seen in the c_p-distribution of S6 and S7. Since the shape of the peak varies significantly from the leading to the trailing edge, it is not possible to determine the travelling velocity of the vortex. One can state, that discernible vortices do not necessarily occur in regions of strongly separated flow. If vortices occur, they do not travel exactly in downstream direction but are deflected by the spanwise velocities.

5.5 Influence of Pitching Frequency

The influence of the pitching frequency is investigated by means of the test cases LC-DS4 ($f = 3.3$ Hz) and LC-DS5 ($f = 9.9$ Hz), shown in Fig. 5.25. The c_p-distributions are shown only for the sections S2, S4 and S5 since the tendencies are similar for the outboard sections. The differences between the two test cases decrease from S2 towards the tip. In order to show

them more clearly, the standard deviation is not indicated here. The lower pitching frequency $f = 3.3$ Hz yields a reduced frequency of $k = 0.0196$. The higher pitching frequency $f = 9.9$ Hz yields a reduced frequency of $k = 0.0588$. At this frequency, the maximum suction peak and consequently stall is postponed to higher angles of attack for all sections. Due to the stronger motion induced downwash, the c_p-distributions are less symmetric around the maximum angle of attack for $f = 9.9$ Hz than for $f = 3.3$ Hz. The reattachment is postponed to higher phase angles for the higher frequency, similar to the results of McCroskey [16] and Carr [14].

At section S2, one notices two discernible peaks even though the data is phase averaged. More distinct, repeatable vortices seem to travel across the blade tip at the higher frequency.
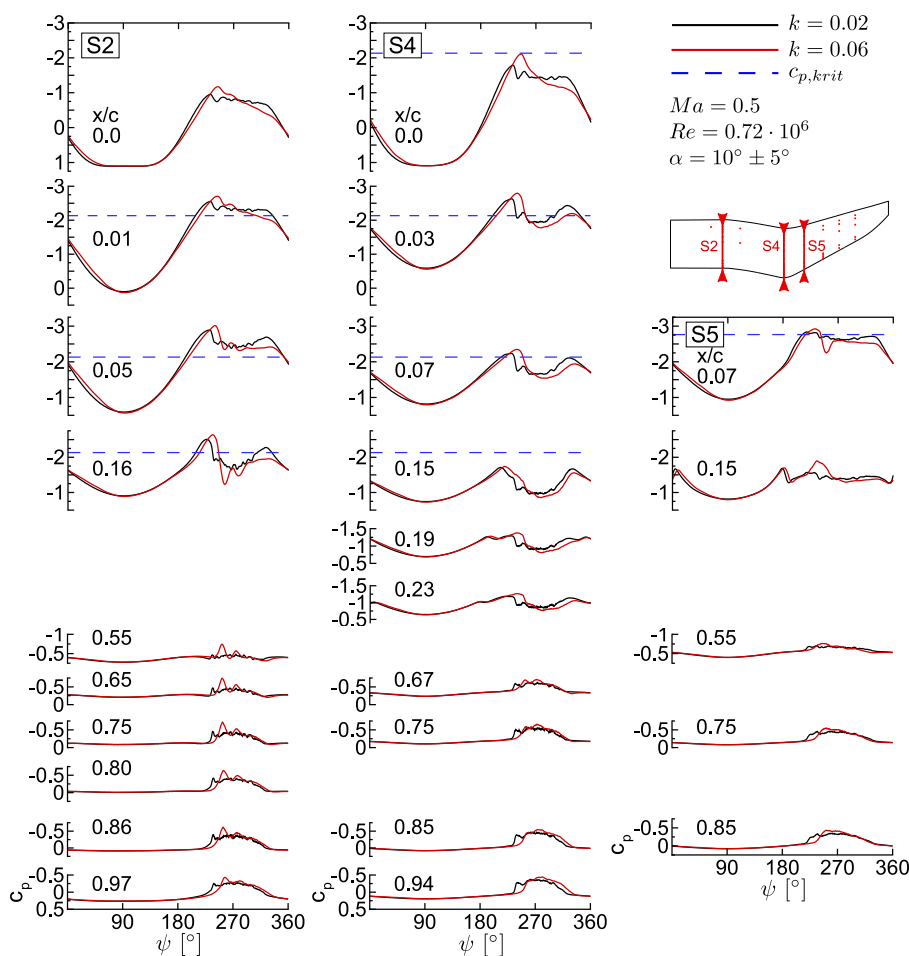
Figure 5.25: **Phase-averaged c_p-distributions for $f = 3.3$ Hz vs $f = 9.9$ Hz**

5.6 Comparison to Two-Dimensional Experiments

In the following, the test case LC-DS3 is compared to 2D experimental data of the airfoils EDI-M112 and EDI-M109 [24]. Thus, the differences between the advanced planform and the midsection of a 2D rectangular wing can be studied. A straight-forward comparison between two test cases is not possible. Due to the twist distribution of the blade tip (Fig. 3.1) and the

availability of certain measurement points only, different test cases are compared at the span-
wise sections S2, S4 and S6, shown in Fig 5.26. The phase-averaged data is presented. For the
convenience of the reader the standard deviation is only indicated for the sensors from the lead-
ing edge to $x/c = 0.16$. At section S2, the 3D test case LC-DS4 ($\alpha = 11° \pm 5°$) is used instead of
LC-DS3. Thereby, the airfoil, the oscillation amplitude and the geometric angle of attack match
approximately at each section. The Mach number $Ma = 0.5$ and the pitching frequency $f = 6.6$
Hz are equal for all cases. Due to higher chord length the Reynolds number is $Re_{2D} = 3.0 \cdot 10^6$
and the reduced frequency is $k_{2D} = 0.07$ for the 2D-cases.

The strongest discrepancy between the 2D-case and the blade tip is detected at the kink. The
suction at the leading edge is decreased for the blade tip over the whole cycle. Again, this indi-
cates that the spanwise velocities which have opposite signs at the forward and backward swept
part lead to a less accelerated flow at the leading edge. At the trailing edge the flow is less
decelerated. Consequently the suction peak is lower and stall is postponed to higher angles of
attack for the blade tip. It is remarkable, that the phase-averaged c_p-data of the 2D-case shows
strong oscillations after the first drop in the c_p-distribution. Nevertheless, the standard deviation
remains high, so that no stronger similarity from cycle to cycle can be deduced.
At section S6, the suction peak is higher, sharper and located closer to the leading edge then for
the 2D case. The deflection of the inflow due to the sweep seems to lead to a stronger accelerated
flow at the leading edge and consequently to the increased suction peak. Flow separation occurs
around the same phase angles but is more pronounced for the 3D-case. Similar to the differ-
ences at section S2 at high angles of attack, this can be caused by the lower Reynolds number
and the lower reduced frequency, as shown in the preceding sections. One can state, that the
agreement between the 2D- and 3D-c_p-distributions at the section S2 is well for the first half of
the cycle. The differences in the c_p-distributions are smaller at the trailing edge. The suction
level is similar, even as flow separates around $\psi \approx 225°$. At $x/c = 0.86$, a c_p-distribution of a
pressure transducer located further inboard at section S1 is depicted. From the lower suction
level around $\psi \approx 270°$, one can deduce that the twist reduction towards the root is sufficient to
avoid separation to be triggered by the corner stall at the wind tunnel wall. As shown in Gardner
et al. [77], the gap between wind tunnel model and wind tunnel wall also reduces the tendency
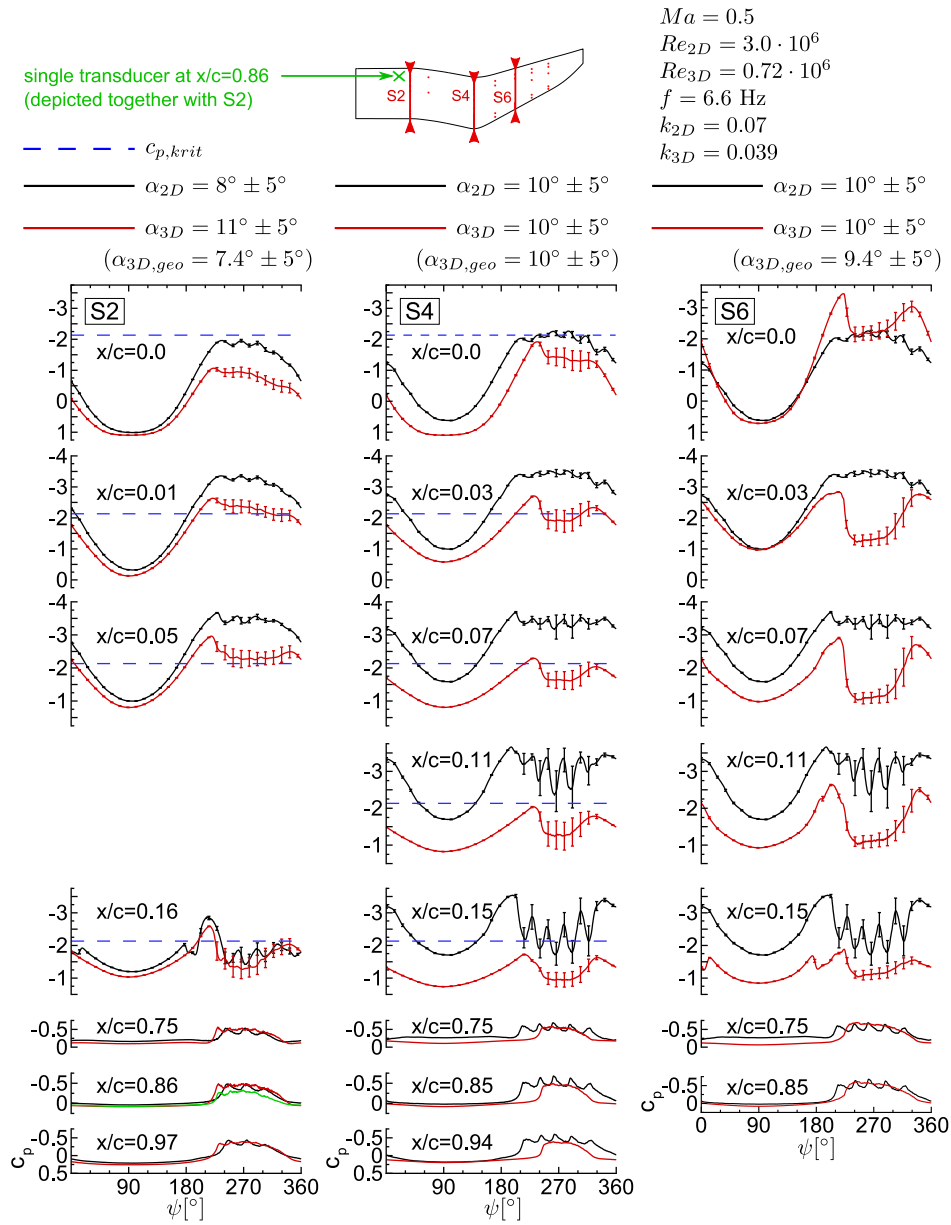towards flow separation.

Figure 5.26: **Comparison of the blade tip to 2D airfoil experiments**

5.7 Influence of the Surface Roughness - Pressure Sensitive Paint

In the second measurement campaign the pressure distribution on the upper surface of the model was investigated by means of unsteady pressure sensitive paint (iPSP). As shown by the static polars in Fig. 4.2, the surface roughness and the thickening of the airfoil seems to change the flow significantly. Before investigating the influence of the oscillation amplitude by means of iPSP, the pressure distributions of LC-DS2 with and without coating are shown. In Figs. 5.27 and 5.28, the phase-averaged data is shown for the sections S2 and S4-S8. The iPSP-measurements have a sampling frequency of 64 points per period.
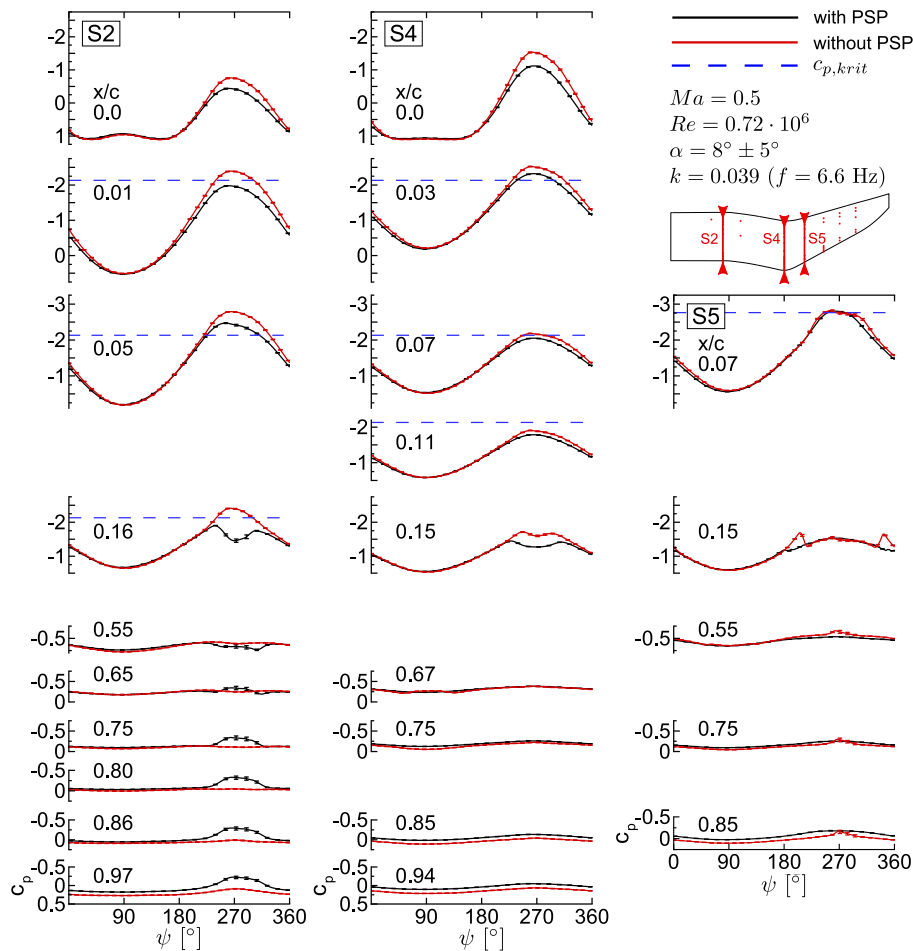
Figure 5.27: $Ma = 0.5$, $\alpha = 8° \pm 5°$ **with and without iPSP**

One can deduce, that the coating enhances trailing edge separation at the inboard section S2 where the airfoil thickness is 12% (EDI-M112). The suction level at the trailing edge is significantly increased around the maximum angle of attack. However, the suction peak at the leading edge does not collapse, but is slightly decreased. According to Schlichting [58], the increased surface roughness shifts the laminar-turbulent transition in upstream direction. This can be seen in the c_p-distribution of section S4 at $x/c = 0.15$. In case of the coated surface the transition
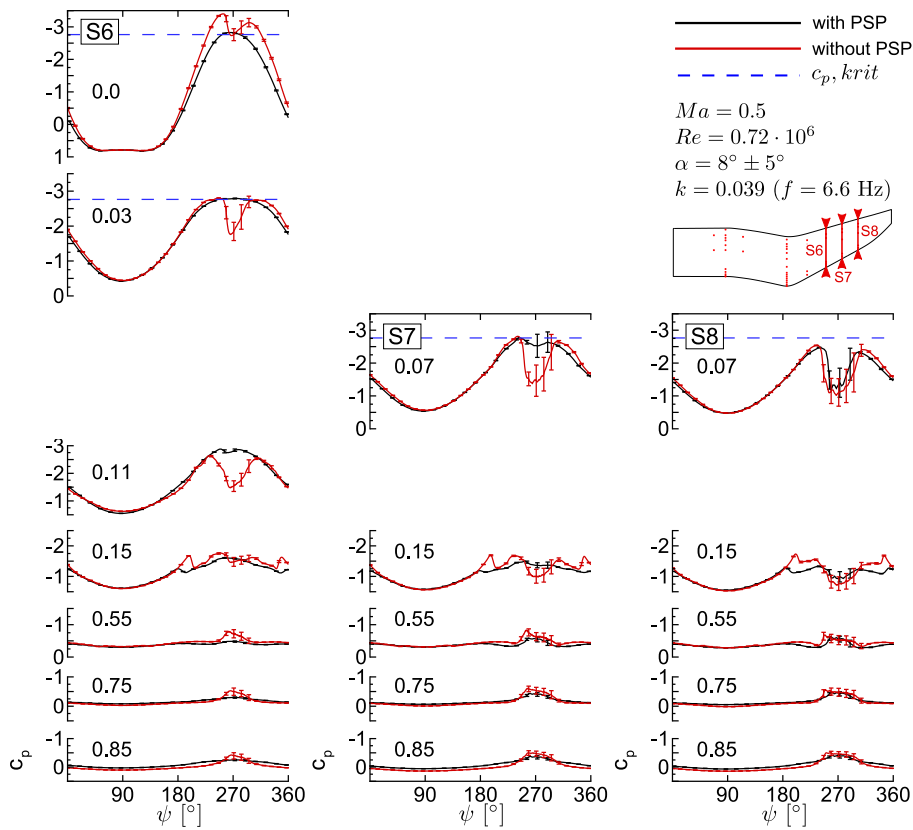
Figure 5.28: $Ma = 0.5$, $\alpha = 8° \pm 5°$ **with and without iPSP**

drop can be seen at a lower angle of attack at the upstroke and the downstroke. Thus, the region of the turbulent boundary layer is increased and consequently the thickness of the boundary layer is also increased. This leads to an decreased local angle of attack. Both effects, the larger turbulent boundary layer and the reduction of the local angle of attack lead to a stabilized flow at all sections. At the outboard sections, the drop in the suction peak around the maximum angle of attack is significantly lower than for the uncoated model. Only at S8, where the maximum flow separation occurs, the elevated suction at the trailing edge and the drop at $x/c = 0.07$ are nearly equal.

5.8 Influence of the Oscillation Amplitude

Varying the oscillation amplitude from $\alpha = 8 \pm 4$ (LC-DS7) to $\alpha = 8 \pm 6$ (LC-DS8) changes the flow significantly. The two test cases are compared for the coated model. The upper surface pressure coefficient measured by means of unsteady pressure sensitive paint is shown for selected phase angles ψ in Fig. 5.29. Due to the low time resolution of the PSP-recordings, the test cases do not have data points at exactly the same phase angles. However, the variation is less than $\Delta\psi = \pm 2°$. The last pixels at the leading edge are also not resolved properly because of its strong curvature and the view direction of the cameras. The greyed out areas could not be observed with the cameras.
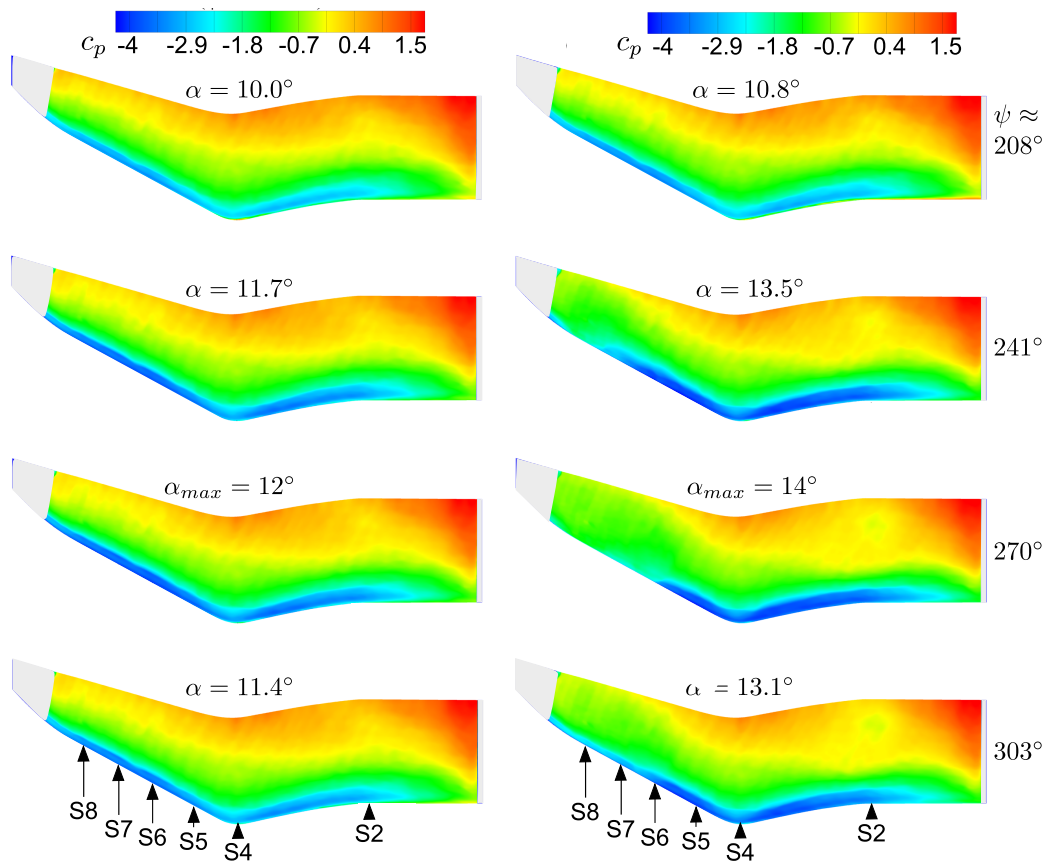
Figure 5.29: $Ma = 0.5$, $\alpha = 8° \pm 4°$ (**LC-DS7**) vs $\alpha = 8° \pm 6°$ (**LC-DS8**)

The flow is attached over the whole cycle for LC-DS7. No separated flow can be detected in the pressure transducer signals nor in the surface pressure measured by iPSP. Till $\psi \approx 208°$, LC-DS8 shows attached flow over the whole surface. At section S2, LC-DS8 shows an elevated suction plateau which starts at the trailing edge at $\psi \approx 240°$ and quickly moves forward to $x/c = 0.64$. The plateau remains till $\psi \approx 300°$ but does not lead to a collapse of the leading edge suction peak. This can be also detected in the surface pressure distributions at $\alpha = 13.5°$, $\alpha_{max} = 14.2°$ and $\alpha = 13.1°$ in Fig. 5.29. The flow is attached for both test cases at section S4. Outboard of the kink flow separation occurs first at section S8 but quickly spreads to section S7 and S6, as

one can see at $\alpha = 13.5°$ and $\alpha_{max} = 14.2°$ in Fig. 5.29. The separation is more abrupt and starts from the leading edge. The suction peaks drop. At S6, the drop at $x/c = 0.0$ is not as significant as at $x/c = 0.3$ and $x/c = 0.11$. This might be due to the fast reattachment of the flow at the leading edge or due to disturbance by the stronger separated flow further outboard. At $\alpha = 13.1°$, the flow has reattached at the backward swept part whereas the trailing edge separation is still evident at the beginning of the forward sweep. Short behind $\psi \approx 303°$ the flow is reattached over the whole blade tip.
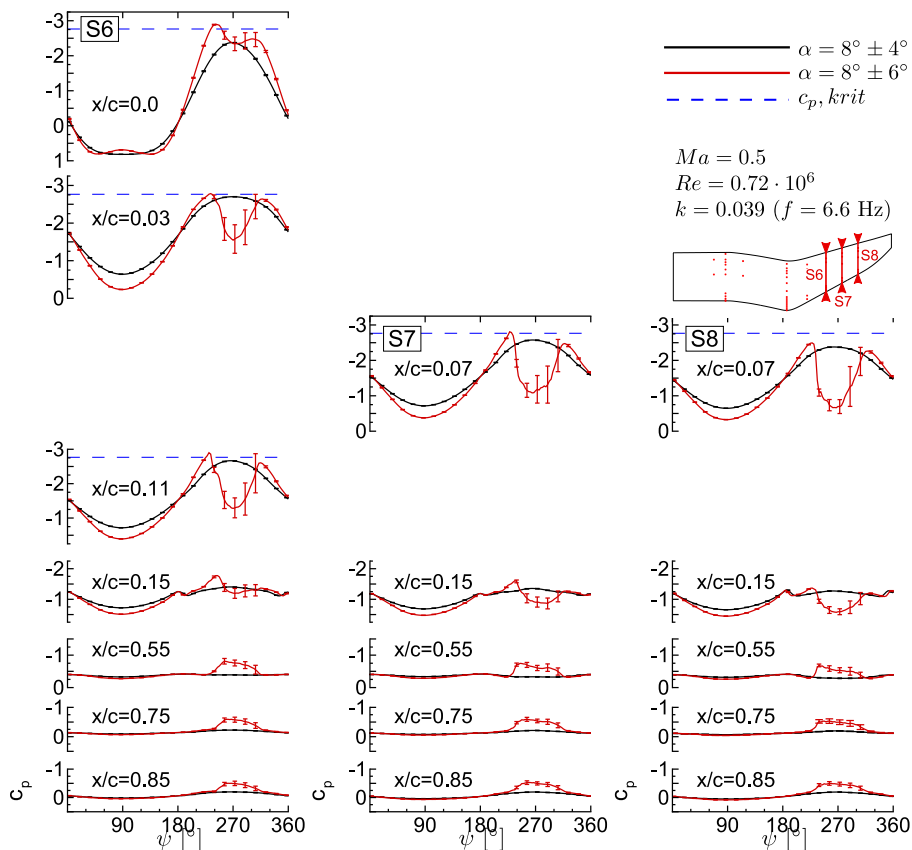
Figure 5.30: $Ma = 0.5$, $\alpha = 8° \pm 4°$ **vs** $\alpha = 8° \pm 6°$

5.9 Influence of the Mach number

LC-DS8 is compared to the test case LC-DS9 where the Mach number is decreased from $Ma = 0.5$ to $Ma = 0.4$. The Reynolds number is $0.72 \cdot 10^6$ at $Ma = 0.5$ and $0.96 \cdot 10^6$ at $Ma = 0.4$. The angle of attack and the pitching frequency are not changed: $\alpha = 8° \pm 6°$ and $f = 6.6$ Hz. The reduced frequency increases from $k = 0.039$ to $k = 0.049$. Two instantaneous c_p-surface distributions are shown for $Ma = 0.4$ in Fig. 5.31. In comparison to Fig. 5.29 in the preceding section the following is observed: at the maximum angle of attack, a separated flow region occurs at section S2, similar to the higher Mach number. However, the flow seems still attached

at the outboard backward swept part and the suction peak at the leading edge has not collapsed as it does for the higher Mach number.
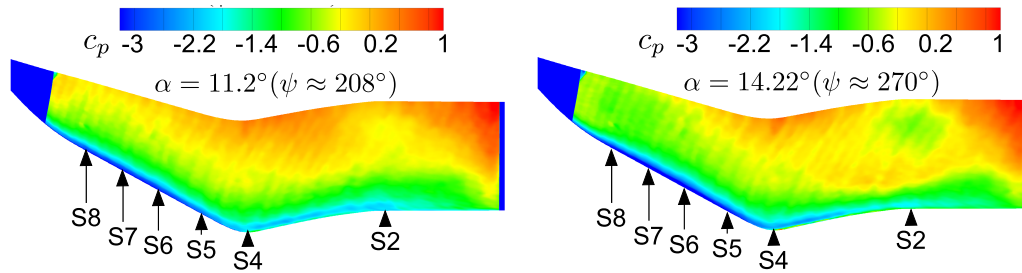
Figure 5.31: **Two instantaneous PSP measurements for** $Ma = 0.4$ **and** $\alpha = 8° \pm 6°$
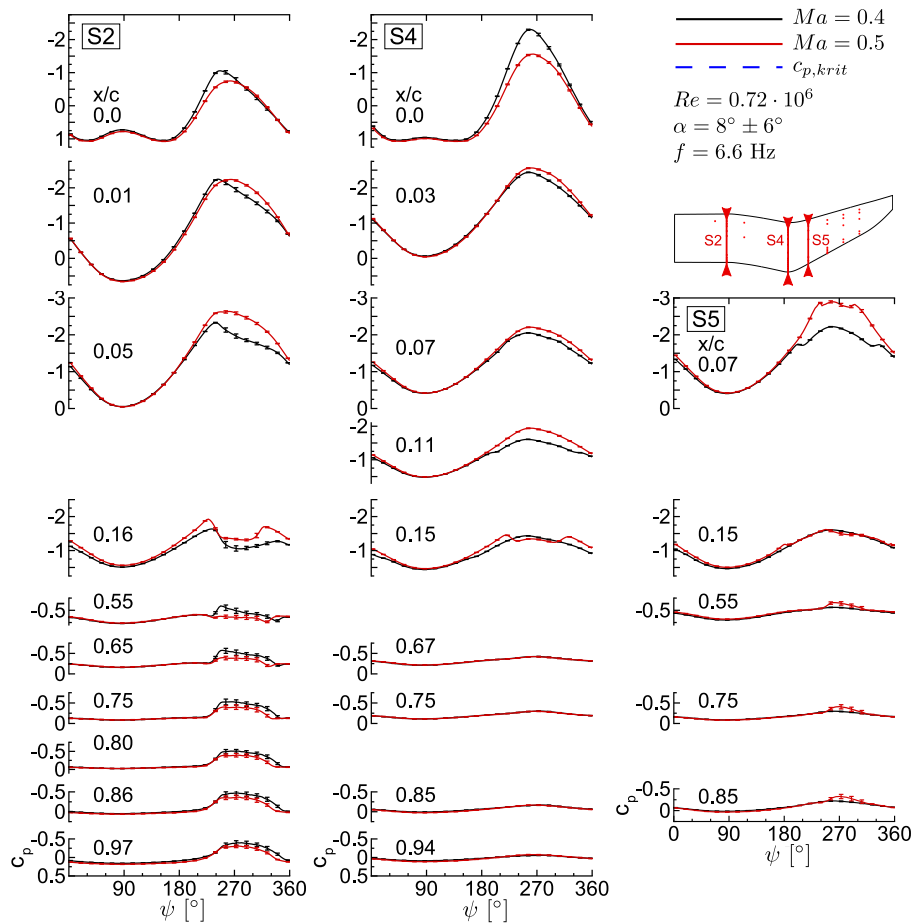
Figure 5.32: $Ma = 0.5$ **vs** $Ma = 0.4$**,** $\alpha = 8° \pm 6°$**, pressure transducers**

In Figs. 5.32 and 5.33 the discrete pressure measurements reflect the behavior mentioned above. The critical pressure c_p is not indicated for the different Mach numbers. The critical pressure at $Ma = 0.4$ is $c_{p,krit} = -3.6$ at section S2 and $c_{p,krit} = -5.0$ at the backward swept part. This value seems not to be reached at any spanwise position, so that neither supersonic flow nor shocks occur at $Ma = 0.4$. Laminar-turbulent transition is shifted in upstream direction for the lower Mach Number as one can see $x/c = 0.11 - x/c = 0.15$ at section S4. This phenomenon

could also be caused by the slightly higher Reynolds number at $Ma = 0.4$. Nevertheless, the difference between the Reynolds numbers is small and reduced Mach number certainly favors the stabilized flow at the leading edge at the outboard section. One the other hand, the longer turbulent boundary layer at $Ma = 0.4$ leads to an increased trailing edge separation at section S2. This leads to a smooth collapse of the suction peak at the leading edge, before the maximum angle of attack is reached. The $c_p - \alpha$-distribution would show a strong hysteresis.

Figure 5.33: $Ma = 0.5$ **vs** $Ma = 0.4$**,** $\alpha = 8° \pm 6°$**, pressure transducers**

6 Conclusion

The dynamic stall behavior of an advanced double-swept helicopter rotor blade tip has been investigated in the Transonic Wind Tunnel Göttingen. In fast forward or maneuvering flight of a helic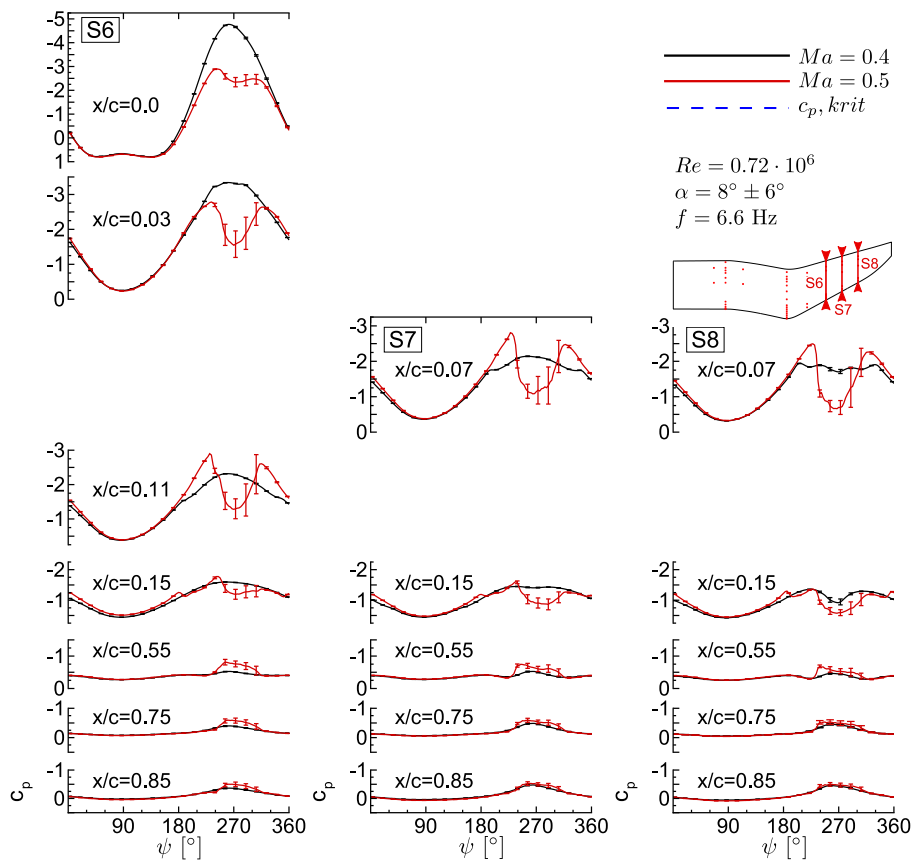opter the angle of attack varies sinusoidally once per revolution in order to balance the lift. This variation of the angle of attack is reproduced with a hydraulic oscillation rig which drives the wind tunnel model. Due to the complex planform, the high degree of instrumentation, the high loads and the high aspect ratio $AR = 4.5$ of the model, the structural design is very demanding. Its most important aspects are summarized in the first part of the conclusion. The second part deals with the dynamic stall behavior and the most important flow phenomena occurring on this model. The influence of the different flow parameters and the surface roughness on the flow separation are shortly recapitulated.

Structural Design of the Wind Tunnel Model

A carbon fiber reinforced plastic CFRP rotor blade tip built for the DNW-TWG. The ribless design with one central spar is well suited for highly loaded models with a high degree of instrumentation. Sixty unsteady pressure transducers, two accelerometers and two temperature sensors are integrated in the model of 750 mm span. A steel shaft which is bonded to the half shells and the spar, transfers the loads to the piezoelectric balance which is mounted on the hydraulic test oscillation rig. This concept assures a high stiffness with the first eigenfrequency at $f = 67$ Hz and a low mass ($m = 4.6$ kg).

For the first time, a mold with removable inserts has been used to check the leak-tightness of the pressure transducers during the manufacturing process. Furthermore, the half shells can be retained in the mold by partial vacuum in case of an unwanted detachment. Nevertheless, the surface quality is well.

The experimental modal analysis on a solid steel block shows excellent agreements to the numerical results. However, the experimental and numerical results with the wind tunnel clamp condition show discrepancies due to the simplified boundary condition in the FE model. The strength analysis is not affected by this simplification.

Flow separation and Dynamic Stall on the Double-Swept Blade Tip

Dynamic stall has been investigated by means of global balance data and local pressure data. The optically recorded aeroelastic deformation is low due to the stiff design of the model. Thus, computational fluid dynamic simulations with a rigid contour show a good agreement to the experimental data and confirm the limited influence of the elasticity on the aerodynamics of the wind tunnel model.

Light Dynamic Stall

For the reference case LC-DS1 ($Ma = 0.5$, $Re = 1.2 \cdot 10^6$, $\alpha = 8° \pm 5°$, $k = 0.039$), the computed global and sectional moments show a well-balanced model. The pitching moment decreases smoothly at the upstroke. Before the maximum angle of attack, the positive pitching moment of the forward swept part leads even to an increase of the global pitching moment. Then, a sharp drop and strong oscillations result from the flow separation at the backward swept part the pitching moment. First flow separation is detected at the most outboard section S8 ($y/R = 0.83$) even though the geometric twist is decreased from the forward-backward kink to the tip. The spanwise velocity components caused by the sweep and the tip vortex encourage the separation of the flow at this position. The locally reduced Reynolds number caused by the taper might be another trigger of the separation since it increases the length of the less stable laminar flow. The thin airfoil EDI-M109 with 9% thickness leads to a sharp and sudden stall where the suction peaks collapse. Clearly discernible oscillations in the c_p-distributions indicate several vortices travelling across the blade. The broad spectral content of the pressure signals do not indicate any elevated frequency besides the pitching frequency. The eigenfrequencies of the model do not seem to affect the flow, the first higher harmonics are slightly dominant. According to the computations there is a fast alteration of massive detached flow with clearly discernible vortical structures and almost attached flow around the maximum angle of attack.

At the forward swept part, the spanwise velocity components point in the opposite direction than at the backward swept part. Thus, the flow at the leading edge of the kink, is decelerated, the suction peak decreased. At the trailing edge, the flow is accelerated and stabilized. For all presented test cases, the flow separates at the kink at last. One significant advantage of the forward-backward swept planform is that the sectional lift and moment do not collapse simultaneously over the span width. Thus, a sharp gradient in the global pitching moment is avoided.

The forward sweep, the airfoil EDI-M112 with 12%-thickness and the reduced twist towards the root, lead to a very stable flow at the inboard section. Only slight trailing edge separation is detected at the beginning of the forward sweep for the reference case.

Increasing the mean angle of attack or increasing the oscillation amplitude lead to very similar results: the flow is separated over a larger part of the cycle than at the reference case. At the outboard section, less clear oscillations are found when the flow separates. A second region of flow separation is detected at the beginning of the forward sweep. The airfoil EDI-M112 with 12% thickness leads to a softer stall behavior than at the backward swept part. The suction peak is only reduced but does not collapse completely. The detached flow remains close to the trailing edge.

Deep Dynamic Stall

Only the test case with $\alpha_{max} \approx 15°$ shows separated flow at the kink. This test case is compared to two-dimensional airfoil experiments. However, conclusions are not unambiguous since the Reynolds number is about four times lower for the blade tip experiment. A preliminary comparison of two test cases with the blade tip at different Reynolds numbers ($Re = 0.72 \cdot 10^6$ and $Re = 1.2 \cdot 10^6$) showed significantly stronger flow separation for the lower Reynolds number. Hence, it is not astonishing that the blade tip shows stronger flow separation than the 2D experiments due to the lower Reynolds number. However, the comparisons between the 2D-experiments and the double-swept blade tip confirm the strong difference at the kink due to the spanwise velocities, as mentioned above. There is a strong and nearly constant Δc_p over the whole cycle at the kink. The stall is delayed but the lift is decreased. On the contrary, the unswept part shows a good agreement to the 2D-data as long as the flow is attached. As soon as flow separation sets in, stronger oscillations are found in the pressure signals of the two-dimensional test cases.

Increasing the surface roughness by the pressure sensitive paint changes the flow significantly. Laminar-turbulent transitions is moved upstream. Thus, the flow is stabilized and flow separation delayed at the backward swept part. At the inboard section, where the thicker airfoil is located, the trailing edge separation is increased. The unsteady pressure sensitive paint measurements show the areas of separated flow very well: the leading edge separation at the backward swept part and the trailing edge separation at the unswept inboard section. Decreasing the Mach number from $Ma = 0.5$ to $Ma = 0.4$ stabilizes the flow at high angles of attack at the backward swept part since no shocks establish anymore.

Future Work

The design could be further improved by using a CFRP shaft at the root. Thus, the mass and the moment of inertia would be further reduced while keeping a high stiffness. A more perfect α-signal is desirable in order to reduce higher harmonics in the α-signal. Dynamic tests at higher Mach numbers could give deeper insights into the aerodynamics at the advancing blade. Computations for different load cases should be carried out in order to further validate the computational setup. Comparing the results to a rotating system with the same advanced rotor blade tips would give insights how fundamental the investigated effects are. Do the centrifugal forces and the non-uniform inflow change the observed phenomena completely. How does the flow separation change in the rotating system? Which are the most sensitive parameters with regard to dynamic stall of the rotating system.

Bibliography

[1] Perry, F., "Aerodynamics of the Helicopter World Speed Record." *Proceedings of the 43rd Annual Forum of the American Helicopter Society*, 1987, pp. 3–15.

[2] Leishman, G. J., *Principles of Helicopter Aerodynamics with CD extra.*, Cambridge university press, 2006.

[3] Johnson, W., *Helicopter theory*, Courier Corporation, 2012.

[4] Gustafson, F. and Myers Jr, G., "Stalling of Helicopter Blades." 1946.

[5] Harris, F. D. and Pruyn, R. R., "Blade Stall - Half Fact, Half Fiction." *Journal of the American Helicopter Society*, Vol. 13, No. 2, 1968, pp. 27–48.

[6] Pruyn, R. R., "In-Flight Measurement of Rotor Blade Airloads, Bending Moments, and Motions, Together with Rotor Shaft Load and Fuselage Vibration, on a Tandem Rotor Helicopter. VOLUME 4. SUMMARY AND EVALUATION OF RESULTS," Tech. rep., DTIC Document, 1967.

[7] Bousman, W. G., "A Qualitative Examination of Dynamic Stall from Flight Test Data." *Journal of the American Helicopter Society*, Vol. 43, No. 4, 1998, pp. 279–295.

[8] Kufeld, R., Balough, D. L., Cross, J. L., and Studebaker, K. F., "Flight Testing the UH-60A Airloads Aircraft." *Annual Forum Proceedings-American Helicopter Society*, Vol. 5, American Helicopter Society, 1994, pp. 557–557.

[9] Kufeld, R. M. and Bousman, W. G., "High Load Conditions Measured on a UH-60A in Maneuvering Flight." *Journal of the American Helicopter Society*, Vol. 43, No. 3, 1998, pp. 202–211.

[10] Ham, N. D., "Aerodynamic Loading on a Two-Dimensional Airfoil During Dynamic Stall." *AIAA journal*, Vol. 6, No. 10, 1968, pp. 1927–1934.

[11] Ham, N. D. and Garelick, M. S., "Dynamic Stall Considerations in Helicopter Rotors." *Journal of the American Helicopter Society*, Vol. 13, No. 2, 1968, pp. 49–55.

[12] McCroskey, W. and Fisher, R., "Dynamic Stall of Airfoils and Helicopter Rotors." *AGARD Paper*, , No. R595, 1972.

[13] Carr, L. W., McAlister, K. W., and McCroskey, W. J., "Analysis of the Development of Dynamic Stall Based on Oscillating Airfoil Experiments." *Technical Report NASA-TN-D-8382*, 1977.

[14] Carr, L. W., "Progress in Analysis and Prediction of Dynamic Stall." *Journal of aircraft*, Vol. 25, No. 1, 1988, pp. 6–17.

[15] Liiva, J., "Unsteady Aerodynamic and Stall Effects on Helicopter Rotor Blade Airfoil Sections." *Journal of Aircraft*, Vol. 6, No. 1, 1969, pp. 46–51.

[16] McCroskey, W., "The phenomenon of Dynamic Stall." Tech. rep., DTIC Document, 1981.

[17] McCroskey, W., McAlister, K., Carr, L., Pucci, S., Lambert, O., and Indergrand, R., "Dynamic Stall on Advanced Airfoil Sections." *Journal of the American Helicopter Society*, Vol. 26, No. 3, 1981, pp. 40–50.

[18] Geissler, W., Dietz, G., Mai, H., Junker, B., and Lorkowski, T., "Dynamic Stall Control Investigations on a Full Size Chord Blade Section." *30th ERF, Marseille, France*, 2004.

[19] Gardner, A., Richter, K., Mai, H., and Neuhaus, D., "Experimental Investigation of Air Jets for the Control of Compressible Dynamic Stall." *Journal of the American Helicopter Society*, Vol. 58, No. 4, 2013, pp. 1–14.

[20] Mai, H., Dietz, G., Geißler, W., Richter, K., Bosbach, J., Richard, H., and de Groot, K., "Dynamic stall control by leading edge vortex generators." *Journal of the American Helicopter Society*, Vol. 53, No. 1, 2008, pp. 26–36.

[21] Gardner, A., Richter, K., Mai, H., and Neuhaus, D., "Experimental Control of Compressible OA209 Dynamic Stall by Air Jets." *Proceedings of the 38th European Rotorcraft Forum*, 2012.

[22] Richter, K., Koch, S., Goerttler, A., Lütke, B., Wolf, C. C., and Benkel, A., "Unsteady Boundary Layer Transition on the DSA-9A Rotor Blade Airfoil." *Proceedings of the 41st European Rotorcraft Forum*, 2015.

[23] Klein, A., Richter, K., Altmikus, A., Lutz, T., and Krämer, E., "Unsteady Criteria for Rotor Blade Airfoil Design." *35th European rotorcraft forum*, Vol. 1, 2009, pp. 358–367.

[24] Gardner, A., Richter, K., Mai, H., Altmikus, A., Klein, A., and Rohardt, C.-H., "Experimental Investigation of Dynamic Stall Performance for the EDI-M109 and EDI-M112 airfoils." *Journal of the American Helicopter Society*, Vol. 58, No. 1, 2013, pp. 1–13.

[25] St Hilaire, A., Carta, F., Fink, M., and Jepson, W., "Influence of Sweep on the Aerodynamic Loading of an Oscillating NACA 0012 Airfoils – Volume 1. TECHNICAL REPORT," Tech. rep., 1979.

[26] Triebstein, H., "Unsteady Pressure Measurements on Rotor Blade Tips with Incidence." *AIAA Journal*, Vol. 17, No. 5, 1979, pp. 514–518.

[27] Lorber, P. F. and Covino Jr, A. F., "Dynamic Stall Experiments on a Swept Three-Dimensional Wing in Compressible Flow," *AIAA, Fluid Dynamics, Plasma Dynamics and Lasers Conference, 22 nd, Honolulu, HI*, 1991, p. 1991.

[28] Lorber, P. F. and Carta, F. O., "Airfoil Dynamic Stall at Constant Pitch Rate and High Reynolds Number." *Journal of Aircraft*, Vol. 25, No. 6, 1988, pp. 548–556.

[29] Lorber, P. F., "Dynamic Stall of Sinusoidally Oscillating Three-Dimensional Swept and Unswept Wings in Compressible Flow." *AHS, Annual Forum, 48 th, Washington, Proceedings.*, Vol. 2, 1992, pp. 1307–1322.

[30] Lorber, P. F., "Compressibility Effects on the Dynamic Stall of a Three-Dimensional Wing." *AIAA, Aerospace Sciences Meeting and Exhibit, 30 th, Reno, NV*, 1992.

[31] Lorber, P. F., "Tip Vortex, Stall Vortex, and Separation Observations on Pitching Three-Dimensional Wings." *AIAA, Fluid Dynamics Conference, 24 th, Orlando, FL*, 1993, p. 1993.

[32] Tang, D. and Dowell, E., "Experimental Investigation of Three-Dimensional Dynamic Stall Model Oscillating in Pitch." *Journal of aircraft*, Vol. 32, No. 5, 1995, pp. 1062–1071.

[33] Johnson, W., "Technology Drivers in the Development of CAMRAD II." *American helicopter society aeromechanics specialists conference, San Francisco, California*, 1994.

[34] Coton, F. N. and Galbraith, R. A., "An Examination of Dynamic Stall on an Oscillating Rectangular Wing." *21st applied aerodynamics conference, Orlando, Florida. Paper AIAA-2003-3675*, 2003.

[35] Coton, F. and Galbraith, R., "An Experimental Study of Dynamic Stall on a Finite Wing." *Aeronautical Journal*, Vol. 103, No. 1023, 1999, pp. 229–236.

[36] Le Pape, A., Pailhas, G., David, F., and Deluc, J., "Extensive Wind Tunnel Measurements of Dynamic Stall Phenomenon for the OA209 Airfoil Including 3D effects." *33rd European Rotorcraft forum, Kazan, Russia*, 2007.

[37] Merz, C. B., Wolf, C. C., Richter, K., Kaufmann, K., and Raffel, M., "Experimental Investigation of Dynamic Stall on a Pitching Rotor Blade Tip." *STAB Symposium München*, 2014.

[38] Merz, C., Wolf, C., Richter, K., Kaufmann, K., Mielke, A., and Raffel, M., "Spanwise Differences in Static and Dynamic Stall on a Pitching Rotor Blade Tip Model." *Proceedings of the 41st European Rotorcraft Forum*, 2015.

[39] Brocklehurst, A. and Duque, E., "Experimental and numerical study of the British Experi-

mental Rotor Programme blade," *Flight Simulation Technologies Conference and Exhibit*, 1990, p. 3008.

[40] Scott, M., Sigl, D., and Strawn, R., "Computational and Experimental Evaluation of Helicopter Rotor Tips for High Speed Forward Flight." *AIAA paper*, Vol. 89, 1989, pp. 12–16.

[41] Yeager, W. T., Jr., Noonan, K. W., Singleton, J. D., Wilbur, M. L., and Mirick, P. H., "Performance and Vibratory Loads Data From a Wind-Tunnel Test of a Model Helicopter MainRotor Blade With a Paddle-Type Tip." Tech. rep., 1997.

[42] Rauch, P., Gervais, M., Cranga, P., Baud, A., Hirsch, J.-F., Walter, A., and Beaumier, P., "Blue Edge: The Design, Development and Testing of a New Blade Concept." *AHS 67th International Forum*, AHS, May 2011.

[43] Splettstößer, W. R., Schultz, K.-J., Buchholz, H., van der Wall, B. G., Junker, B., Wagner, W., Mercker, E., and Pengel, K., "ERATO Rotor - Validation Test in the DNW - Documentation and Representative Results," *DLR-Interner Bericht*, Vol. 129-99/30, 1999.

[44] Prieur, J. and Splettstoesser, W., "ERATO-An ONERA-DLR Cooperative Programme On Aeroacoustic Rotor Optimization." *Proceedings of the 35th European Rotorcraft Forum*, 1999.

[45] van der Wall, B. G., Keßler, C., Delrieux, Y., Beaumier, P., Gervais, M., Hirsch, J.-F., Pengel, K., and Crozier, P., "From ERATO Basic Research to the Blue Edge Rotor Blade." *Rotorcraft Virtual Engineering Conferencee, Liverpool*, 2016.

[46] Brocklehurst, A. and Barakos, G., "A review of helicopter rotor blade tip shapes." *Progress in Aerospace Sciences*, Vol. 56, 2013, pp. 35–74.

[47] Wedemeyer, E., Taylor, N., and Holst, H., "Adaptive Wall Techniques." *AGARD AG*, Vol. 336, 1998.

[48] Wiggen, S. and Voß, G., "Development of a Wind Tunnel Experiment for Vortex Dominated Flow at a Pitching Lambda Wing." *CEAS Aeronautical Journal*, Vol. 5, No. 4, 2014, pp. 477–486.

[49] Lütke, B., Schmidt, M., Sinske, J., and Neumann, J., "Structural Design of an Instrumented Double-Swept Wind Tunnel Model," *20th International Conference on Composite Materials*, 2015.

[50] Mai, H., *Untersuchung der Druckverteilungen eines Schwingenden Ringflügels in Transsonischer Strömung.*, Ph.D. thesis, 2012.

[51] Pengel, K., Müller, R., and Van der Wall, B., "Stereo Pattern Recognition–the Technique for Reliable Rotor Blade Deformation and Twist Measurement." *Proceedings of the American Helicopter Society International Meeting on Advanced Rotorcraft Technology and Life Saving Activities (Heli Japan), Tochigi, Utsunomiya, Japan*, 2002.

[52] Carius, M., "Entwicklung einer Software zur Auswertung von Verformungen in Aeroelastischen Windkanalversuchen." *DLR IB 232-2010 J 05*, 2010.

[53] Carius, M., "Kalibrierung und Bestimmung der Genauigkeit des picCOLOR Positionsmesssystems." *DLR IB 232-2010 J 03*, 2010.

[54] Schewe, G., "A Multicomponent Balance Consisting of Piezoelectric Force Transducers for a High-Pressure Wind Tunnel." *Sensors and systems'82*, 1982, pp. 13–23.

[55] Schewe, G., "On the Force Fluctuations Acting on a Circular Cylinder in Crossflow from Subcritical up to Transcritical Reynolds Numbers." *Journal of fluid mechanics*, Vol. 133, 1983, pp. 265–285.

[56] Schewe, G., "Force Measurements in Aerodynamics Using Piezoelectric Multicomponent Force Transducers." *ICIASF'85-11th International Congress on Instrumentation in Aerospace Simulation Facilities*, Vol. 1, 1985, pp. 263–268.

[57] Schewe, G., "Force and Moment Measurements in Aerodynamics and Aeroelsticity using Piezoelectric Transducers." *Springer Handbook of Experimental Fluid Mechanics*, Vol. 96, 2007, pp. 596–616.

[58] Schlichting, H. and Gersten, K., *Grenzschichttheorie.*, Springer-Verlag, 2006.

[59] Nitsche, W. and Brunn, A., *Strömungsmesstechnik.*, Springer-Verlag, 2006.

[60] Liu, T., *Pressure-and Temperature-Sensitive Paints*, Wiley Online Library, 2004.

[61] Schwamborn, D., Gerhold, T., and Hannemann, V., "On the Validation of the DLR-TAU Code," *New Results in Numerical and Experimental Fluid Mechanics II*, Springer, 1999, pp. 426–433.

[62] Gerhold, T., Galle, M., Friedrich, O., Evans, J., Gerhold, T., Galle, M., Friedrich, O., and Evans, J., "Calculation of complex three-dimensional configurations employing the DLR-TAU-code," *35th Aerospace Sciences Meeting and Exhibit*, 1997, p. 167.

[63] Menter, F. R., "Zonal two equation k-turbulence models for aerodynamic flows," *AIAA paper*, Vol. 2906, 1993, pp. 1993.

[64] Lütke, B., Neumann, J., and Schmidt, M., "Design of a Rotor Blade Tip for the Investigation of Dynamic Stall in the Transonic Wind Tunnel Göttingen," *40th European Rotorcraft Forum 2014*, 2014.

[65] Zienkiewicz, O. C., Taylor, R. L., Zienkiewicz, O. C., and Taylor, R. L., *The finite element method*, Vol. 3, McGraw-hill London, 1977.

[66] Kohnke, P., "Theory reference for the mechanical APDL and mechanical applications," *Ansys Inc, release*, Vol. 12, 2009.

[67] Golub, G. H. and Underwood, R., "The block Lanczos method for computing eigenvalues," *Mathematical software*, Vol. 3, 1977, pp. 361–377.

[68] Schimke, D., Link, S., and Schneider, S., "Noise and Performance Improved Rotor Blade for a Helicopter." *Patent EP 2 505 500 A1*, 03 2011.

[69] Lütke, B., Nuhn, J., Govers, Y., and Schmidt, M., "Design of a rotor blade tip for the investigation of dynamic stall in the transonic wind-tunnel Göttingen," *The Aeronautical Journal*, Vol. 120, No. 1232, 10 2016, pp. 1509–1533.

[70] Bailie, J., Ley, R., and Pasricha, A., "A summary and review of composite laminate design guidelines," *Langley RC, Hampton*, 1997.

[71] Allemang, R. J., "The modal assurance criterion–twenty years of use and abuse," *Sound and vibration*, Vol. 37, No. 8, 2003, pp. 14–23.

[72] Puck, A. and Schürmann, H., "Failure analysis of FRP laminates by means of physically based phenomenological models," *Composites Science and Technology*, Vol. 58, No. 7, 1998, pp. 1045–1067.

[73] Gardner, A., Richter, K., and Rosemann, H., "Prediction of the Wind Tunnel Sidewall Effect for the iGREEN Wing-Tailplane Interference Experiment." *New Results in Numerical and Experimental Fluid Mechanics VII*, edited by A. Dillmann, G. Heller, M. Klaas, H.-P. Kreplin, W. Nitsche, and W. Schröder, Vol. 112 of *Notes on Numerical Fluid Mechanics and Multidisciplinary Design*, Springer Berlin Heidelberg, 2010, pp. 75–82.

[74] Gerhold, T. and Neumann, J., "The parallel mesh deformation of the DLR TAU-code," *New results in numerical and experimental fluid mechanics VI*, Springer, 2007, pp. 162–169.

[75] Neumann, J. and Krüger, W., "Coupling Strategies for Large Industrial Models." *Computational Flight Testing*, edited by N. Kroll, R. Radespiel, J. van der Burg, and K. Sorensen, Vol. 123 of *Notes on Numerical Fluid Mechanics and Multidisciplinary Design*, Springer, 2013, pp. 207–222.

[76] O'Meara, M. and Mueller, T., "Experimental determination of laminar separation bubbles on the airfoil at low Reynolds numbers," *AIAA Journal*, Vol. 25, 1987, pp. 00–00.

[77] Gardner, A. D. and Richter, K., "Effect of the model-sidewall connection for a static airfoil experiment," *Journal of Aircraft*, Vol. 50, No. 2, 2013, pp. 677–680.